DEVELOPMENT OF DISCONTINUITIES

IN GRANULAR MEDIA

A thesis
Presented to
The Academic Faculty

by

Hosung Shin

In Partial Fulfillment
of the Requirements for the Degree
Doctor of Philosophy in the
School of Civil and Environmental Engineering

Georgia Institute of Technology
August 2009

DEVELOPMENT OF DISCONTINUITIES

IN GRANULAR MEDIA

Approved by:

Dr. J. Carlos Santamarina, Advisor
School of Civil and Environmental Engineering
Georgia Institute of Technology

Dr. Robert C. Bachus
School of Civil and Environmental Engineering
Georgia Institute of Technology

Dr. Paul W. Mayne
School of Civil and Environmental Engineering
Georgia Institute of Technology

Dr. Guillermo Goldsztein
School of Mathematics
Georgia Institute of Technology

Dr. Susan E. Burns
School of Civil and Environmental Engineering
Georgia Institute of Technology

Dr. Joseph A. Cartwright
School of Earth, Ocean and Planetary Sciences
Cardiff University, UK

Date Approved: May 27, 2009

ACKNOWLEDGEMENTS

I would like to thank my advisor, Dr. J. Carlos Santamarina for such a wonderful time with him. Looking back upon the past five years, it was very fortunate to meet him at first and his endless curiosity and patience have encouraged me to see many surprises. He is a real mentor and friend with his heart. I would also like to thank Cecilia for her generous support.

I wish to acknowledge my thesis committee for their useful comments and suggestions: Dr. Pual Manye, Dr. Susan Burns, Dr. Robert Bachus, and Dr. Guillermo Goldsztein. Especially I would like to thank Dr. Joseph Cartwright for advices and great experiences. I also appreciate Dr. Seung-Rae Lee for all the opportunities during my Master degree.

I want to thank the past and current members of the Particulate Media Laboratory for their help and encouragement: Jong-Sub Lee, Hyunki Kim, Tae-Sup Yun, Guillermo Narsilio, Joo-Yong Lee, Veronica R. Landa, Ahmed M. Bayoumi, Jongwon Jung, Douglas D. Cortes, Jaewon Jang, Changho Lee, D. Nicolas Espinoza, Seunghee Kim, Minsu Cha, Sheng Dai, César Pastén, Harshad Phadnis, and Rafael Monroy. I would also like to thank Sungsoo Yoon, Jongwon Choi, Jonghee Lee, and Duhwan Kim.

Finally, I want to thank my parents and parents-in-law for their confidence in me and dedicated support. Above all, I want to think my wife Somin, daughter Jiwon, and son Seungmin for all their love, sacrifice and patience.

TABLE OF CONTENTS

LIST OF TABLES

LIST OF FIGURES

Page

SUMMARY

Discontinuous planes often develop in soils; examples include shear bands, desiccation cracks, polygonal faults, and hydraulic fractures. These discontinuities affect the mechanical behavior (stiffness and strength) and transport properties of sediments (fluid migration and diffusion). Contrary to discontinuities in solid materials, granular materials such as soils are already separated at the particle scale. Therefore, the fundamental understanding of the development of discontinuities in soils must recognize their inherent granular nature and effective-stress dependent behavior. This research focuses on particle-scale mechanisms involved in contraction-driven shear failure due to mineral dissolution, desiccation cracks, and hydraulic fractures. Complementary experimental, analytical and numerical methods are used to study three cases.

Contraction-driven polygonal fault formation under the seabed. Shear failure planes are often found in sediments that formed under near horizontal burial conditions. Particle-scale volume contraction due to mineral dissolution causes a decrease in the state of stress from the insitu K_0-condition to the active failure K_a stress field. Shear strain localization follows in sediment with post-peak strain softening response.

Desiccation cracks in saturated fine soils. The formation of desiccation cracks in soils is often interpreted in terms of tensile strength, which contradicts the cohesionless, effective stress dependent frictional behavior of fine grained soils. Experimental results monitored using high resolution time lapse photography point to a proper effective stress-dependent mechanism centered on the invasion of the air-water interface membrane.

Miscible and immiscible fluid-driven fracture formation. Hydraulic fracture in granular materials cause grain separation and the development of conduits for preferential fluid flow leading to fracture formation due to the forced invasion of either immiscible or miscible fluids. Capillary, seepage, and skeletal interparticle forces define particle scale mechanisms at the fracture tip.

Numerical simulations confirm that the effective stress remains in compression everywhere throughout the granular medium in the three localization mechanisms.

CHAPTER 1

INTRODUCTION

The failure of geotechnical systems is often accompanied by the formation and propagation of discontinuous planes which are generally regarded as failure condition. Discontinuities imply the formation of two characteristic planes involving discontinuous kinematical fields, where the deformation is not homogeneous anymore (Houlsby and Wroth 1980).

Soils are granular materials; the particle fabric and pore structure determine the mechanical and hydraulic properties of the soil mass. Strain localization planes in the granular mass can develop along sedimentation planes, or by changes in boundary and loading conditions that cause positive feedback and a runaway effect. These localizations have profound practical relevance because stability and deformation characteristics of geo-structures are often controlled by the presence of discontinuities that act as either weak zones or preferential paths for gas or fluid migration.

The development of discontinuities in granular materials has attracted much research attention, and various modes of failure have been identified, including open, closed, and shear discontinuities. Specific examples include shear bands, desiccation cracks, polygonal fault systems, ice lenses, hydraulic fractures, and grouting-induced fractures (Table 1.1).

This research pursues a fundamental particle and pore scale understanding of localization mechanisms associated to mineral dissolution, desiccation cracks and hydraulic fracture. The study is organized into 5 chapters as follows:

Dissolution is a ubiquitous phenomenon in soil diagenesis; however, we have no understanding of its implications on the initial state of stress in a soil mass. Chapter 2

documents a study of the evolution of K_0 during grain dissolution using both experimental and numerical methods.

Chapter 3 explores the possible consequences of grain dissolution in a soil mass that reaches failure conditions under zero-lateral strain, with emphasis on the possible development of strain localization and polygonal fault systems.

Chapter 4 develops a new understanding of desiccation crack initiation and propagation in granular materials, focusing on the invasion of the tensile membrane at the water-air interface as suction increases from water evaporation on the soil surface.

Chapter 5 extends in Chapter 4 to the case of fluid-driven fracture initiation and propagation caused by the forced invasion of immiscible fluids.

Chapter 6 is devoted to the study of strain and displacement fields for the case of contraction-driven shear faults under zero-lateral strain conditions.

The most relevant conclusions from this study are summarized in Chapter 7.

Table 1.1 Discontinuities in granular materials

Shear bands 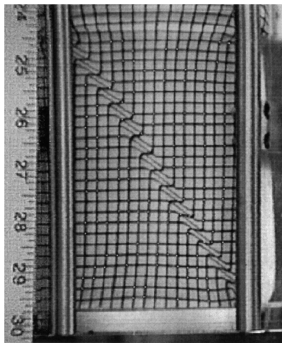 Localized deformation within thin zones of intense shearing in soils (Alshibli and Sture, 2000 –sand in plane strain condition)	Desiccation cracks  Open fractures, typically in the context of non-uniform drying or boundary restrained free shrinkage (pro.corbis.com)	Polygonal faults system 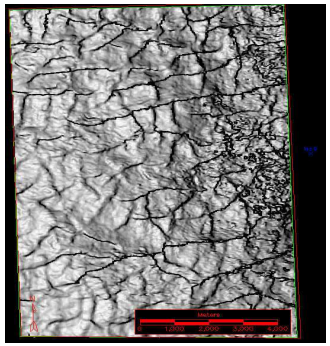 Polygonal networks of shear faults in layer-bound sequences of fine-grained layers formed without regional tectonic extension under zero lateral strain condition (Cartwright, 2005-North Sea)
Ice lenses 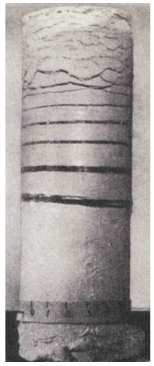 Formation of discrete ice layers in freezing soils, as a result of the migration and subsequent freezing of pore fluid in fine-grained soils (Taber, 1930)	Hydraulic fracture 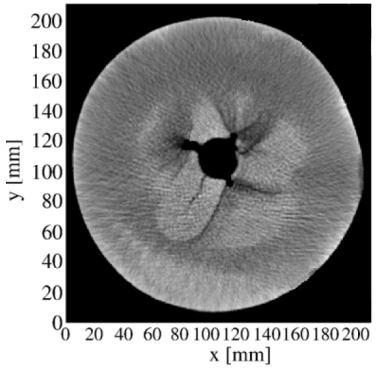 Creation of open flow channels in granular media (Bohloli and de Pater, 2006-sand with bentonite slurry).	Grouting induced fracture 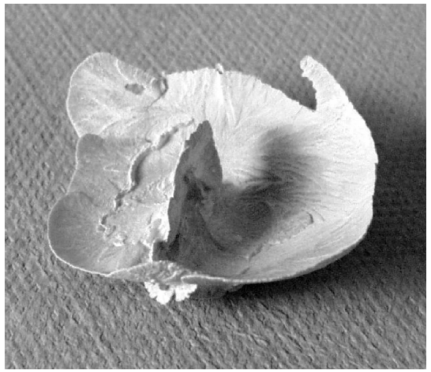 Different grout injection mechanisms depend on particle size and grout rate (Soga et al., 2006 - kaolin with epoxy).

CHAPTER 2

MINERAL DISSOLUTION AND THE EVOLUTION OF K_0

2.1 Introduction – Previous studies

The current stress level in the ground has important effects on the load-deformation response of soils and the performance of engineered geosystems. Hence, the stress ratio K_0 between the horizontal and the vertical effective stresses under zero lateral strain conditions is an important parameter in analysis and design.

The value of K_0 reflects soil characteristics and stress history. Theoretical and empirical relationships have been proposed to estimate K_0. Jaky's equation is widely used for non-preloaded sediments (Jaky 1944; Michalowski 2005):

$$K_{0<NC>} = 1 - \sin(\phi) \qquad \text{NC: non-preloaded} \qquad (2.1)$$

where ϕ is the constant volume friction angle. Jaky's expression does not invoke stress level (explicitly) in agreement with experimental observations in the absence of grain crushing or contact creep (Note: higher K_0 values are observed in looser soils - Bishop and Eldin 1953, Andrawes and El-Sohby 1973). It is interesting to note that K_0 is a function of the frictional resistance of the soil, even though the state of stress is away from the failure state (Feda 1984; Michalowski 2005). This being said, the decrease in K_0 with increasing friction angle captured in Jaky's equation is consistent with the asymptotic value K_0 =1.0 for ϕ=0, i.e., the hydrostatic state in fluids (Mesri and Hayat 1993), and compatible with equivalent continuum models such as the modified Cam Clay that take compressibility into consideration (Roscoe and Burland 1968; see discussion in Muir Wood 1990).

The preloading of frictional granular material leaves residual horizontal stresses locked in. Therefore, the prediction of K_0 during unloading must take into consideration the preload ratio or OCR (Prŭska, 1973),

$$K_{0<OC>} = K_{0<NC>} OCR^{m} \qquad \text{OC: preloaded} \qquad (2.2)$$

where the at-rest rebound parameter of the soil m is often related to friction, e.g., $m=\sin(\phi)$ (Mayne and Kulhawy 1982).

In uncemented soils, the lower limit for K is the active stress coefficient K_a, and the upper limit is the passive stress coefficient K_p (Abdelhamid and Krizek 1976; Brooker and Ireland 1965; Feda 1984; Mayne and Kulhawy 1982); for example, K_0 in OC London clay approaches K_p (Mayne and Kulhawy 1982; Skempton 1961).

The value of K_0 increases with increasing plasticity in NC fine-grained soils (Brooker and Ireland 1965), but the trend may be very weak (Kulhawy and Mayne 1990); different fabrics and pore solution have a secondary effect (Abdelhamid and Krizek 1976). The evolution of K_0 during secondary compression under no lateral strain is controversial. A decrease in K_0 could be expected due to the increase in strength with aging (see discussion in Schmertmann 1983). On the other hand, theoretical creep analyses and limited experimental data predict an increase in K_0 in NC soils, approaching $K_0 \approx 1.0$ with time (Kavazanjian and Mitchell 1984), yet, there are other experimental results that show a seemingly constant value of K_0 during secondary compression (Holtz and Jamiolkowski 1985; Jamiolkowski et al., 1985).

Limited data are available for the evolution of K_0 during drying (Slatter et al. 2005). The value of K_0 remains constant before air-entry (lateral boundary conditions must be corrected or compensated for suction – required when interpreting Slatter et al. 2005 data). Once suction exceeds the air entry value, the total horizontal stress decreases as suction increases; the evaluation of K_0 in this region is conditioned by the definition of effective stress. The evolution of K_0 during cementation depends on the contractive strain

the cementing agent may impose on the granular matrix. If the soil is cemented at low effective confinement $\sigma_z' = \alpha$, further zero-lateral-strain loading to $\sigma_z' = \beta > \alpha$ takes place at a very low K_0 value (even lower than K_a for the uncemented sediments) (Berre et al. 1996; Zhu and Clark 1995). Finally, if the cement is dissolved while the applied vertical effective stress is maintained at $\sigma_z' = \beta$, the value of K_0 will increase towards the K_0 value that corresponds to the uncemented soil (Castellanza and Nova 2004).

There is no information on the evolution of K_0 in soils that have experienced post-depositional grain dissolution, which is a common diagenetic process in a wide range of geological systems (Weaver 1989; Herrera et al. 2007; Zhang et al. 2007). The purpose of this study is to investigate the evolution of K_0 during mineral dissolution and to identify underlying particle level processes using a combination of experimental and numerical methods.

2.2 Experimental study

2.2.1 Test device

Various procedures have been devised to measure K_0. In all cases, the radial strain must be kept smaller than $\varepsilon_r < 5 \times 10^{-5}$ to reduce errors in K_0 to less than 0.01 (Okochi and Tatsuoka 1984). Triaxial-type methods involve a flexible lateral boundary and a sensitive feed-back system to create the zero lateral deformation condition (Ting et al. 1994). Alternatively a thin wall “soft” oedometer may be designed to permit small lateral deformation to measure the horizontal stress using strain gauges, yet within the allowable strain range of $\varepsilon_r < 5 \times 10^{-5}$ to maintain proper K_0 conditions (Kolymbas and Bauer 1993). Soft oedometers have been used to evaluate weathering (Castellanza and Nova 2004) and drying effects on K_0 (Slatter et al. 2005).

The soft oedometer built for this study consists of a thin aluminum shell with inside diameter 66mm and wall thickness 0.13mm (Figure 2.1a). Porous stones are embedded in the top cap and bottom plate. Deaired water flow is imposed from the bottom of the cell (inlet port) and out through the top cap (outlet port). The nominal specimen height is 40mm. The vertical settlement of the top cap is measured using an LVDT. Tangential strains are measured using two strain gages located at the mid-height of the specimen (two dummy gages are included for temperature compensation). The allowable stress level is determined to satisfy the $\varepsilon_r < 5\times10^{-5}$ strain criterion. The soft oedometer is calibrated using a water filled balloon inside the cell so that the known vertical stress applied onto the top cap is equal to the horizontal stress; calibration results are shown in Figure 2.1b.

The effects of top and bottom boundary conditions and specimen height on measured tangential strains in the horizontal direction (i.e., strain gage reading) are numerically evaluated using finite element simulations. The aluminum cell is modeled as an axi-symmetric, linear-elastic material (Young's modulus, E = 69GPa, Poison's ratio, ν = 0.3). The soil pressure against the wall is simulated as either normal stress only (σ_r, τ=0), or both normal and longitudinal shear stresses (σ_r, τ=0.5×σ_r). Furthermore, fixed and free boundary conditions are considered at the bottom of the wall. Simulation results show that top and bottom boundary conditions have minimal effect on the tangential strains measured at mid-height when the specimen height to diameter ratio is H/D ≈ 0.6, while the longitudinal side friction during sediment settlement causes a change in the strain gauge reading smaller than 2%.

2.2.2 Test procedure

Changes in K_0 during dissolution are investigated using mixtures of glass beads (d_{50} = 0.7mm, spherical shape) and various percentages of table salt (d_{50} = 0.3mm, cubical shape). The two grains are mixed under a salt-saturated brine to prevent

dissolution, and scooped into the oedometer cell. The prepared specimen is subjected to vertical loading to 40 kPa. Then, deaired water is allowed from the bottom of the cell to gradually dissolve the salt in the specimen. Water flow is continued until constant specimen height and horizontal stress are reached. When the initial amount of salt is divided by the total volume of water flushed through each specimen, the average concentration is lower than 0.4mol/L in all tests, which is much lower than the saturation concentration 6 mol/L. Asymptotic stress, stable deformation and low concentration suggest that full grain dissolution and mass removal was attained in the tests.

2.2.3 Results

The evolution of vertical strain and K_0 are plotted versus time in Figure 2.2 for mixtures prepared with a volume of salt divided by the total volume of solids V_S/V_T=0%, 5%, 10%, and 15%. Tests were repeated 2 to 5 times for each mixture.

Experimental results show the intricate evolution of K_0. The specimen without salt remains at a constant horizontal stress $K_0 \approx 0.53$ and exhibits no settlement during fluid replacement. All specimens with salt experience a decrease in K_0 during dissolution and reach a minimum value K_{min}. The final K value after dissolution is lower than the initial value before dissolution in specimens with 5% salt fraction. However, specimens with 10% and 15% salt fraction exhibit multiple oscillations in K_0; eventually, the horizontal stress recovers from the minimum K_{min} to end near the initial value K_0 when dissolution ends.

Results for 5 similar specimens prepared with 10% salt are summarized in Figure 2.3. As observed above, there is pronounced variability in the minimum and final stress ratios K. Jaky's equation $K_0=1-\sin(\phi)$ and Rankine's active coefficient equation $K_a=\tan^2(45°-\phi/2)$ are computed using the friction angle determined from the angle of repose method (as in Santamarina and Cho 2001): the measured angle of repose for the glass beads is $\phi=25\pm0.5°$ and it is not affected by the presence of soluble salt for $V_S/V_T \leq$

25%. Computed values are superimposed on Figure 2.3. The estimated K_0 matched the initial and final values, while the measured K_{min} is in the range of the active earth pressure coefficient K_a.

The measured settlement is normalized by the initial specimen height and plotted versus the volume fraction of salt in Figure 2.4. The measured vertical strain is much lower than the volume fraction of dissolved particles.

2.3 Discrete element simulations

2.3.1 Methodology

The discrete element method is used to gain particle level insight into the consequences of mineral dissolution. The 2D simulation involves 9,999 disks with 25% standard deviation in particle size (PFC-2D, Itasca). The packing is subjected to vertical confinement under zero lateral strain and no friction is assumed between particles and walls ($\sigma_z/K_n = 10^{-3}$, where K_n [N/m^2] is normal contact stiffness). Then a servo-control function is used to maintain the vertical stress constant during dissolution. Simulations are repeated for the following volume fraction of particles subjected to contraction: 5%, 10%, 15%, 20%, 30%, 40% and 50%. Dissolution is simulated by decreasing the particle size (Note: preliminary simulations were conducted by reducing the shear modulus and produced similar trends).

2.3.2 Results

Typical simulation results are summarized in Figure 2.5. The following observations can be made: (1) general trends agree with experimental results presented in Figure 2.2, (2) dissolution causes vertical settlement and an early decrease in horizontal stress, (3) the final K is lower than the initial K_0 in tests with less than 15% dissolving particles and both settlement and horizontal stress stabilize at an early stage, (4)

horizontal stress recovery takes place when the volume fraction of dissolving particles exceeds 15%, (5) both experimental (Figure 2.2) and numerical results (Figure 2.5) show quite smooth vertical settlement in all cases, while rough changes in horizontal stress take place in large V_S/V_T specimens.

The changes in the anisotropy of internal parameters is recorded in all simulations: a_c captures contact anisotropy ($1+a_c\cos2\theta$), a_n normal force anisotropy ($1+a_n\cos2\theta$), and a_t shear force anisotropy ($a_t\sin2\theta$). Figure 2.6 shows the evolution of each parameter for the simulation with a 20% volume fraction of dissolving particles. Anisotropy is most pronounced in normal contact forces a_n. The three parameters a_c, a_n, and a_t reach a peak in anisotropy as the medium approaches the minimum value in the lateral stress coefficient.

Figure 2.7 shows statistical summaries of micro-mechanical parameters in the form of polar plots at the initial state ("a" in Figure 2.6), at the minimum horizontal stress during dissolution ("b" in Figure 2.6), and at the final state after dissolution ("c" in Figure 2.6) for the simulation with 20% volume fraction of dissolving particles. The polar plots confirm the increased anisotropy in contacts, normal and shear forces reported in Figure 2.6. Furthermore, profound differences in fabric are observed between the initial and the final stages (not detected in statistical summaries): marked force chains, a "honeycomb fabric", and force arches characterize the fabric after dissolution. Therefore, while the stress ratio K is similar before and after dissolution in this simulation (Figure 2.6), the internal fabric is distinct and a different sediment response is anticipated upon further loading.

Figure 2.8 shows the final settlement obtained in the simulations with different volume fractions of dissolving particles. Analogous to experimental data (Figure 2.4), strains are small for low V_S/V_T ratios, but increase significantly thereafter (for V_S/V_T=20% in these 2D-simulations).

2.4 Discussion

2.4.1 Vertical settlement during dissolution

Assuming the same void ratio before and after dissolution, the strain due to dissolution would be (Note: very loose materials could densify during dissolution):

$$\varepsilon_z = \frac{1}{1+\frac{G_S M_{GB}}{G_{GB} M_S}} = \frac{V_S}{V_T} \tag{2.3}$$

where subscripts GB and S denote “glass bead” and dissolving granular "salt” respectively, V_S is the volume of salt and V_T is the initial total volume of solids. The predicted strain is superimposed on experimental and numerical results in Figure 2.4 and 2.8. The measured strains are much smaller than the strain estimated using Equation 2.3; this is agreement with the development of load carrying grain arches around the dissolving particles and the increase in internal porosity loading to the honeycomb fabric. In particular, the final vertical strain ε_z is small at low V_S/V_T ratios, however strains track grain dissolution at high volume fractions above a certain V_S/V_T threshold. Therefore, it appears that a limiting porosity or “terminal density” is reached during dissolution so that further dissolution must be accompanied by volume collapse. The V_S/V_T threshold is higher in the 2D simulations ($V_S/V_T \approx 20\%$) than in the 3D-experimental results ($V_S/V_T \approx 10\%$), probably due to inherent differences in particle mobility in 2D and 3D systems.

2.4.2 Stiffness evolution

Truong et al. (2009) conducted complementary tests using mixtures of silica sand and soluble salt to study the evolution of stiffness during dissolution. They observed a marked decrease in shear wave velocity and small strain shear modulus during particle dissolution; furthermore, they found that stiffness does not recover to the before-dissolution trend but remains low upon further K_0-loading. These results agree with the

reduction in lateral stress (transient in high V_S/V_T mixtures) and the higher final void ratio (all mixtures) observed in our experiments and numerical simulations.

2.4.3 Smooth settlement and episodic K changes

Both experimental and numerical results show that vertical settlement evolves smoothly during particle dissolution, while the measured horizontal stress shows more dramatic episodic changes (see Figure 2.2 and 2.5). While stick-slip behavior between wall and ductile grains can produce oscillation in vertical stress measurements during self-weight deformation (H/D=1 to 4 and D/d=3.4 to 7.6, Uri et al. 2006), a smooth settlement response is observed in all our experiments suggesting minimal side wall friction effects on both settlement and horizontal stress measurements (in agreement with the low H/D ratio used in this study - Ovarlez and Clement 2003). Therefore, an alternative explanation is sought herein.

Insight is gained by studying the changes in internal anisotropy parameters: the granular fabric must be continuously evolving to sustain the applied vertical stress while grain dissolution takes place. Indeed, Figure 2.9 shows that sudden increases in micro-mechanical anisotropy parameters a_n, a_t, and a_c accompany the episodic K drops (Figure 2.5d). Hence, dissolution causes local fabric changes and pronounced changes in force transmission that have an immediate effect on K but a delayed integration into global settlement.

2.4.4 Mobilized friction

The anisotropy in internal parameters can be used to estimate the mobilized shear strength within the particulate medium (Rothenburg and Bathurst 1989):

$$\sin(\phi_{mob}) = \frac{\frac{1}{2}\left(a_c + a_n + a_t\right)}{1 + \frac{a_c a_n}{2}} \qquad (2.4)$$

The evolution in mobilized friction during dissolution is superimposed on the plot for horizontal stress change in Figure 2.6. Results show that K_0 reaches the minimum value when the mobilized friction angle is maximum. The mobilized friction ϕ_{mob} confirms that internal shear failure conditions may be reached during dissolution.

2.4.5 Macroscale effects

It can be shown following Rudnicki and Rice (1975) that shear localization may take place during mineral dissolution in sediments that exhibit post-peak strain softening (details in Shin et al. 2008). This could explain the formation of polygonal fault systems observed in offshore basins worldwide (Cartwright and Dewhurst 1998), as well as the development of internal shear planes in volcanic ash soils which evolved onshore from the in-situ dissolution of wind transported volcanic ash (Herrera et al. 2007).

2.5 Conclusions

The in-situ state of stress under zero lateral strain conditions, captured in the K_0 parameter, is a complex consequence of sediment properties and the formation history of natural sediments. Empirical equations fail to capture the effects of formation history, and there is limited information related to the post depositional evolution of K_0 during soil diagenesis in particular as a consequence of mineral dissolution. Experiments and discrete element numerical simulations reported in this manuscript help gain insight into the effect of mineral dissolution on internal stress and deformation.

Mineral dissolution under zero lateral strain and constant vertical stress results in horizontal stress decrease. The minimum horizontal stress coefficient K_{min} can be as low as Rankine's active earth pressure coefficient. Discrete element simulation results confirm that the internal friction is fully mobilized at K_{min}. Hence, internal shear failure can be reached during grain dissolution.

A small amount of dissolving particles is sufficient to trigger the horizontal stress drop. If the volume of dissolving particles V_S/V_T is small, there is no stress recovery and the change in void ratio is very minor. Once a threshold value V_S/V_T is exceeded, the horizontal stress recovers, a low terminal density is reached and the vertical strain increases proportionally to the amount of dissolving particles.

Mineral dissolution involves rearrangement of the internal granular structure. While the lateral stress coefficient may be similar before and after dissolution (i.e., a medium with V_S/V_T above the threshold value), the internal fabric is quite distinct and it is characterized by a honeycomb structure with pronounced force chain arching.

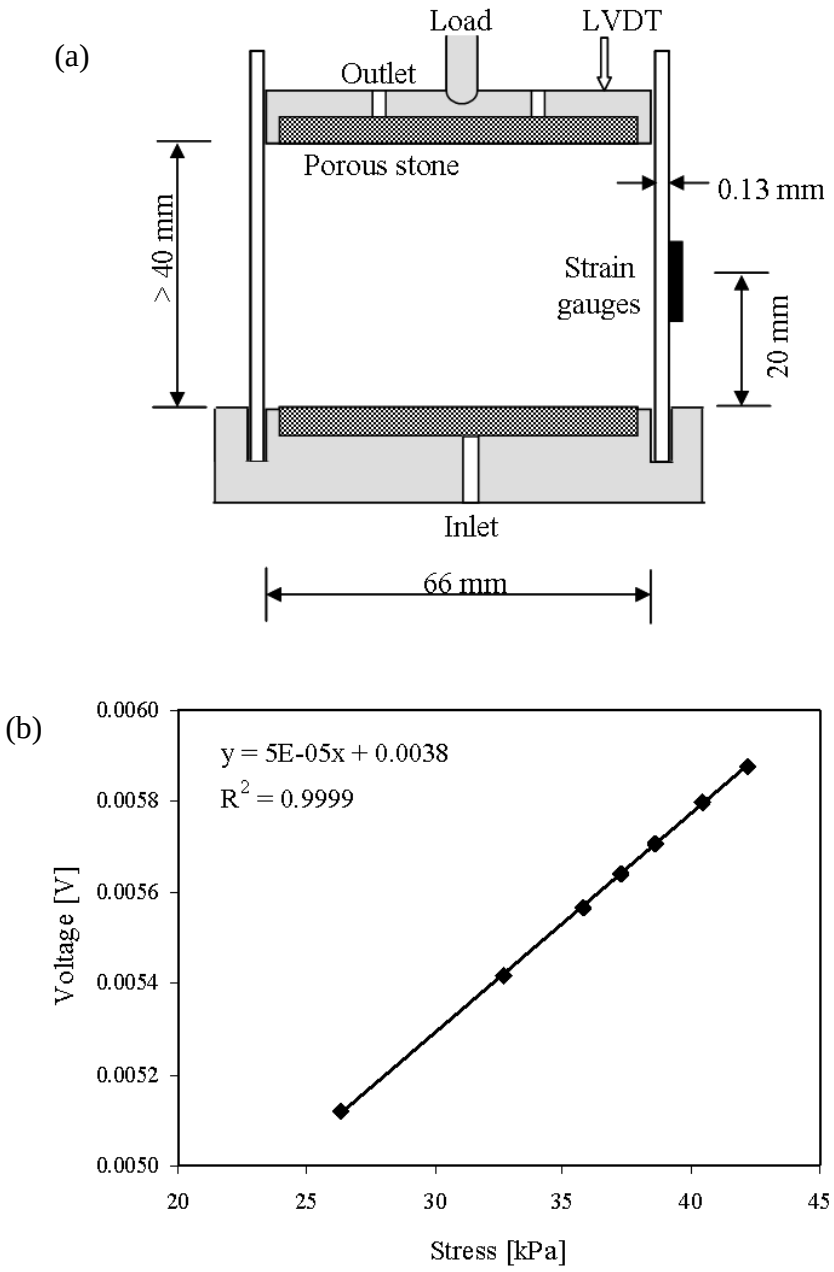

Figure 2.1 Device and calibration. (a) Soft oedometer. (b) Lateral stress calibration.

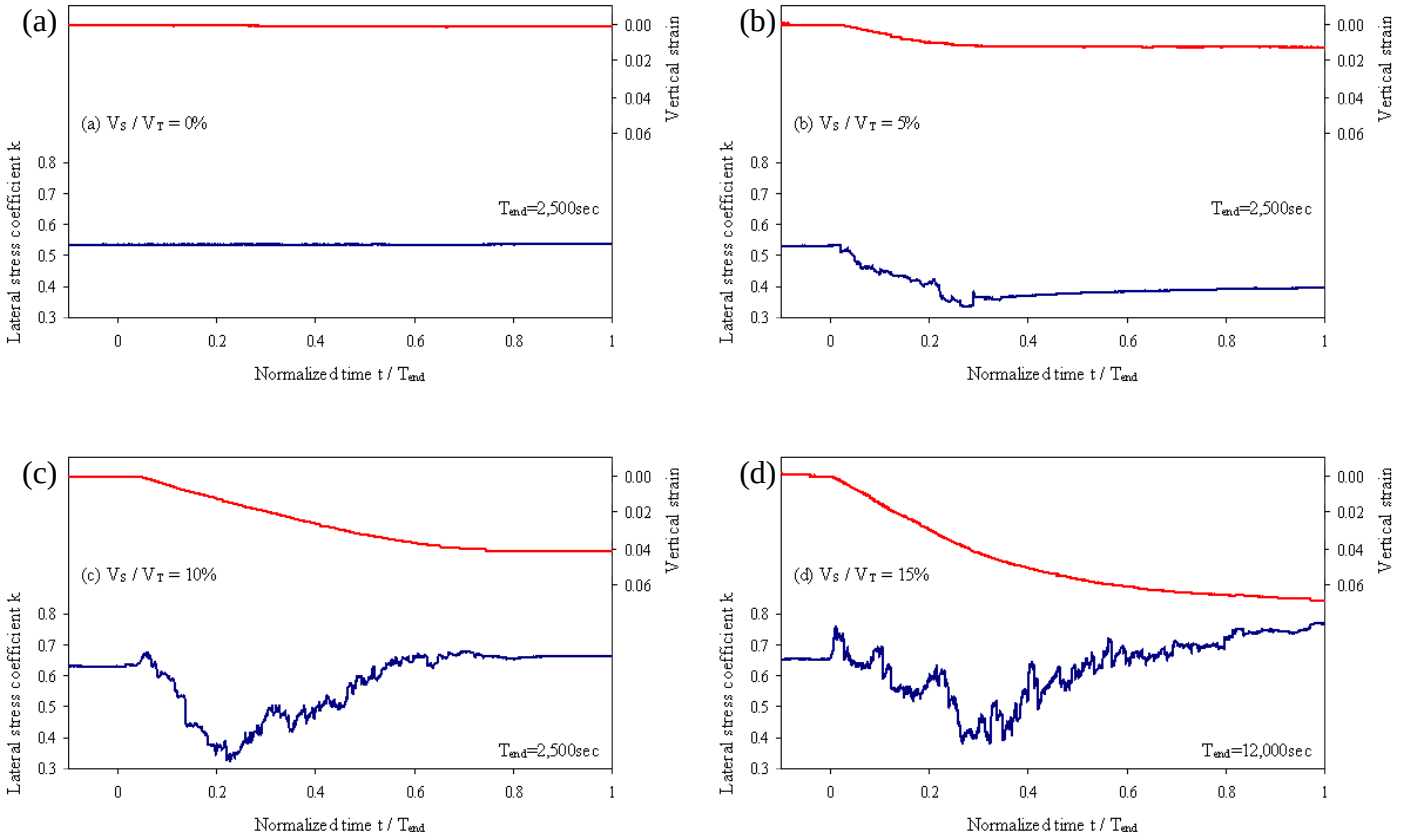

Figure 2.2 Dissolution tests – Evolution of settlement and lateral stress coefficient K in time. Mixtures with volume fraction of salt $V_S/V_T=V_S/(V_{GB}+V_S)$: (a) 0%, (b) 5%, (c) 10%, and (d) 15% salt.

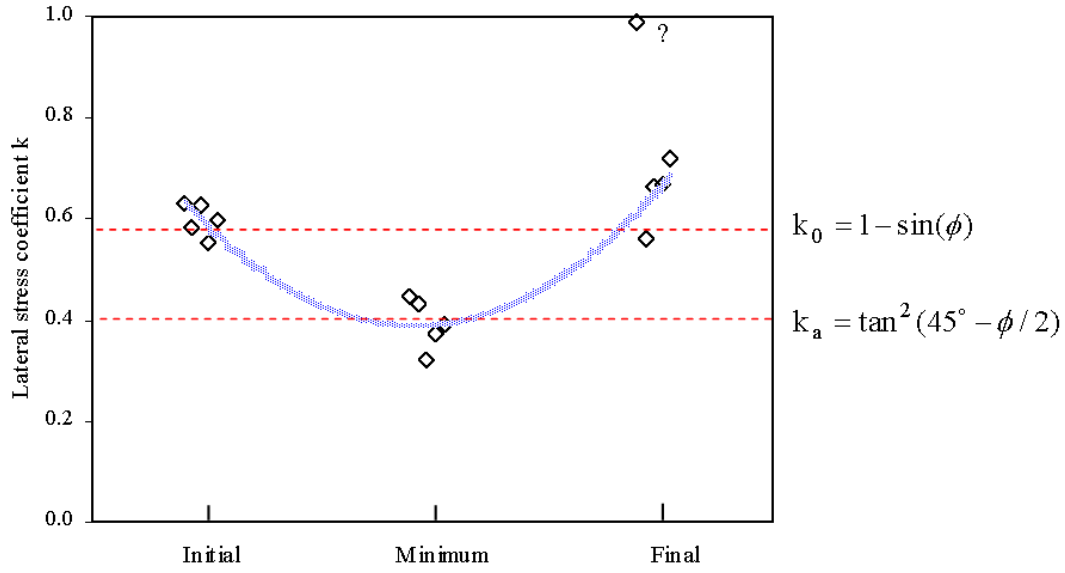

Figure 2.3 Variation of lateral stress coefficient K during dissolution. Set of 5 tests run on similar specimens made of V_S/V_T = 10%. Lateral stress coefficient at before, during, and after dissolution. Estimated Jaky's K_0 and Rankine's K_a are shown for a mixture friction angle of ϕ=25°.

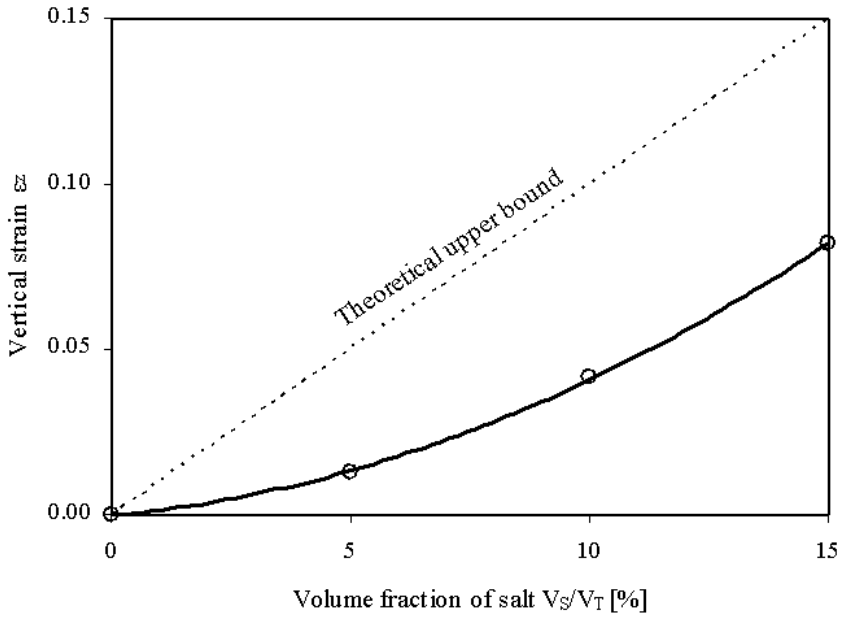

Figure 2.4 Experimentally determined vertical strain at the end of dissolution as a function of the volume of dissolving particles, V_S/V_T. The theoretical upper bound is estimated assuming that the void ratio is the same before and after dissolution.

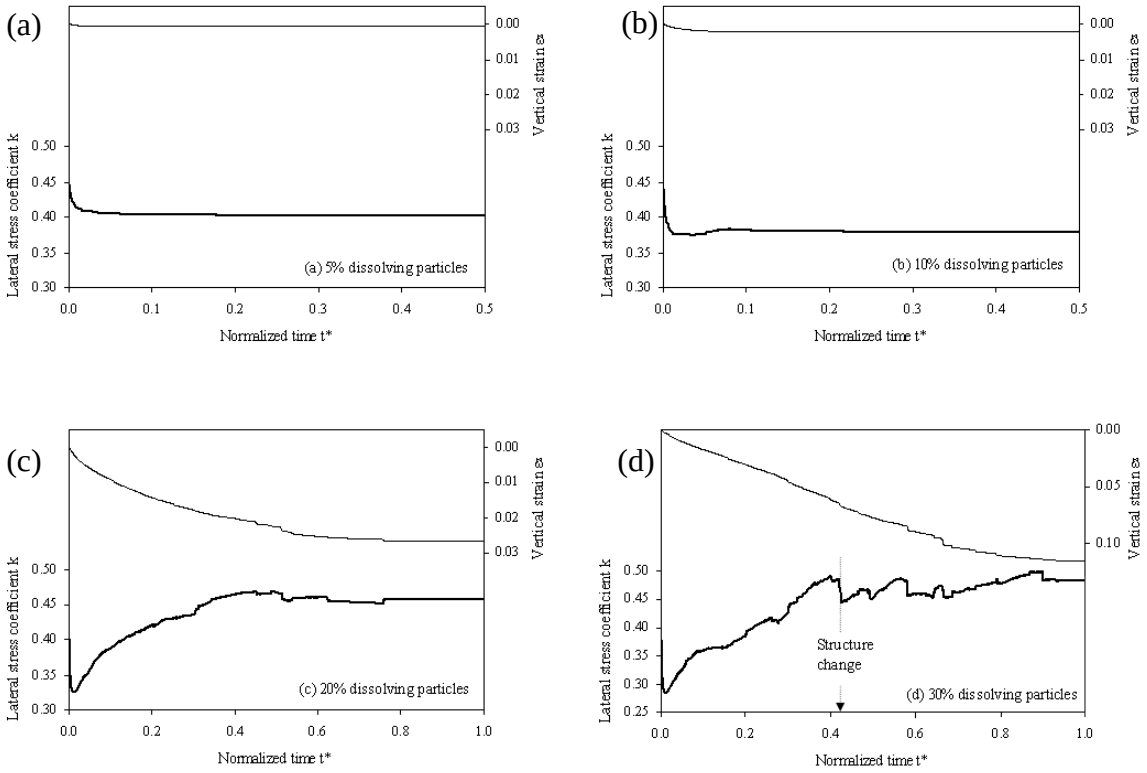

Figure 2.5 DEM simulation. Evolution of settlement and lateral stress coefficient during particle dissolution. The normalized time t* is the current time step divided by the time at 100% dissolution. Volume fraction of dissolving particles V_S/V_T: (a) 5%, (b) 10%, (c) 20%, and (d) 30%. Simulation conditions: inter-particle friction μ= 0.5, standard deviation in particle radius 25%, hindered particle rotation.

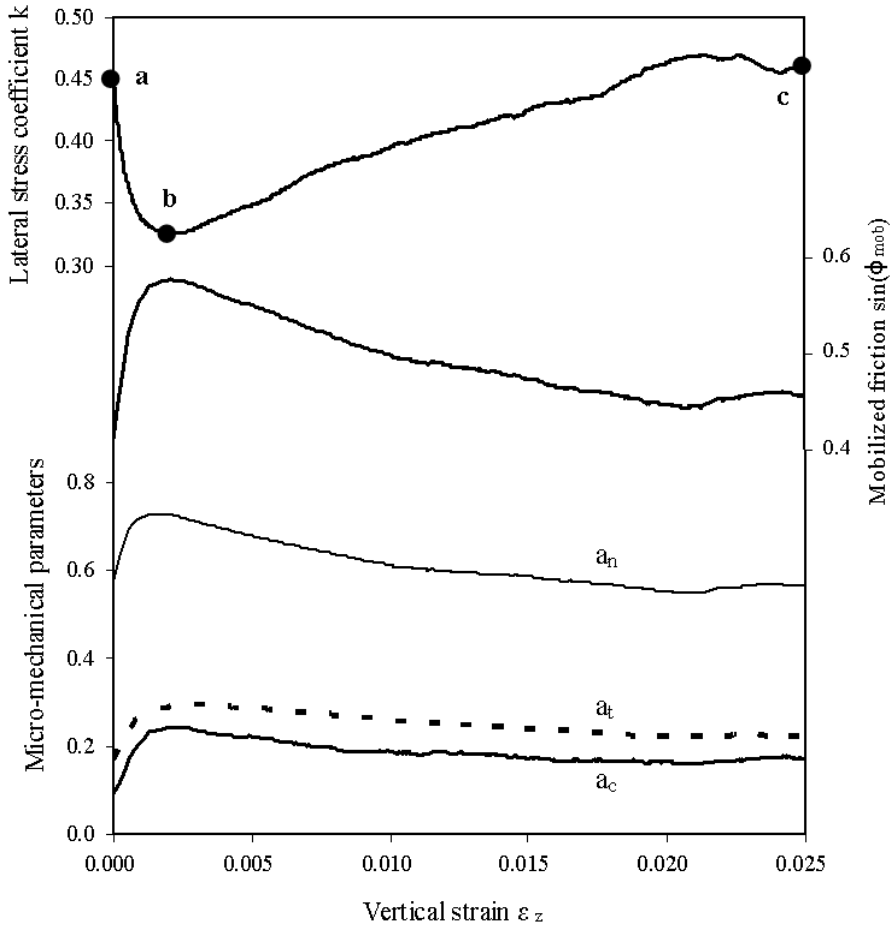

Figure 2.6 DEM simulation. Evolution of horizontal stress coefficient, mobilized friction $\sin\phi_{mob}$ and micro-mechanical parameters during dissolution. Simulation conditions: inter-particle friction μ= 0.5, hindered particle rotation, volume fraction of dissolving particles 20%.

Stages in Fig. 6	(a) Before dissolution	(b) During dissolution at k minimum	(c) After dissolution
Chains of contact normal forces	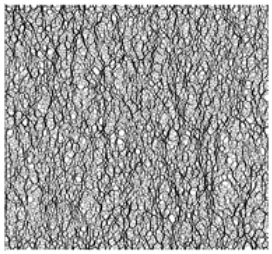	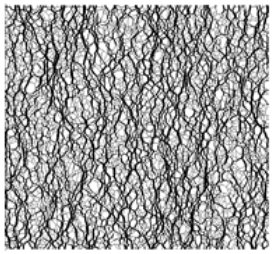	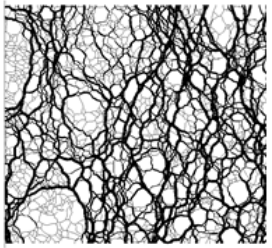
Number of contacts	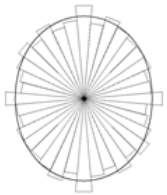	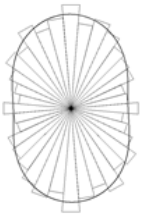	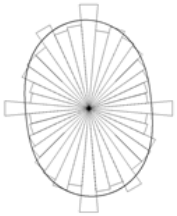
Average normal contact forces			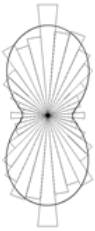
Average tangential contact forces		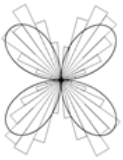	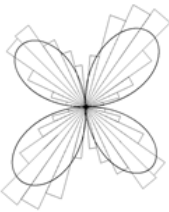
k	0.45	0.33	0.46
$\sin(\phi_{mob})$	0.41	0.58	0.46

Figure 2.7 DEM simulation. Fabric and polar plots of internal micro-mechanical parameters before, during, and after dissolution – Refer to Figure 2.6 for stages a, b, and c (20% volume fraction of dissolving particles).

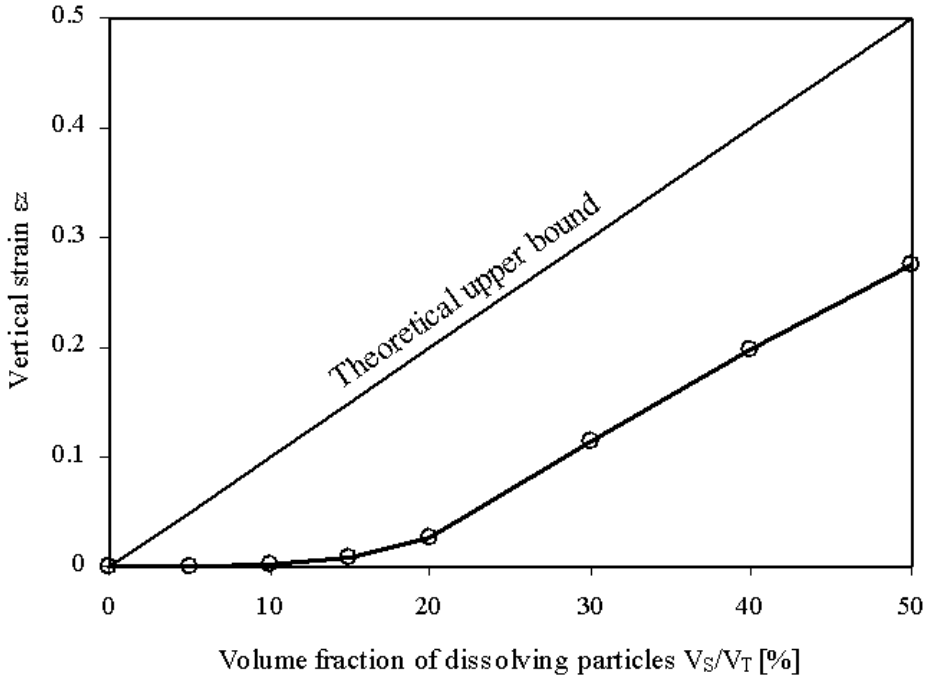

Figure 2.8 DEM simulation. Vertical strain at the end of dissolution as a function of the volume fraction of dissolving particles V_S/V_T. The theoretical upper bound presumes that the void ratio is the same before and after dissolution.

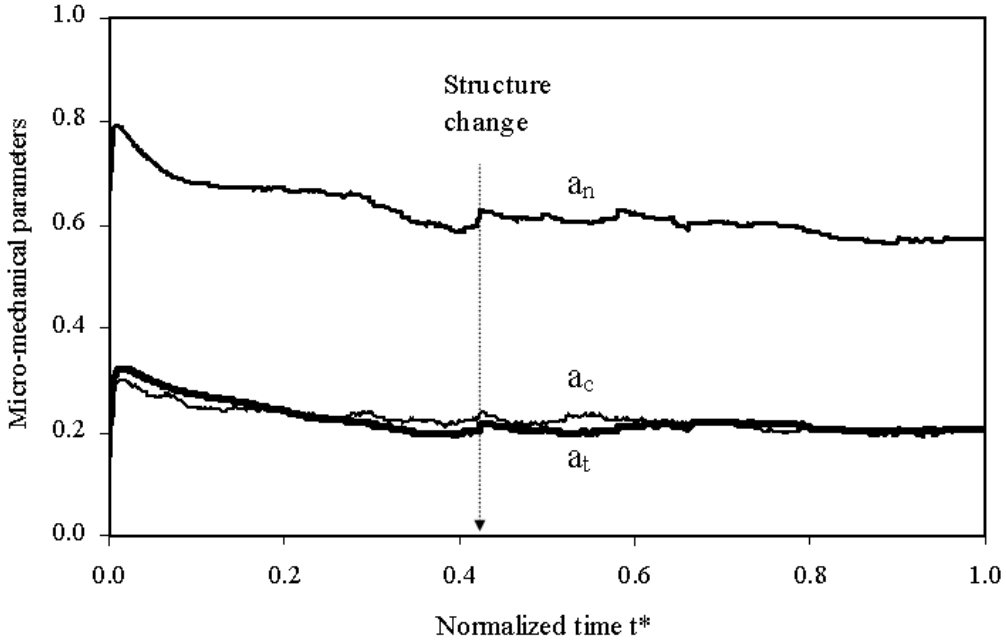

Figure 2.9 DEM simulation. Evolution of micro-mechanical parameters during dissolution. The corresponding trends for settlement and lateral stress coefficient K are shown in Fig. 2.5d. Notice the jump in K at t*=0.42 in Fig. 2.5d and the corresponding structure change in this figure. Simulation conditions: inter-particle friction μ= 0.5, volume fraction of dissolving particles 30%.

CHAPTER 3

CONTRACTION-DRIVEN SHEAR FAILURE IN COMPACTING UNCEMENTED SEDIMENTS

3.1 Introduction

Shear failure in sedimentary rocks is a fundamental process in all sedimentary basins, and leads to the growth of all types of geological faults (Jaeger and Cook, 1976). Shear failure is not considered possible under normal geomechanical burial conditions that typify basin evolution unless there is a modification of the state of stress by the addition of tectonic stresses (either regional or local, such as due to local flexure or tilting). Furthermore, classical geomechanical theories predict that sediment compaction under zero-lateral strain conditions takes place at a quasi-constant ratio between the horizontal effective stress and the vertical effective stress (Terzaghi et al., 1996; the response in structured sediments is discussed in Burland 1990).

Mineral dissolution-and-reprecipitation is a common geological phenomenon that contributes to changes in porosity and sediment compaction (Berner, 1980; Renard et al., 2001; He et al., 2003; Cailly et al., 2005; Herrera et al., 2007; Zhang et al., 2007). Surprisingly, there has been no formal study of the evolution of the internal state of stress in uncemented particulate media (such as sediments) during mineral dissolution. Yet, many regionally extensive fracture networks that occur in sedimentary basins with complex diagenetic histories are often attributed to regional tectonic stresses or to the unloading effects of regional uplift, and the diagenetic history is never implicated in their formation (Engelder, 1993).

The aim of this study is to investigate the changes in the stress state in an uncemented soil or sediment during grain-scale dissolution, and to test whether stress changes induced

by dissolution could lead to shear failure. In contrast to previous investigations of tensile fracturing in cohesive solids caused by dissolution/corrosion (e.g., Yakobson, 1991; Boeck et al. 1999; Malthe-Sorenssen et al. 2006), we focus on uncemented granular sediments that exhibit cohesionless, stress-dependent frictional behavior. We use complementary analytical, numerical and experimental techniques to investigate the effects of particle-level volume contraction on the evolution of the state of stress under constant overburden at zero-lateral strain boundary conditions, and place special attention to the ensuing deformation field and the potential development of shear planes.

3.2 Theoretical considerations

Typically, the state of stress in level-ground sediments under constant vertical load is determined by the displacement of lateral boundaries. Under zero-lateral strain conditions, the coefficient of earth pressure at rest $K_0 = \sigma'_h / \sigma'_z$ between the horizontal effective stress σ'_h and the vertical effective stress σ'_z depends on the friction angle ϕ as predicted by Jaky's equation $K_0=1-\sin\phi$ (Mayne and Kulhawy, 1982; Terzaghi et al. 1996). When lateral boundaries move out, the sediment deforms laterally to accompany the wall movement, the internal shear strength in the sediment is mobilized and the horizontal effective stress decreases to a limiting value that defines the "active" earth pressure coefficient and can be derived from the Coulomb frictional strength of the soil to be $K_a = (1-\sin\phi)/(1+\sin\phi)$.

Analytically, a homogeneous isotropic elastic medium experiences a reduction in horizontal stress from $K_0\sigma'_z$ to $K_a\sigma'_z$ when the volumetric strain in the medium is (see Appendix 3.1).

$$\varepsilon_v = 3\,(1-\nu)\,(K_0-K_a)\,\sigma'_z\,/E \qquad (3.1)$$

The ratio σ'_z /E is a small number in granular materials (on the order of 10^{-3}), therefore, it is anticipated that relatively small volumetric strains can produce significant horizontal stress reduction.

3.3 Numerical and experimental analysis

We conducted a set of finite element simulations to capture the behavior of uncemented particulate sediments subjected to dissolution of a small component of the solid grain fraction (see Table 3.1 for model details). After zero-lateral strain loading, a selected volume fraction of randomly distributed elements v_{cont} was subjected to a volumetric contraction strain ε_v (Figure 3.1). As the volumetric contraction $\varepsilon_v \cdot v_{cont}$ increases, an increasingly higher number of elements reach the Coulomb failure condition within the medium (Figure 3.1a), and the mean horizontal stress at the boundaries lessens so that the global stress ratio $K = \sigma'_h / \sigma'_z$ gradually decreases from K_0 to the failure K_a state. The vertical load applied on the top boundary is homogeneously transferred through the medium before volume contraction; however, as volume contraction develops, the load is preferentially transferred along columns of vertical stress concentration. In all cases, the stress drop takes place at relatively low volume contractions in agreement with Equation 3.1 (Figure 3.1b).

We conducted a complementary experimental study to corroborate the evolution from K_0 to K_a during dissolution in real granular materials, using a simple binary mixture in which one particle type would be prone to dissolution (see details in Chapter 2). We placed a mixture of small glass beads and NaCl salt grains, homogeneously mixed in NaCl brine, inside a calibrated zero lateral strain oedometer cell instrumented with strain gauges to measure the horizontal stress. The evolution of vertical strain was monitored using an LVDT. Edge effects were minimized by keeping the height-to-diameter ratio below 0.6. First, the granular mixture was allow to reach chemo-mechanical equilibrium

under a nominal vertical effective stress: σ'_z = 40 kPa. Then, the fluid concentration was gradually decreased during advective flow resulting in controlled dissolution of the salt grains. Tests were repeated with near-identical boundary conditions but for varying mass fractions of salt m_{salt} (5% to 20%). All test results for the different m_{salt} values show a similar pattern: an initial decrease in horizontal stress followed by a gradual recovery after a minimum value is reached (Figure 3.2).

Discrete element simulations of sediment modeled with the particles satisfying Newtonian equations were run to obtain particle-scale information unattainable in experimental studies. We used both 2D (PFC-2D) and 3D (EDEM) configurations (Cundall and Strack, 1979) and tested different mechanisms that can lead to volume contraction, such as particle stiffness reduction and particle size reduction (see details in Chapter 2). In all cases, we obtained consistent results that resemble the experimental evolution in lateral stress: a drop in the effective stress ratio K followed by horizontal stress recovery. A representative model run is shown in Figure 3.3. The internal mechanisms for the observed lateral stress reduction can be inferred from the evolution of internal parameters of the simulations during particle volume contraction. We observed that the anisotropy in coordination number increases and force chains become increasingly more focused and vertically aligned as particle dissolution takes place. Interparticle coordination and forces reach maximum anisotropy near the minimum value of the effective stress ratio K; thereafter, particle chains start buckling and global contact anisotropy diminishes (Note: while the stress ratio K recovers toward the end of the simulation, the final fabric is quite different from the initial fabric – Figure 3.3b). The evolution in the internal anisotropy of contacts, normal forces and shear forces can be combined to estimate the mobilized friction (Rothenburg and Bathurst, 1989 – Figure 3.3a): the mobilized friction angle reaches the limiting value by the time the horizontal stress ratio approaches the minimum $K = K_a$. Therefore, boundary measurements and

internal parameters corroborate the shear failure of the granular skeleton during mineral dissolution under zero-lateral strain conditions.

3.4 Discussion

3.4.1 Strain localization

Analytical, experimental and numerical results demonstrate unequivocally that particle level contraction can cause a macro-scale stress drop from the initial at-rest K_0-condition to the at-failure K_a-condition, i.e, grain dissolution in a natural environment can advance the uncemented sediment to a state of failure. This has major implications for the potential coupling between diagenetic and deformational processes, but it does not by itself account for fracture development. To properly link grain dissolution to fracture formation, we need to consider the conditions for strain localization.

Shear strain localization and the formation of shear bands reflect the development of an energetically beneficial deformation mechanism whereby less energy is required to deform along a few planes rather than as a homogeneous process that affect the whole sediments mass. Mathematically, shear bands form when the strain hardening h exceeds a critical value h_{cr} in bifurcation theory (Rudnicki and Rice 1975)

$$h = \frac{\partial \sigma_d}{\partial \gamma_{pl}} \tag{3.2}$$

where σ_d is the deviatoric stress and γ_{pl} is the plastic shear strain.

Values of h_{cr} depend on material strength parameters and loading path. In the case of the Drucker-Prager model with shear hardening, the value of h_{cr} can be mathematically predicted (Rudnicki and Rice 1975; Perrin and Leblond, 1993; Lade, 2002)

$$\frac{h_{cr}}{G} = \frac{1+\nu}{9(1-\nu)}(\beta-\mu)^2 - \frac{1}{2}(1+\nu)\left[-N+\frac{1}{3}(\beta+\mu)\right]^2 \tag{3.3}$$

where peak friction and dilation are captured in coefficients $\mu = \tan(\phi)$ and $\beta = \tan(\psi)$, and stress anisotropy is represented by the parameter $N = \sqrt{2}\sigma'_2 / \sqrt{\sigma'^2_1 + \sigma'^2_2 + \sigma'^2_3}$. The extent of strain hardening h a material exhibits also depends on similar soil parameters (packing density and inter-particle friction) and loading path.

In sediments that have experienced particle-level volume contraction, the stress in the vertical direction is the maximum principal stress and the two horizontal stresses are of the same magnitude. For this stress condition, shear faulting occurs in the strain softening regime in homogenous media; therefore, the formation of shear faults associated with volume contraction will take place in materials that exhibit post-peak strength softening (Figure 3.4). This could be the case in the undrained failure of shear-contractive soils or sediments (e.g., fast shear of normally consolidated clays), in the drained shear of sediments with low residual friction angle (from smectites to micaceous sands - Skempton, 1985), or in sediments with some degree of heterogeneity. Under this stress condition (triaxial compression), strain localization develops in a complex pattern because there is no preferred direction for shear localization (Desrues and Viggiani, 2004). The polygonal shape in field observations also reflects the emergence of an exclusion length in the development of localizations.

To gain further insight into the potential development of shear strain localization during particle-level contraction, we conducted finite element simulations of a medium subjected to constant vertical stress under zero lateral strain boundary condition using a Drucker-Prager frictional model with non-associated flow rule. The nucleation of localization was facilitated by creating a correlated random field for volume contraction (see Table 3.1 for model details). Results show diffused strain localization in perfectly plastic media $\phi_{residual} = \phi_{peak}$ (Figure 3.5a) and marked shear strain localization when the medium was modeled with post-peak strength softening $\phi_{residual} < \phi_{peak}$ (Figure 3.5b).

In summary, our results, based on complementary analytical, experimental and numerical analyses, show that particle-level volume reduction in uncemented granular media causes a decrease in horizontal stress, leading to internal shear failure conditions and the potential development of shear strain localization. It is noted, however, that other potential localization mechanisms may develop in relation to cemented soils and soils made of crushable aggregations.

3.4.2 Implications

These results prompt a fundamental re-appraisal of how sediments can fail in shear, and have wider implications for fracture and fault development in sedimentary basins and residual soils. Regional diagenesis of sediments commonly involves loss of granular volume through mineral-specific dissolution. For some of these reactions, well documented linkages already exist between diagenesis and regional fracture development (e.g., the fractured Monterey Formation, Eichhubl et al., 2001). For others, our results may prompt a re-evaluation of the impact of diagenetic reactions on deformation. Furthermore, there is potential coupling between coeval volume contraction, fluid expulsion, and fracture propagation, which can provide a positive feedback with the driving reaction (Davies and Cartwright, 2007. The dissociation of gas hydrates in marine sediments may trigger this sequence of events. Our study also raises questions concerning the long-term stability of engineering solutions such as the geological storage of CO_2 by highlighting the potential for fracturing through acidification of pore fluids and grain dissolution in underground reservoirs (Renard et al., 2005; Le Guen et al., 2007). Finally, the proposed mechanism may offer a simple explanation for the genesis of the enigmatic but widely developed polygonal fault systems (Cartwright and Dewhurst, 1998; Cartwright et al. 2003): the stress history and deformation field that accompanies particle-level volume contraction can account for the development of polygonal faults in

uncemented sediments, and strain-softening behavior (e.g., low residual friction - Goulty, 2001) enhances localization.

Table 3.1 Finite element analysis: Model, material parameters

Boundary conditions:

- Plane strain
- Zero-lateral strain condition on the lateral boundary
- No friction against boundaries
- Element type: 8 node, plane strain element
- Mesh: 100 by 100 elements in Figure 3.1
  140 by 70 element in Figure 3.4

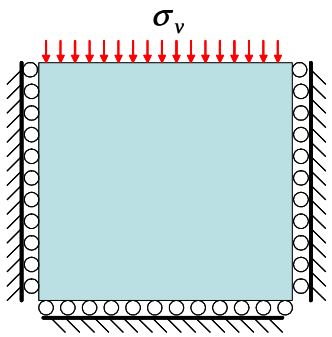

Material properties:

- Constitutive model: Drucker-Prager model with non-associated flow rule
- Host elements: $\sigma'_z/E = 10^{-3}$, Poisson's ratio ν=0.3, friction angle ϕ=30°, ψ=0°
- Contractive elements

  -Figure 3.1: Randomly distributed, the same material properties as host elements, and additional volumetric

  -Figure 3.5: Correlated random field for volume contraction (coefficient of variation 20%; correlation length=20% of the model height, as in Kim and Santamarina, 2008; methodology for correlated random field generation in El-Kadi and Williams, 2000). Perfectly plastic medium $\phi_{residual}=\phi_{peak}$ in Figure 3.5a, Post-peak strength softening medium $\phi_{peak}=30^{\circ}$, $\phi_{residual}=10^{\circ}$, softening modulus h/E=-0.05 in Figure 3.5b.

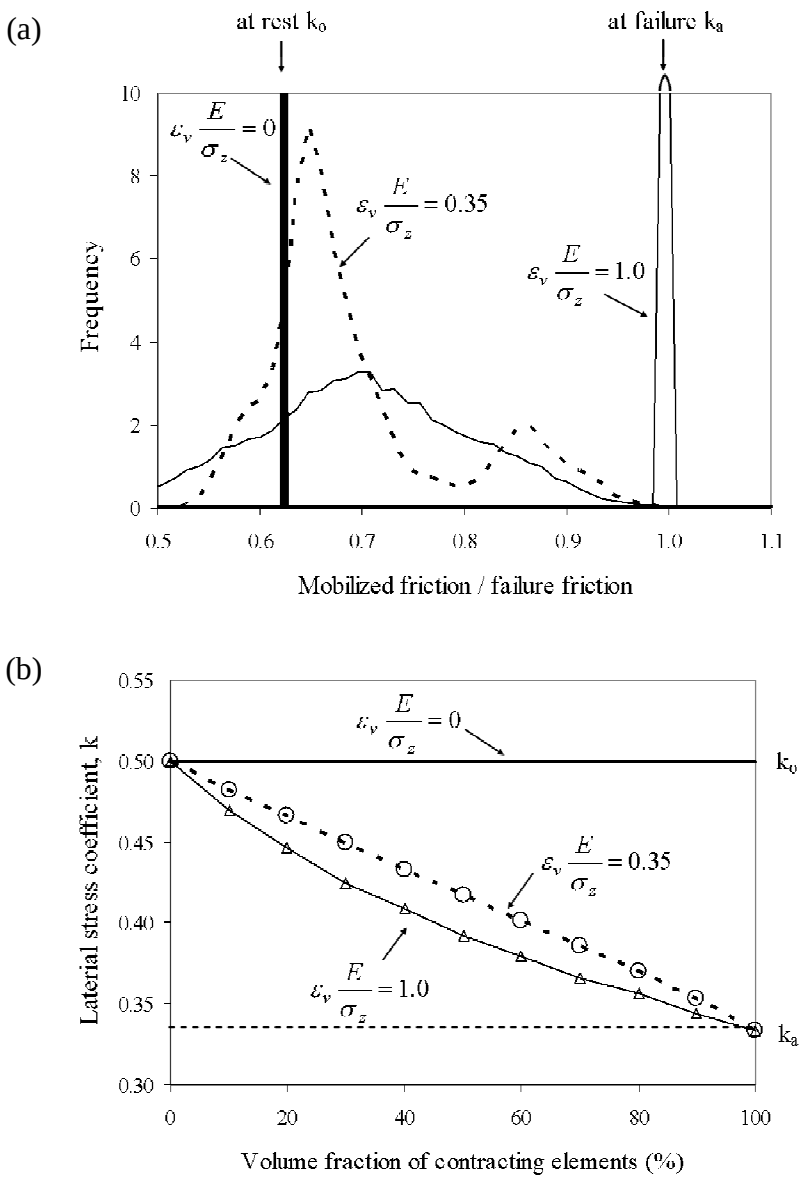

Figure 3.1 Numerical finite element simulation of volume contraction in a frictional material (ϕ=30°). Without particle contraction, the modeled material exhibits a horizontal stress coefficients equal to K_0 = 0.5 for zero lateral strain, and K_a = 0.33 for the active failure condition. (a) Histogram of local stress ratio at each element when volumetric contraction ε_v = 0.1% is imposed on 20% of the elements under constant vertical stress and zero lateral strain. (b) Value of K measured at boundaries as a function of percentage of contracting elements and amount of volume contraction.

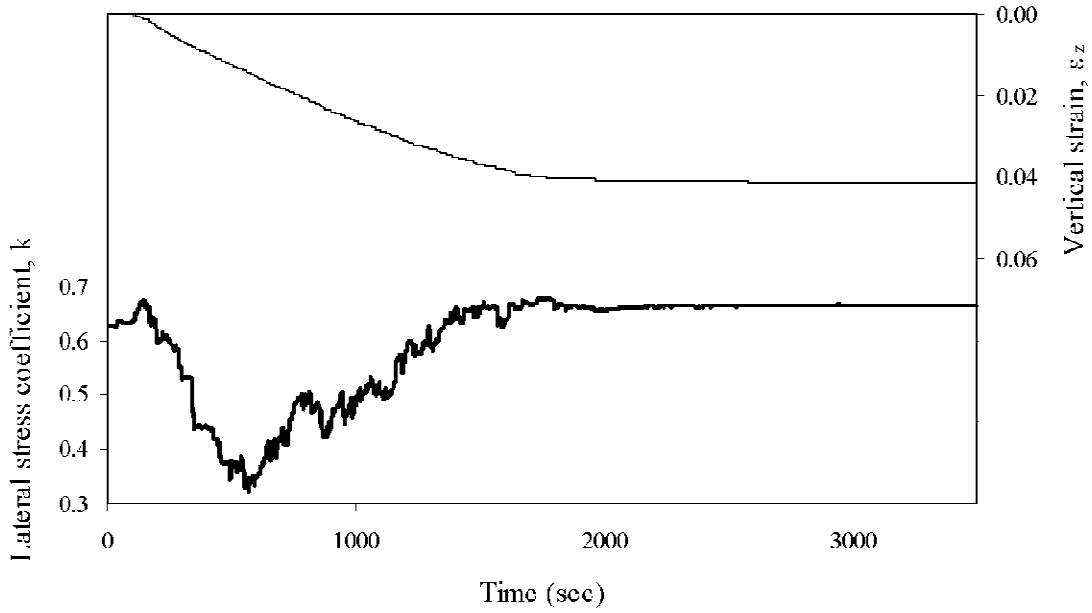

Figure 3.2 Experimentally determined evolution in lateral stress during grain dissolution. Study conducted using an instrumented, zero lateral strain oedometer cell. Results shown for a mixture of 90% unsoluble glass beads and 10% soluble granular NaCl salt (refer to Figure 2.2c).

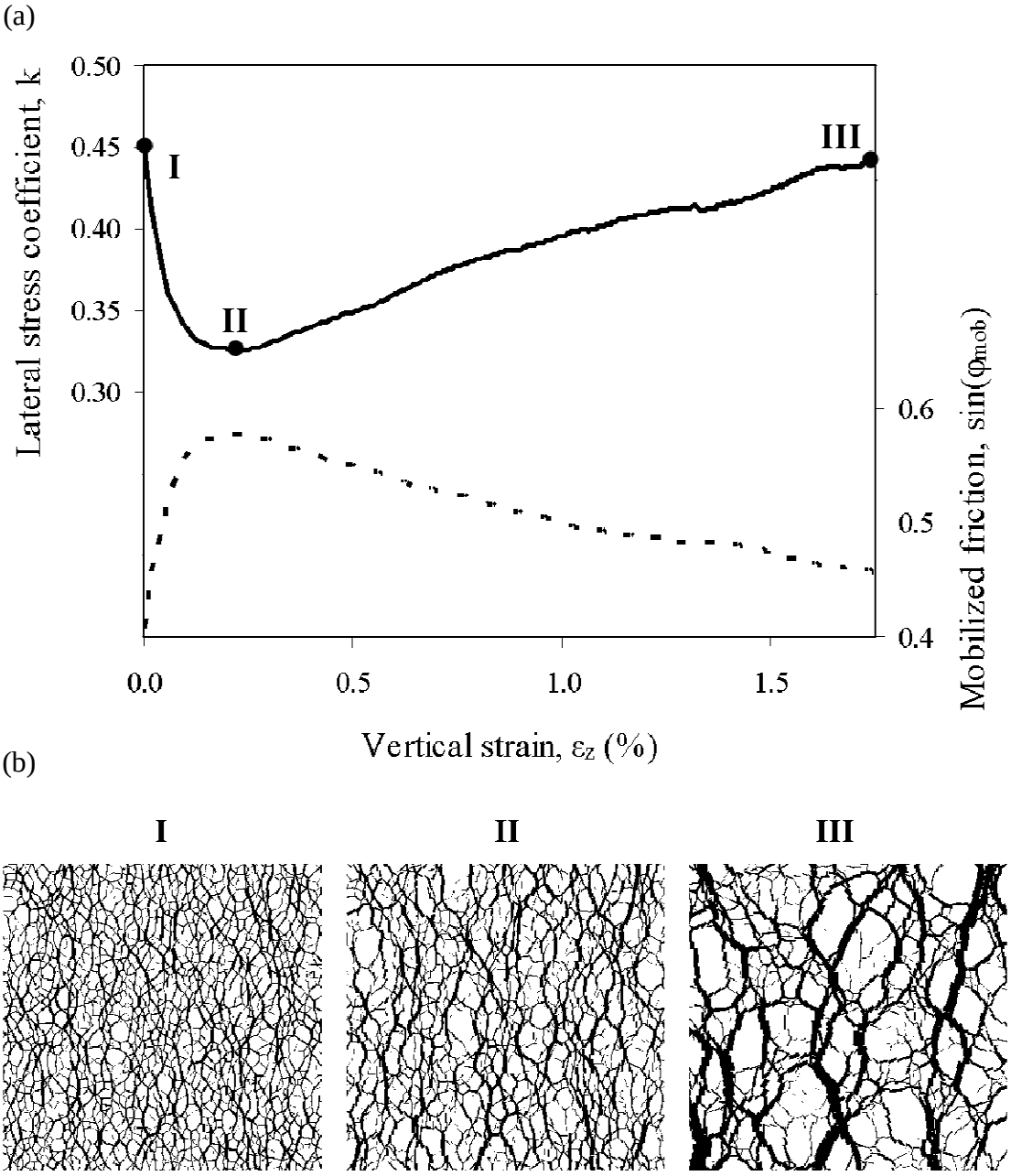

Figure 3.3 Evolution in the horizontal stress during particle dissolution. Discrete element simulation of a 2D packing of 9999 disks. The diameter of 20% of the particles - selected at random- is gradually reduced while keeping zero lateral strain and constant vertical stress boundary conditions. (a) Lateral stress coefficient K and mobilized friction (refer to Figure 2.6), (b) Interparticle force networks at different stages of dissolution (more information in Figure 2.7).

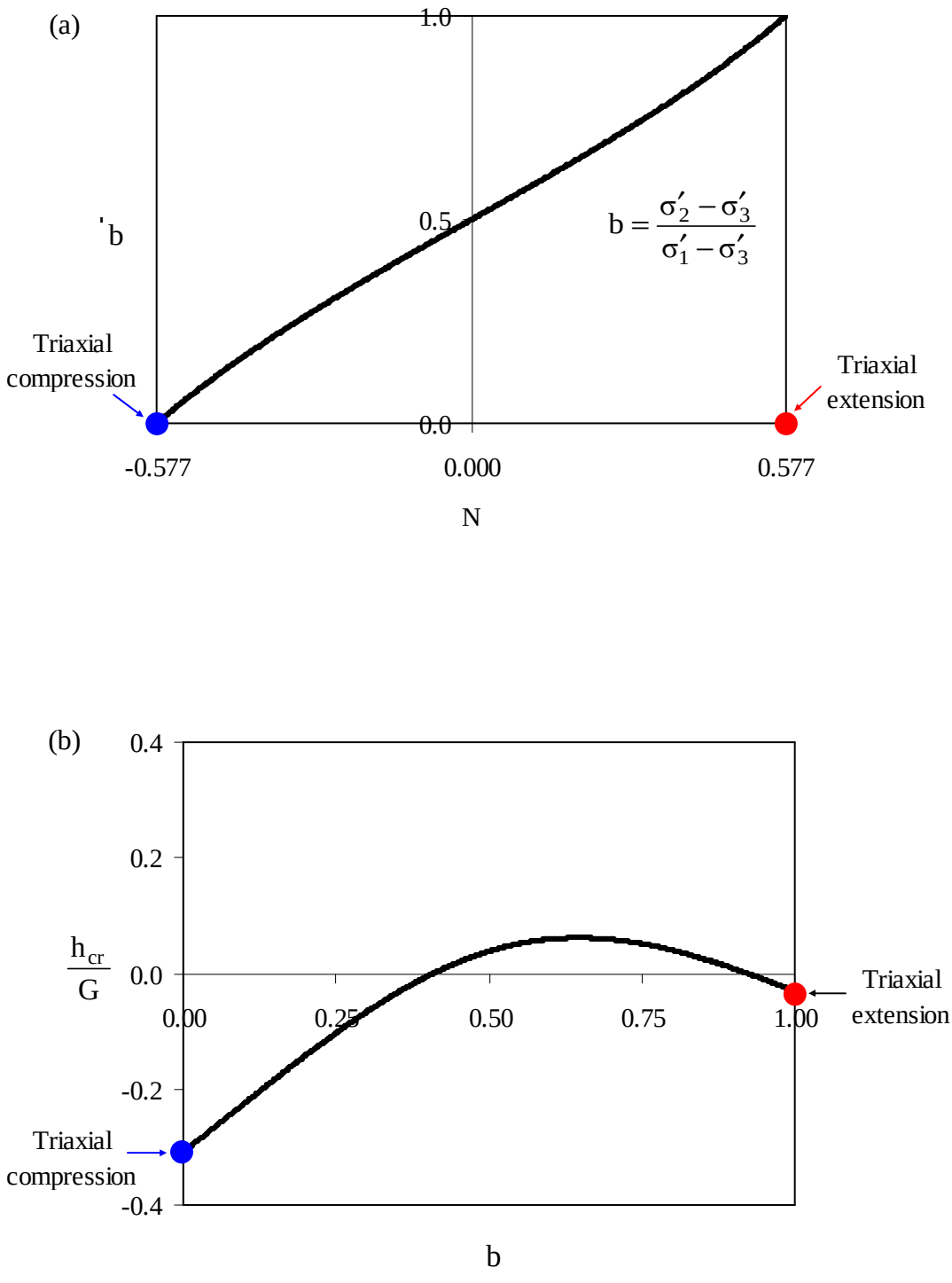

Figure 3.4 Normalized critical hardening modulus with b value. (a) Relationship between two stress parameters b and N, (b) Negative critical hardening modulus under triaxial compression condition.

(a)

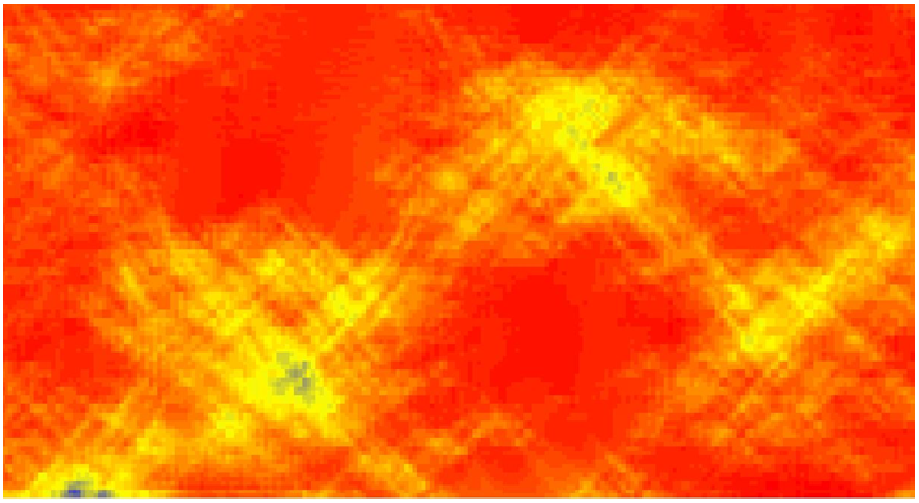

(b)

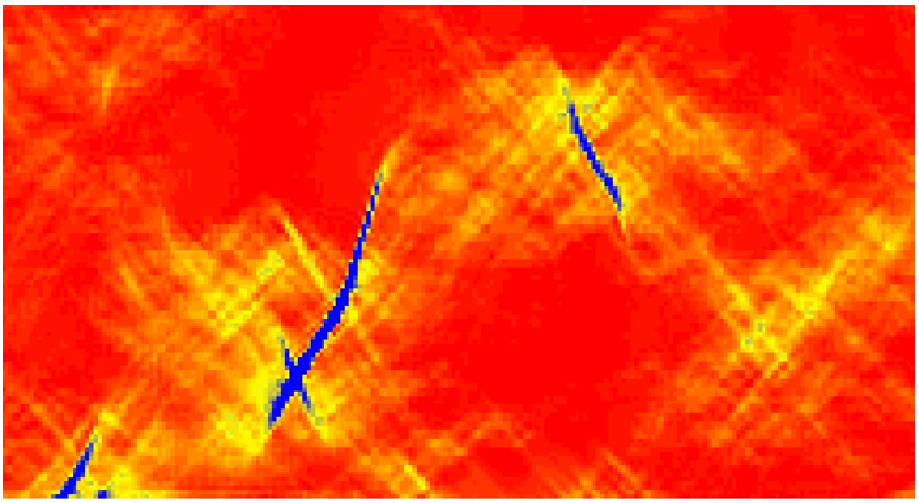

Figure 3.5 Finite element simulation - Correlated random field of volume contraction within a frictional material. (a) Diffused deviatoric strain distribution in perfectly plastic media – without softening $\phi_{residual} = \phi_{peak} = 30°$ (b) Shear strain localization is facilitated in media with post peak strain softening ($\phi_{peak} = 30°$, $\phi_{residual} = 10°$).

Appendix 3.1 Volumetric contraction to reach failure state

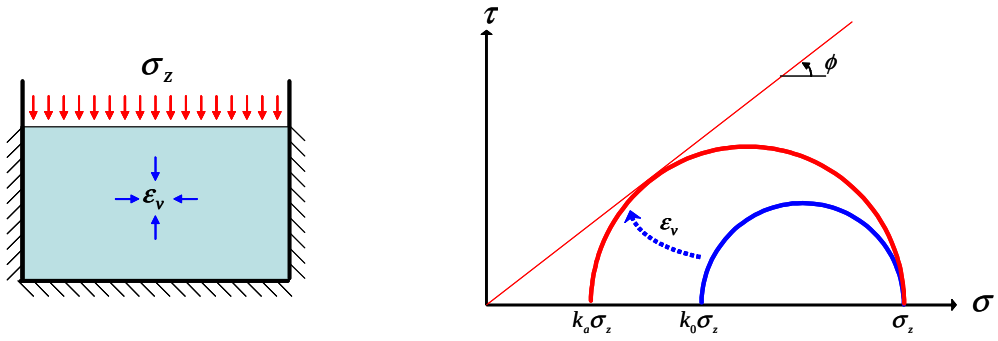

Isotropic volumetric contraction for stress change from K_0 to K_a can be calculated the following equation for linear elastic-perfect plastic material.

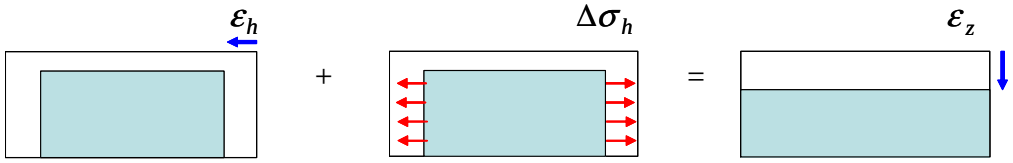

In a linear elastic material, horizontal strain from volumetric strain can be calculated as follows.

$$\varepsilon_h = \varepsilon_v/3$$

To simulate zero-lateral deformation condition, additional horizontal stress can be calculated from linear elasticity.

$$-\varepsilon_h = (1-\nu)\Delta\sigma_h/E$$

So, horizontal stress change from volumetric strain can be calculated as follows.

$$\Delta\sigma_h = -\frac{E\,\varepsilon_v}{3(1-\nu)}$$

In a soil following Mohr-Coulomb failure criterion, volumetric strain to reach active failure state from at rest stress state can be written.

$$\Delta\sigma_h = K_a\,\sigma'_z - K_0\,\sigma'_z$$

and

$$\varepsilon_v = 3(1-\nu)(K_0 - K_a)\frac{\sigma'_z}{E}$$

CHAPTER 4

DESICCATION CRACKS IN SATURATED FINE-GRAINED SOILS

4.1 Introduction

The development of desiccation cracks damages geotechnical structures, exacerbates geo-environmental problems (e.g., fast flow path for contaminants), triggers instabilities and hinders the serviceability of earth structures. Desiccation cracks are important in other fields as well, from concrete technology (Lura et al., 2007) to thin film formation and gels (Brinker & Scherer, 1990; Holmes et al., 2006).

It is often assumed that soils crack when the tensile stress that develops within the soil mass exceeds the soil tensile strength, typically in the context of non-uniform drying or boundary restrained free shrinkage. However, this mechanistic interpretation fails to recognize the inherent, cohesionless-yet-frictional effective stress dependent behavior of soils. Furthermore, assumptions such as zero effective stress at the crack tip may not necessarily reflect the underlying particle level mechanisms.

The purpose of this study is to develop a fundamental understanding of crack initiation and propagation in granular materials by combining particle-level and macro-scale perspectives. At the particle-level, we focus on the tensile membrane at the water-air interface as it invades the soil driven by the increase in suction that accompanies water evaporation. At the macroscale, we explore changes in effective stress and volume near imperfections and crack tips. Together, these two perspectives provide a new understanding of desiccation crack formation in soils. The research methodology is described next; relevant references and previous studies are cited in each section.

4.2 Research methodology

The study of desiccation crack initiation and propagation is herein implemented using a combination of experimental and numerical methods.

The full scope of the experimental study involved 273 tests for different sediments, thickness, pore fluid chemistry, and evaporation boundary condition. All results are adequately explained within the conceptual framework discussed herein; for clarity and conciseness, the manuscript follows the series of desiccation experiments that involved slurries prepared by mixing Ca-montmorillonite (Panther Creek 150; liquid limit=97%; plastic limit=47%) and deionized water (initial water content: 150%). Desiccation tests are conducted within a chamber with controlled temperature (T=25ºC) and moisture conditions (RH= 35%).

Two specimens are tested for each condition. One sits under an optical microscope (LEICA MZ6) augmented with a digital camera (Qimaging) to obtain a 0.8 to 5 μm/pixel resolution. In this case, images are gathered every 10 sec. This test configuration is designed to obtain detailed information on crack initiation and propagation mechanisms. The second specimen sits on a scale (Pinnacle 6001 with 1 mg resolution) and its surface is photographed using a digital camera operating in time-lapse mode (Nikon Coolpix P4; 3264×2448 pixels; resolution 0.013mm/pixel; photograph every 1 min). This test configuration provides the evolution of moisture, vertical and horizontal surface deformations, crack propagation, and the development of crack patterns (Matlab code modified from UraPIV; image processing details are discussed later in the text).

Analogous numerical simulations are run to gain additional information not attainable through experimentation. In these simulations, we represent the soil mass using the modified Cam clay model, within an effective stress analysis. Zero soil cohesion is assumed in all cases. Constitutive model parameters and numerical simulation details including boundary conditions are summarized in Table 4.1.

This research has attempted to provide fundamental understanding for development of discontinuities in granular materials, including evolution of K_0 during grain dissolution, shear failure as consequence of grain dissolution, displacement fields in polygonal fault systems, desiccation cracks in saturated fine-grained

4. 3 Stages in desiccation crack formation - Studies

Published desiccation crack initiation theories in soils and gels are summarized in Table 4.2. Presently, these theories are either incomplete or cannot be justified from the fundamental behavior of uncemented granular materials. In this section, we seek a physically acceptable and complete mechanism, and explore the different stages in desiccation crack formation using experimental and numerical tools described above. We start with water evaporation from slurries.

4.3.1 Water evaporation and surface settlement before crack initiation

At the beginning, the supernatant water evaporates at an approximately constant rate. The effective stress in the soil is constant, and the soil experiences no strain.

Once the air-water interface reaches the soil surface, both continue moving downwards together. The soil skeleton consolidates due to the increase in effective stress that equals the increase in suction u_c. The current void ratio e is related to u_c as prescribed in the 1D normal consolidation line NCL: $e=e_{atm}- C_C \cdot \log(u_c/atm)$.

Let's explore this early stage of desiccation experimentally. A single layer of fully saturated Ca-montmorillonite slurry (initial water content: 150%; 1.9 mm thick) is placed in a plastic container (diameter=87mm; wall height=12mm). The vertical and horizontal displacements of a point on the soil surface can be computed from optical images in reference to an external fixed point taken as the image focus. Consider only those cracks that propagate towards the reference point; for a given pixel: (1) the radial movement

towards the image focus is used to compute the vertical displacement -Pythagorean analysis, and (2) the horizontal displacement normal to the direction of crack propagation is determined from the tangential component of the pixel displacement. The evolution of the slurry water content and soil surface displacements are shown in Figure 4.1. The quasi-constant rate of evaporation stage coincides with continuous vertical settlement, (i.e., the soil remains saturated – see also Bronswijk, 1988), and there is no lateral displacement.

The evolution of soil suction during drying is measured using the filter paper method (Bulut et al., 2001). Slurry is poured into thirty containers and left to dry. At selected times, specimens are sealed with a wet filter paper inside the container for 5 days. Then, the soil metric suction is determined from the water content in the filter paper using the drying filter paper calibration curve in Bulut et al. (2001). Data, superimposed on Figure 4.1, show that the constant rate of evaporation coincides with low levels of suction.

The increase in effective stress causes the increase in skeleton stiffness as well. From critical state, the one dimensional constrained modulus D can be related to suction u_c as

$$D = \frac{(1+e_0)\,u_c}{\lambda} \qquad \textit{before air entry} \qquad (4.1)$$

where e_0 is the initial void ratio, and λ is compression index ($\lambda=0.434C_C$). Therefore, low suction during early stages of evaporation implies low skeletal stiffness. Eventually, further evaporation and increased suction will force the air-water interface membrane to invade the soil mass. This situation is analyzed next.

4.3.2 Crack initiation

Cracks initiate during the constant rate of evaporation stage in all tests conducted as part of this study (such as in Figure 4.1). The soil is still fully saturated at crack initiation, i.e., the air-water interface and the apparent soil surface coincide (in agreement

with observations based on gels by Brinker & Scherer 1990). The soil surface experiences no horizontal displacement before crack initiation, and limited vertical movement thereafter (Figure 4.1).

The relevance of surface defects. In particular, all our experimental results with homogenous fine-grained slurries show that crack initiation takes place at surface defects, such as sub-millimeter size "craters", and propagate both laterally and downward (Figure 4.2 – see also Allen, 1982). Inclusions, large aggregate anomalies or small topographic features (e.g. indentations) can trigger crack formation due to shrinkage distortion of the surrounding medium (see also Towner, 1988; Weinberger, 1999; Zabat et al., 1997).

Void ratio at the tip and in the far field. Furthermore, we notice in all our experiments that cracks always start at the bottom of the defect, not at the equator (Figure 4.2 – Contrary to Scherer 1990). A numerical simulation is conducted to investigate the underlying effective stress mechanisms. A Gaussian-shaped surface defect is considered in a modified cam clay material, and modeled using an axisymmetric mesh (model parameters, mesh details and boundary conditions are summarized in Table 4.1a). Internal suction is applied throughout the whole medium, starting at an equilibrium condition p'=0.01 kPa with homogeneous void ratio e=3.92, and gradually increasing the suction to reach p'=100 kPa with far field void ratio e=2.105. The simulation is repeated for various slenderness ratios. Figure 4.3a shows the void ratio distribution around the defect. Consolidation takes place everywhere, however, a higher void ratio is reached at the tip of defects than anywhere else, particularly in narrow defects: the e-σ´ path at the tip gradually deviates from the e-σ´ path in the far field, which follows the normal consolidation line NCL (Figure 4.4).

Air entry line e-u_c (AEL). A lower air-entry suction u_c^{AE} [kPa] corresponds to a higher local void ratio e. This can be estimated assuming parallel platy particles of thickness t

separated at a distance d (Figure 4.3b): the void ratio is e=d/t, and the specific surface is $S_s=2/(\rho t)$. Then, the air entry suction $u_c^{AE}=2T_s/d$ (Laplace equation) is:

$$u_c^{AE} = \frac{\rho T_s S_s}{e} \tag{4.2}$$

where ρ [g/cm^3] is the mass density of the particle and T_s = 0.072 N/m is surface tension of water. A similar analysis for the packing of spherical particles with radius R leads to:

$$u_c^{AE} = \frac{2T_s/R}{\sqrt[3]{\frac{2}{3}\pi(1+e)}-1} \tag{4.3}$$

The change in air entry suction u_c^{AE} with void ratio e defines the air entry line AEL in the void-stress space.

Crack initiation at air invasion. The void ratio at the tip reaches the air entry line AEL first, and air invades the soil mass at the tip while the rest of the soil remains saturated (Figure 4.4). This is the moment when the crack initiates (see also Childs 1969). This sequence of events is in agreement with all our experimental observations that place crack initiation at the tip of defects in soft sediments.

Fine vs Coarse grained soils. Soft, high specific surface soils (typically made of platy particles) have small pores so that the AEL intersects the NCL at high suction (Figure 4.4). Air invasion causes large particle displacements and crack opening because of the low soil stiffness (see Prodanovic & Bryant 2006, and Jain & Juanes 2008 for particle forces induced by interfacial tension). On the other hand, coarse low specific surface soils have large pores, low air entry values, steep AEL, and high skeletal stiffness (flat NCL). Therefore, there are almost no differences in air entry at tips or anywhere else, and the interfacial water-air membrane massively invades the soil.

Summary. The increased local void ratio at the tip of defects facilitates air-water membrane invasion into the soil mass as suction increases in a drying soil. Air invasion is the starting point for desiccation crack formation in saturated soft soils.

4.3.3 Crack propagation

Analogous to crack initiation, we anticipate that the void ratio increases and the air-entry value decreases at the crack tip, the air-water membrane preferentially invades the soil at the tip and the crack propagates.

We test this growth mechanism by modeling a homogeneous single-layer slab of soil, subjected to homogeneous suction u_c= 100kPa in equilibrium at a void ratio e =2.087 (Simulation details in Table 4.1b). After equilibrium, a node in the middle of the left boundary is released to emulate crack initiation while suction is kept constant. The soil mass is allowed to regain equilibrium under constant suction. Then a new node is released where the void ratio is highest. The process is repeated to reproduce crack growth. (Note: The fluid pressure homogenization is not instantaneously reached throughout the medium as crack propagation takes place; however a short time is expected for pressure diffusion given the short length scale involved at the tip).

Instantaneous stress-volume data are shown in Figure 4.5. The crack propagates along the centerline. There is a marked drop in effective horizontal stress immediately ahead of the crack tip; then, the horizontal effective stress recovers to the applied suction after the crack passes. The void ratio at the crack tip is higher than anywhere else. The soil next to the crack walls behind the tip reconsolidates and the void ratio decreases due to the compression imposed by capillary suction against the crack walls (Figure 4.5b & 4.5c).

The numerical simulation approach is validated by comparing numerical predictions against experimental observations. Displacements transverse δ_y and parallel δ_x to the propagation direction x are determined using digital image correlation between consecutive microphotographs, when the crack is at beginning position “B” and at the end position “E”. Nodal displacements are readily obtained from the corresponding stages in the numerical simulation. A strong resemblance is observed between experimental and numerical results (Figure 4.6). There is a quasi-circular shape of the

transverse displacement δ_y bulb which expands behind the crack tip as the crack opens during suction driven consolidation; the affected region scales with the propagation distance. No transverse movement is observed ahead of the crack, except in the far field. The displacement parallel to the direction of crack propagation δ_x is towards the tip, both behind and ahead of the crack tip.

Results in Figure 4.5 (and 4.6) confirm that the soil dilates ahead of the tip, the air entry suction decreases at the tip, and the soil becomes reconsolidated as the crack advances further. It is important to highlight that membrane invasion and crack propagation take place while the effective stress state is in compression everywhere in the medium including at the crack tip. (Note: Holmes et al., 2006 makes a similar observation in a study with alumina suspensions.)

4.4. Stages in desiccation crack formation - Summary

On the bases of previous experimental observations and numerical results, we can identify the following stages in desiccation crack initiation and growth in saturated fine grained soils (Figure 4.7).

Water surface above the sediment surface. In this stage, the water evaporates freely, the pore fluid pressure is positive everywhere inside the sediment, and there is no capillary suction (Figure 4.7a). Eventually, the water level reaches the sediment surface (Figure 4.7b); at this instant, the pore fluid pressure on the surface is zero.

Mobilization of tensile membrane and development of suction. Further evaporation brings the air-water interface membrane against grain surfaces and other topographic features (Figure 4.7c). The membrane grabs onto soil particles and resists invading the soil. Capillary suction develops in the pore fluid (Laplace's equation), and effective stress in the granular skeleton. The soil consolidates, the skeletal stiffness gradually increases, and

the magnitude of the vertical one dimensional settlement is equal to the amount of water that evaporates. The soil remains saturated throughout this stage.

Membrane invasion - Crack Initiation. The increased stiffness of the soil skeleton hinders further consolidation. If evaporation continues, capillary suction causes the air-water interface to invade the sediment. Air intrusion starts at the largest pores, often associated with surface defects. Membrane invasion causes particle displacement into the soil mass, normal to and away from the air-water interface. Therefore, membrane invasion takes place at surface features following the order prescribed by pore size and particle mobility. The pore size increases at the tip of the invading front so that further membrane invasion is favored at the tip signaling crack initiation (Figure 4.7d). Crack initiation can be expected during the constant rate of evaporation regime (Figure 4.7 – see also Figure 4.1). Vapor transport away from the soil surface becomes increasingly more difficult as the air-water interface is pulled into the soil. Then, the evaporation rate decreases almost linearly as the total suction increases (Figure 4.1 - Brinker & Scherer 1990 – see also Wilson et al. 1997 but in linear-linear scale).

Crack propagation. Crack growth consists of membrane invasion into the enlarged pores at crack tips, where the void ratio increases and the air-entry value decreases. Once the air-water interface membrane invades ahead of the crack tip, a new surface is formed and the process repeats itself. Particle mobility and changes in void ratio decrease with depth, so that preferential membrane invasion takes place into lateral pores, and cracks propagate along the surface. Once again, we highlight that the soil mass experiences compressive effective stress everywhere and at all times during the desiccation-crack process.

Eventually, the soil mass between cracks becomes unsaturated. The long-term equilibrium capillary suction reflects the relative humidity, and water content is the retention capacity of the soil as determined by its specific surface and the prevailing relative humidity.

4.5. Further analyses - Discussion

The proposed sequence of events for desiccation crack initiation and growth in saturated fine-grained soils is inherently compatible with the frictional, effective stress dependent behavior of soils. In this section, we invoke the hypothesized mechanism to explain other observations related to desiccation crack formation in soils.

4.5.1 Desiccation cracks, pore size distribution, and soil fabric

It follows from the previous discussion that membrane invasion and crack initiation will more readily take place in soils with non-uniform pore size distribution than in soils of similar porosity but with a uniform pore size distribution. Furthermore, some sediments with initial mono-model pore size distribution may develop a bimodal distribution as suction increases (Koliji et al., 2006). Assuming log-normal distribution of pore size distribution, the ratio between standard deviation $\sigma*$ and mean $\bar{d}$, $\log(\sigma*/\bar{d})$ is typically between 0.3 and 0.7. Air will invade the largest pores first, and the air entry line will plot at lower levels of suction than those predicted by Equations 4.2 or 4.3.

Pore size distribution, fabric, and stiffness in fine grained minerals are determined by the pore fluid ionic concentration, permittivity and pH (Palomino and Santamarina, 2005; Zabat et al., 1997). In particular, fine grained soils mixed with a high concentration salt solution form aggregated fabrics and exhibit larger pore diameters than dispersed fabrics at the same confining stress (Wang and Xu, 2007). Therefore we anticipate that the pore fluid chemistry will affect desiccation crack formation. Indeed, slurries containing aggregations developed a more extensive fracture network than slurries made of dispersed grains (van Damme and Ben Ohoud, 1990; Zabat et al., 1997).

We explicitly confirmed the role of ionic concentration on fabric formation on desiccation cracks by conducting desiccation tests with two Na-Bentonite slurries prepared at the same initial water content of 1000%, one mixed with deionized water and the other with 0.1M NaCl. Results presented in Figure 4.8 corroborate that the soil mass tends to remain monolithic for low ionic concentration pore fluids (dispersed fabric with small and uniform pore size). On the other hand, the soil with high ionic concentration pore fluid becomes extensively fractured as the air-water membrane readily invades the multiple large surface pores between aggregations.

4.5.2 Crack propagation near preexisting cracks – Crack pattern formation

Propagating contraction cracks in cohesive media turn towards existing cracks until they finally intersect at right angles (Morris et al., 1992). Typically, this observation is explained by the maximum stress release criterion (Lachenbruch, 1962): since the internal stress normal to the existing crack plane has been released already, the propagating contraction crack will approach the preexisting crack normal to it.

Furthermore, predictions based on linear elastic fracture mechanics in cohesive media show that as the crack tip approaches the free boundary, the stress intensity experiences a pronounced increase (Figure 4.9), and the crack propagation velocity increases (experimental data for cohesive media in Dally et al. 1985).

We measured multiple cases of desiccation crack tip propagation approaching earlier cracks in soils, and confirmed the well known normal intersection. However, we found in all cases that the velocity of propagation decreases as the distance to the free boundary decreases (Figure 4.10). Why do desiccation cracks in soils slow down and turn towards the nearby free boundary? One explanation consistent with the proposed mechanism is that the lower velocity results from delayed water migration into the expanding soil at the crack tip in the vicinity of the “effectively impervious free boundary” at the existing crack face. Furthermore, suction acts at the free boundary, and

increases the isotropic stress at the approaching crack tip, therefore there is a lower increase in void ratio and the air-entry value remains high.

This mechanical explanation is confirmed by the simulation of crack propagation towards a skewed free boundary shown in Figure 4.11 (Model details in Table 4.1b - nodes are released only along the central alignment in this simulation). There is restricted volume dilation at the crack tip near the free boundary as can be seen by the size of the void ratio bulbs in the three frames shown in Figure 4.11. Furthermore, and contrary to results in Figure 4.6, consolidation induced displacements are much more pronounced on the right hand side of the crack, i.e., closer to the free boundary (not shown here), driving void ratio changes, air invasion and crack propagation normal to the preexisting crack.

4.5.3 Tensile strength in fine grained soils

The “apparent tensile strength” exhibited by an uncemented saturated soil specimen in air cannot be justified on the bases of interparticle electrical forces. In fact, strength must result from inter-granular friction and the confining effect of capillary suction that develops as the air-water interface resists intruding the saturated medium (a comprehensive experimental study with clay beams can be found in Thusyanthan et al. 2007; tensile tests in sandy sediments are presented in Lu et al., 2007).

The failure of a saturated soil in tension is explored using numerical simulations. The soil is modeled as a modified cam clay material and an internal suction of 100 kPa is applied first (model details in Table 4.1a). After equilibrium, the specimen is subjected to 50kPa tension. The void ratio and deviatoric stress fields are shown in Figure 4.12. While the maximum deviatoric stress ratio develops at 45 degrees from the crack tip, the void ratio expansion is aligned with the notch. Therefore, the air-water membrane will invade the specimen and the crack will grow normal to the applied tensile load eventually giving the appearance of a tensile failure while the soil mass has remained in compression at all times.

Based on the initial air entry value u_0, the upper bound for the apparent soil tensile strength can be estimated for the Mohr-Coulomb failure criterion (saturated soils),

$$\sigma_T \leq u_0 \frac{2\sin(\phi')}{1+\sin(\phi')} \qquad \textit{upper bound} \qquad (4.4)$$

We highlight that this is an upper bound because the void ratio increases and the air entry value at the tip decreases during the tensile test, thus a lower "tensile strength" will be measured (Equation 4.2).

Crack initiation in drying slurries occurs while the stress history at the tip is still normally consolidated. However, crack propagation away from the initial defect and in tensile tests in general cause effective stress unloading at the crack tip; this situation prompted Thusyanthan et al. (2007) to explore failure on the Hvorslev failure surface when the initial capillary suction is high.

Suction driven tensile strength based on the invasion of air-water membrane can be estimated using a modification of Equation 4.1. When the specimen is subjected to an initial capillary suction u_0, the initial void ratio e_0 is determined from isotropic consolidation $e_0=e_{atm}- \lambda \cdot \ln(u_0/atm)$. The application of a boundary tensile strain ε_z decreases the air-entry suction u_c^{AE} : let's assume a material made of parallel platy particles (Figure 4.13a): the initial void ratio $e_0=d_0/t$ corresponds to a separation distance d_0; after a tensile strain ε_z, the new interparticle separation becomes $d=d_0+(t+d_0)\times\varepsilon_z$, and air entry suction decreases to

$$u_c^{AE} = \frac{\rho T_s S_s}{e_0(1+\varepsilon_z)+\varepsilon_z} \qquad (4.5)$$

The specimen follows an unloading stress path, and the stress-strain stiffness can be estimated from the swelling index κ in isotropic unloading so that $\varepsilon_z=E_t/\sigma_z$, where $E_t=(1+e_0)/\kappa\times u_0$ for a Poisson's ratio $\nu=1/3$.

The evolution of the air-entry suction u_c^{AE} with the applied tensile stress σ_z is shown in Figure 4.13a. When the tensile load reaches the air entry suction (Equation 4.5),

air invasion occurs to form an opening crack into the saturated medium. A non-uniform pore size distribution leads to a lower air entry line, a decreased apparent tensile strength and a lower tensile strain at failure (Figure 4.13a). The apparent tensile strength of saturated fine grained soils increases with initial capillary suction towards an asymptotic value ($\rho T_S S_S / e_0$); on the other hand the tensile strain at failure decreases with the increase in initial capillary suction (Figure 4.13b).

4.5.4 Related observations - Limitations

Saturation. The degree of saturation is extensively used in unsaturated soil mechanics (Fredlund & Rahardjo, 1995; Rodriquez et al., 2007). However, this is a large-scale parameter and its utilization requires careful interpretation in the context of desiccation cracks in fine grained soils where soil blocks between cracks are expected to remain fully saturated long after crack formation as can be inferred from Figure 4.4 for the case of high specific surface soils.

In coarse grained soils, the air-entry value is low, the skeletal stiffness is high, and the air-water interfacial membrane readily invades the soil mass at relatively low suction (Figure 4.4). Hence, the proposed mechanism for desiccation crack formation based on air invasion looses validity in coarse grained soils. Still, menisci at inter-particle contacts pull particles together (Chertkov et al., 2004; Cho & Santamarina, 2001; Peng & Horn, 2007), and can cause contractive strains that lead to large scale desiccation fractures such as giant desiccation cracks (see examples in Harris 2004). A phenomenological explanation of desiccation cracks in such coarse grained materials is still pending.

4.6. Conclusions

The total stress tensile strength criterion for desiccation crack formation hides the inherent cohesionless, effective stress dependent frictional strength of uncemented soils.

The fundamental mechanism for desiccation crack initiation and growth is centered on the air-water interface membrane. Initially the air-water interface membrane resists invading pores, capillary suction increases, the effective stress increases, the soil consolidates, and the skeletal stiffness increases. Eventually, the air-water interface membrane invades the largest pores and causes particle displacement away from the invasion point. The void ratio increases at the tip and facilitates further membrane invasion and crack growth.

This sequence of events explains known observations related to desiccation crack formation in soils, including: pore fluid and fabric effects on the desiccation crack pattern (due to pore size distribution and air entry); slower crack propagation velocity as the crack approaches the free boundary of a pre-existing crack (due to delayed water migration and a smaller reduction in air-entry value next to the free boundary); right angle junction in crack pattern formation (caused by the rotation of the void ratio expansion contours towards the pre-existing free boundary); and frictional resistance in axial extension yet with a normal failure surface (due to the increase in void ratio and membrane invasion normal to the applied extension).

In all cases, membrane invasion and desiccation crack propagation take place while the state of effective stress remains in compression everywhere in the soil mass, including at the crack tip.

Table 4.1 Numerical study: Model, material parameters

<table>
<tr><td colspan="2">Element type and boundary conditions</td></tr>
<tr><td>(a) Study reported in Fig. 4.3 and 4.12
▪ Element type: 8 node, axi-symmetric or plane strain
▪ No friction against boundaries
 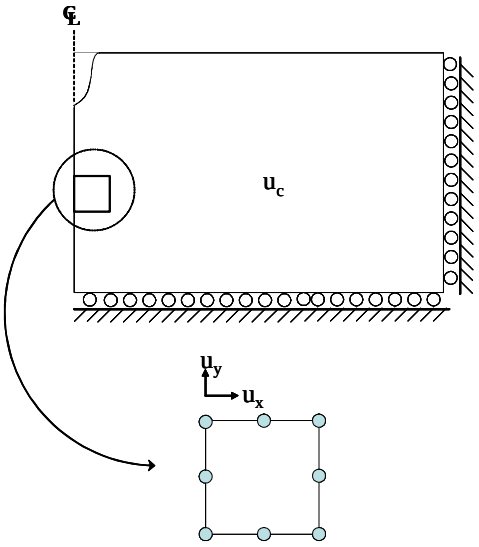
</td><td>(b) Study reported in Fig. 4.5, 4.6, and 4.11
▪ Element type: 20 node, 3D element
▪ No friction against boundaries
 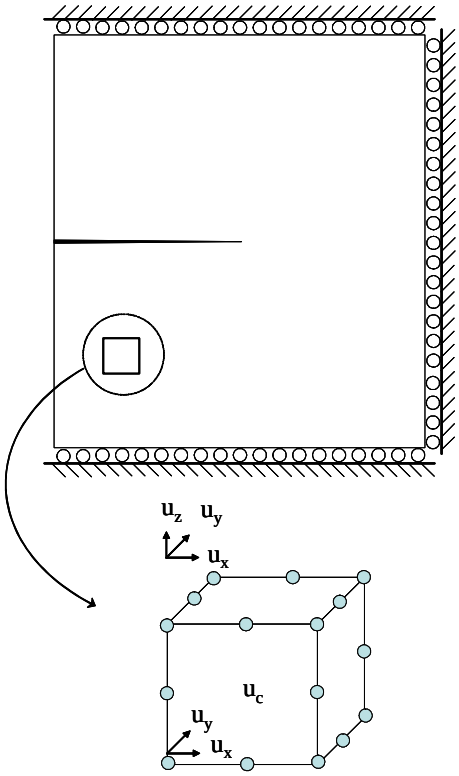
</td></tr>
<tr><td colspan="2">Material properties

▪ Constitutive model: Modified Cam clay model with associated flow rule
▪ Soil properties: normally consolidated , compression index C_c=0.46, swelling index C_s=0.15, void ratio at 1 kPa e_{1kPa}=3, failure stress ratio M=1.0, Poisson’s ratio ν=0.3
▪ Effective stress formulation with internal capillary suction u_c.</td></tr>
</table>

Table 4.2 Previous theories for crack initiation in granular materials

Theory	Mechanism (selected references)	
Tensile failure	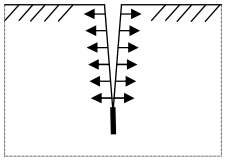	Tensile stress > material tensile strength. Most commonly assumed model (Allen, 1982; Hallett & Newson, 2005; Konrad & Ayad, 1997; Lachenbruch, 1962; Morris et al., 1992; Naser Abu-Hejleh & Znidarcic, 1995).
Irregular drying front	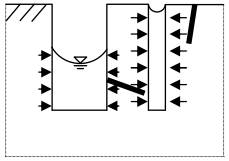	Difference in capillary pressures and subsequent failure of pore walls. Conceptual – no verification (Zarzycki et al., 1982).
Circumferential tension	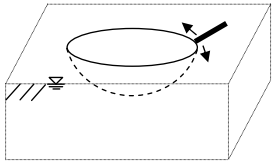	Growth of radial crack due to hoop tension. Conceptual – no verification (Scherer, 1990).
Air entry	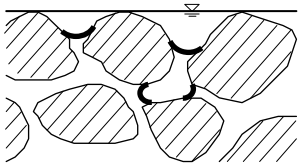	Menisci invasion due to increasing capillary tension. Conceptual – no verification (Childs, 1969; Brinker & Scherer, 1990; Herrera et al., 2007).
Packing collapse	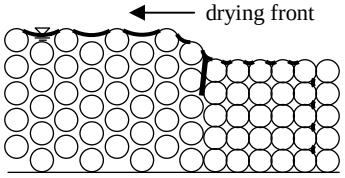	Collapse of particle layers by capillary suction. Concept used to explain desiccation cracks in a drying strip (Holmes et al., 2006).

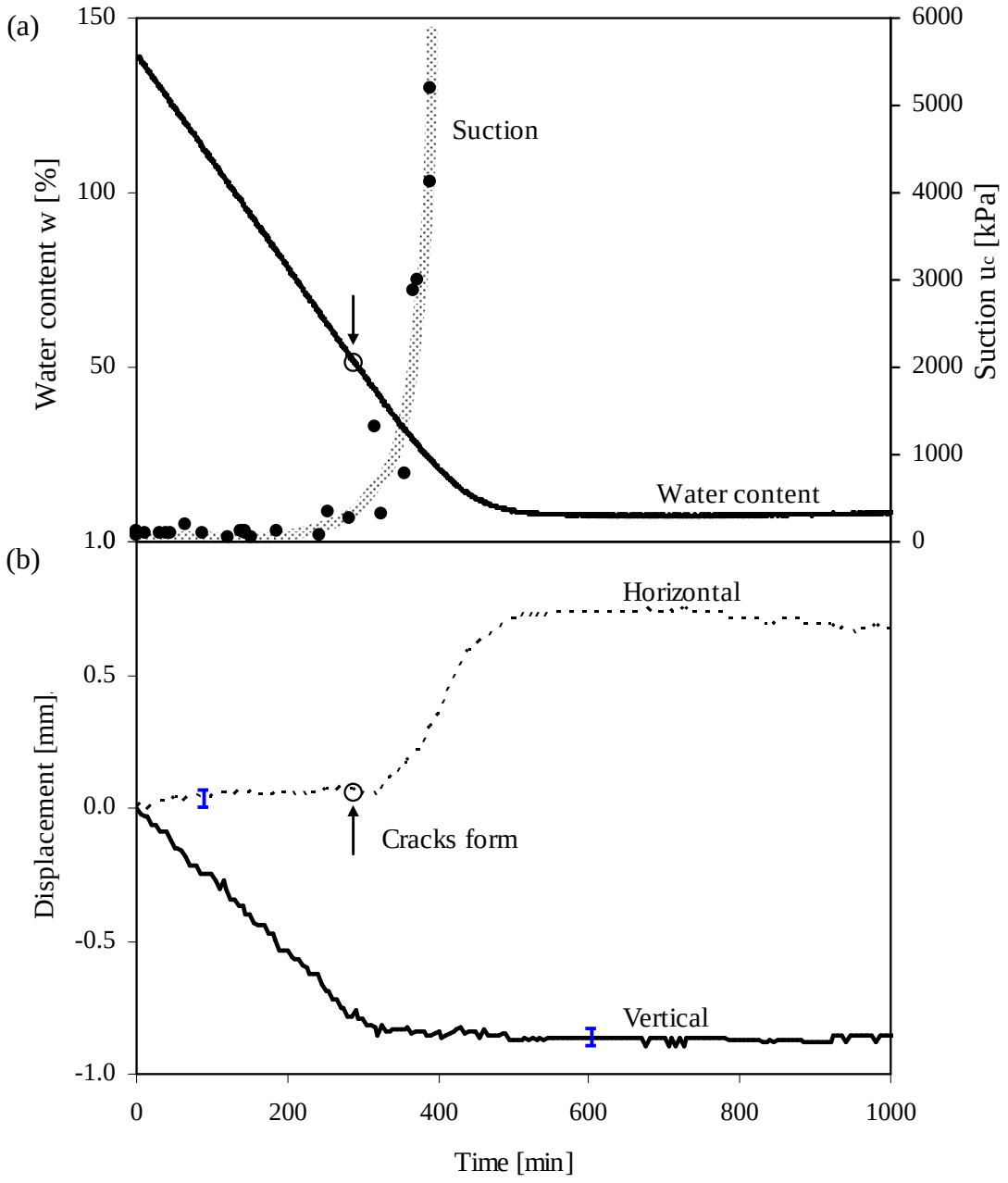

Figure 4.1 Desiccation versus time. (a) Water content and suction evolution. (b) Vertical settlement and horizontal displacement of a point on the soil surface next to a developing desiccation crack.

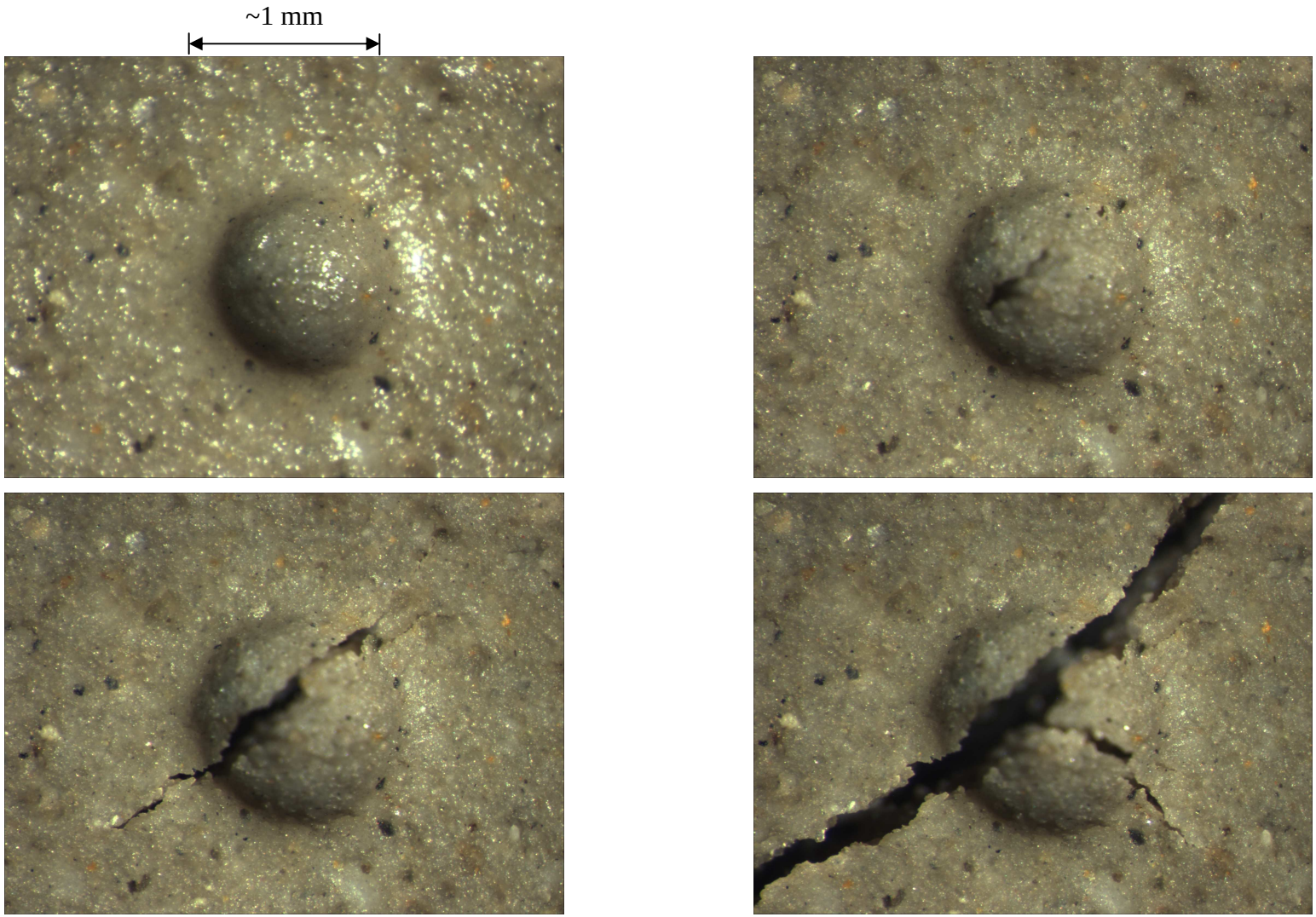

Figure 4.2 Crack initiation at the bottom of a surface defect during evaporation.

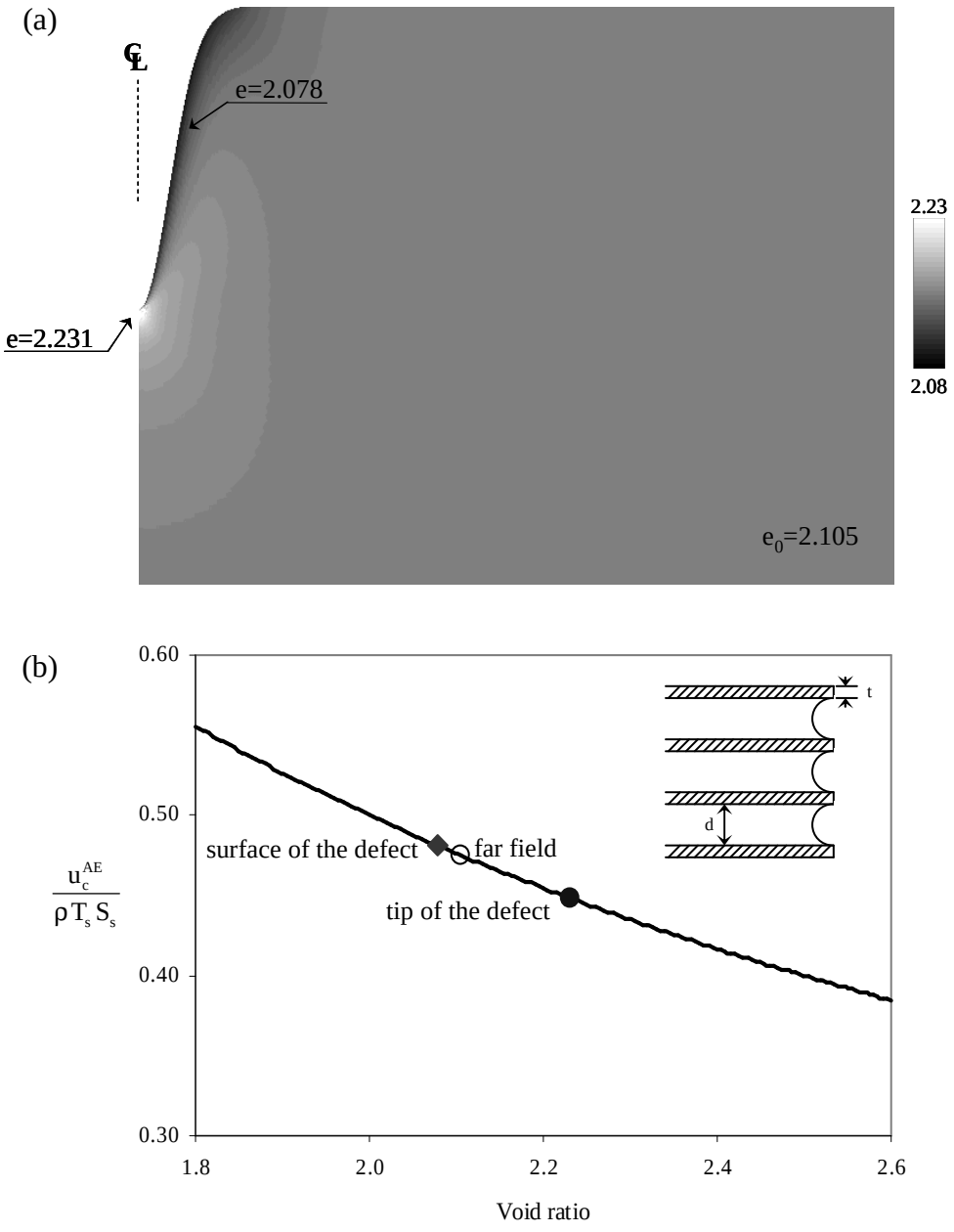

Figure 4.3 Surface defects and crack initiation. Local void ratio evolution during desiccation - Finite element analysis. The domain size is 6mm×6mm, and the defect depth is 1mm. (a) Void ratio when suction u=100kPa. Model details in Table 4.2a. (b) Required suction for air entry at the tip and on the surface as a function of the local void ratios – Equation 4.2.

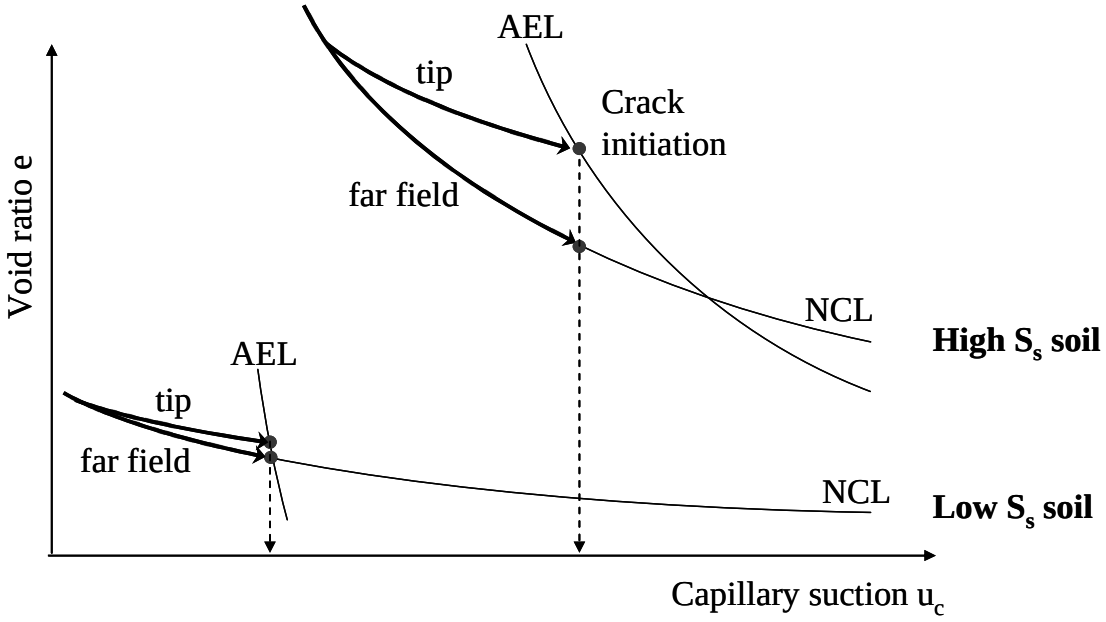

Figure 4.4 The air entry line AEL and the normal consolidation line NCL. Trends are shown for soft high specific surface soils such as NC clays and for stiff low specific surface soils such as sands. Air entry lines defined by Equations 4.2 and 4.3. Both normal consolidation lines defined as $e=e_{atm}- C_C \cdot \log(u_c/atm)$.

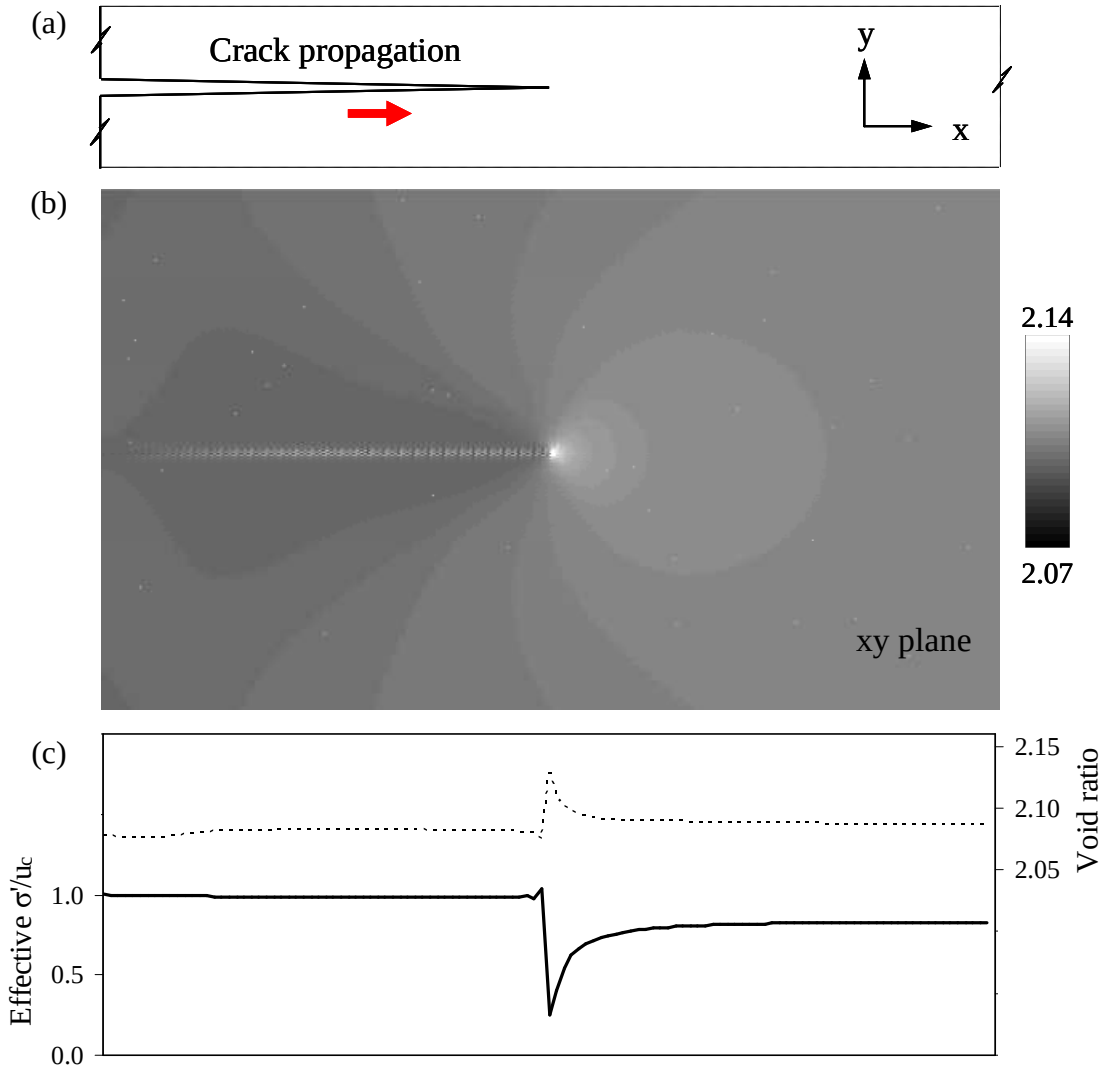

Figure 4.5 Void ratio evolution during crack propagation. (a) Geometry and crack tip location. (b) Void ratio contours - View on xy plane normal to the xz crack plane. (c) Effective stress σ_y' normal to the crack plane and void ratio along the crack alignment. Model details in Table 4.2b - Plane stress with suction u_c. The simulated domain size is 12mm long and 14mm wide (full length shown).

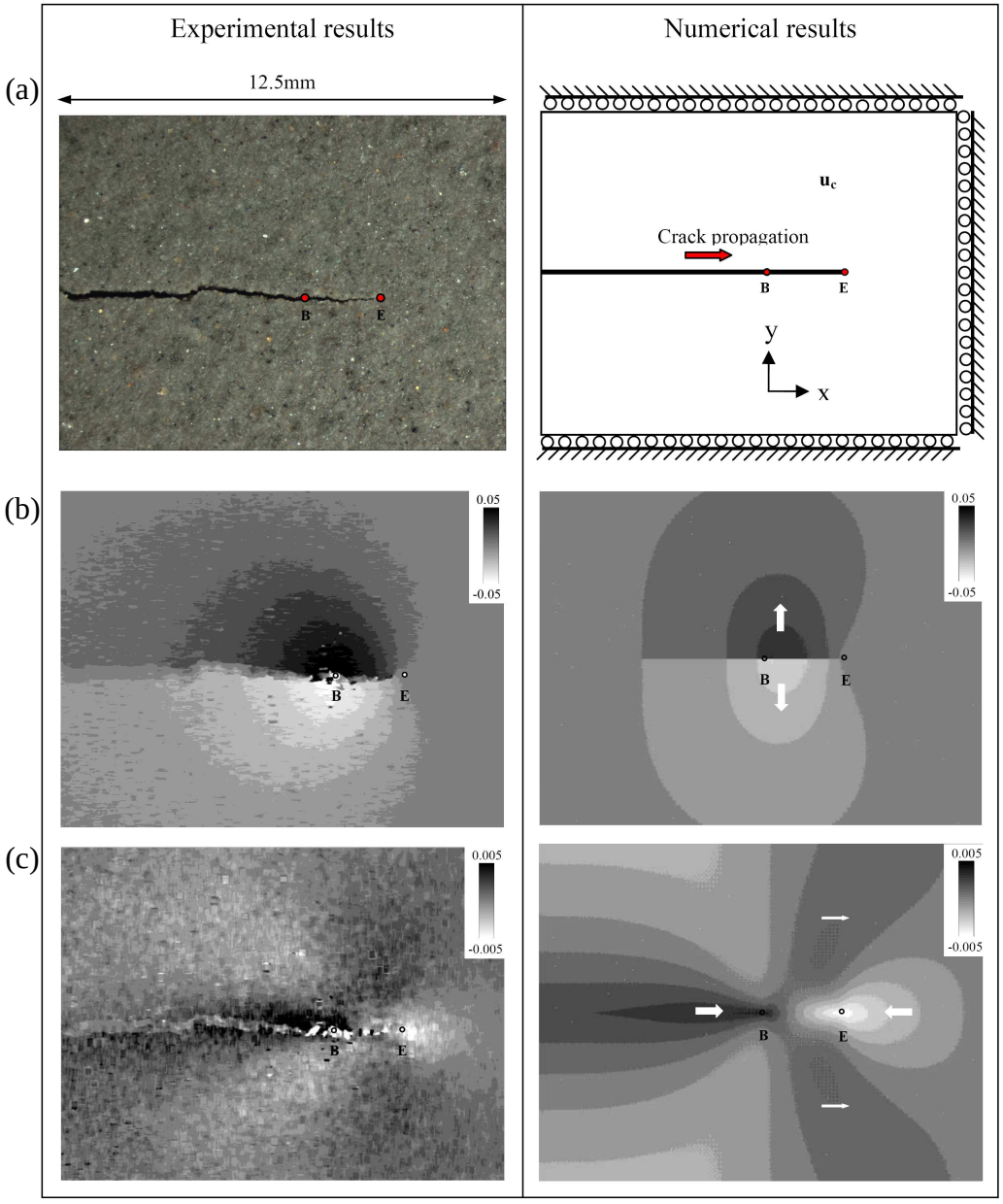

Figure 4.6 Displacement fields associated to a crack propagating from a beginning point B to the end point E. Comparison between experimental and numerical displacements. (a) Photograph and FEM model. (b) Displacement δ_y [mm] normal to the crack plane. (c) Displacement δ_x [mm] parallel to the crack propagation alignment. Soil: Ca-Montmorillonite; initial water content w=150%. Numerical simulation details in Table 4.2b - plane stress with suction u_c.The simulated domain size is 12mm long and 14mm wide (full length shown).

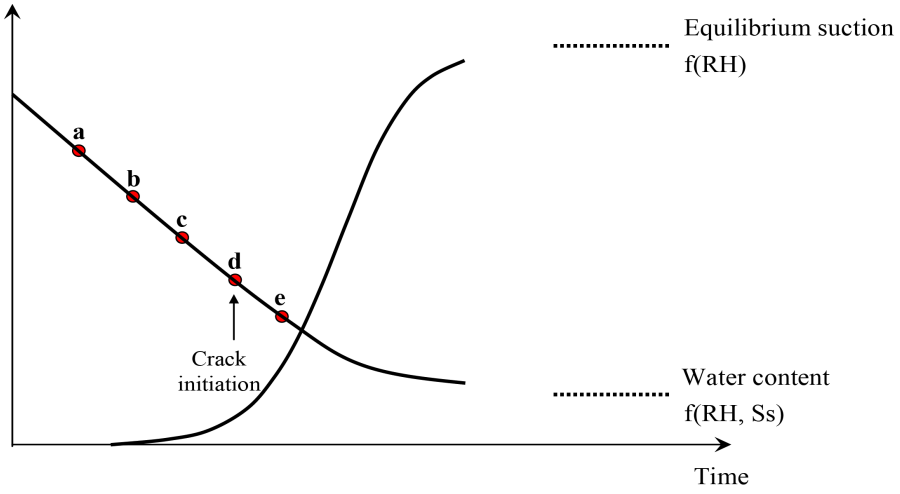

Stages	a	b	c	d	e
Global view	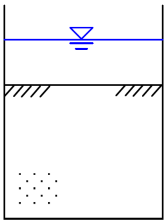	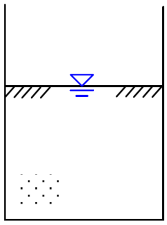	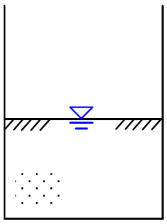	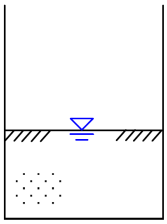	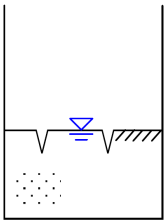
Particle scale view	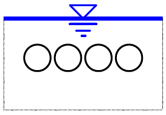 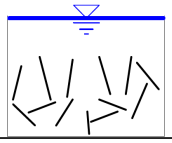	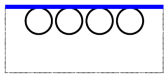 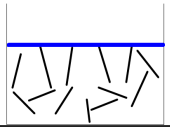	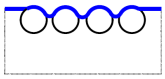 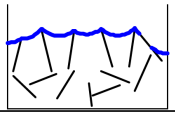	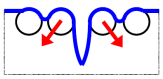 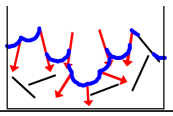	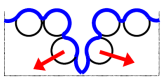 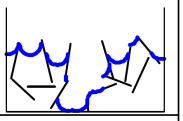
Comments	Evaporation of supernatant water No suction No strain in the soil skeleton	Air-water interface membrane reaches the soil surface	Membrane forms around soil particles Suction increases Consolidation of soil skeleton and increase in stiffness	Air invades the largest pores The air-water interface membrane pushes particles away from the invaded pore. Pore size increase at the tip and crack grows	Crack propagation and formation of polygons Vertical deformation ceases Eventually, the soil mass becomes unsaturated

Figure 4.7 Water evaporation, soil desiccation and crack formation - Summary of pore and particle scale processes.

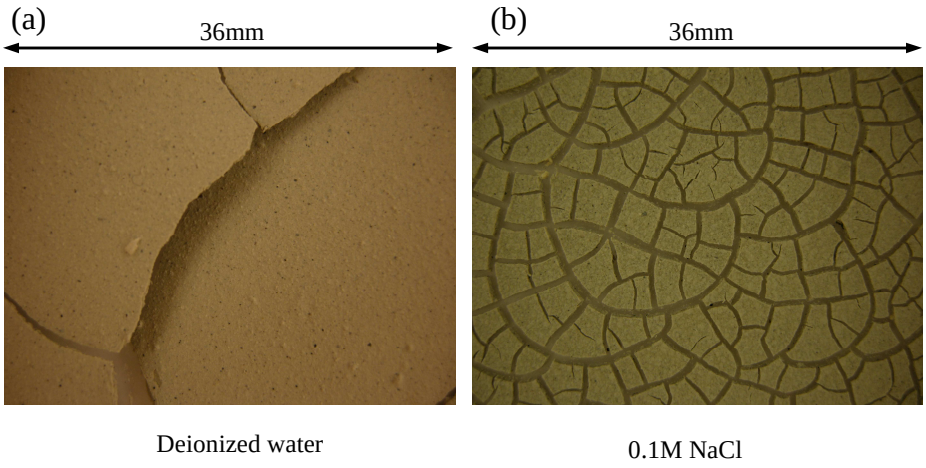

Figure 4.8 Effect of salt concentration on desiccation crack pattern. Na-Bentonite slurry prepared at an initial w = 1000%. Pore fluid condition: (a) Slurry mixed with deionized water. (b) Slurry mixed with 0.1M NaCl. Initial soil thickness is 2 mm in both tests.

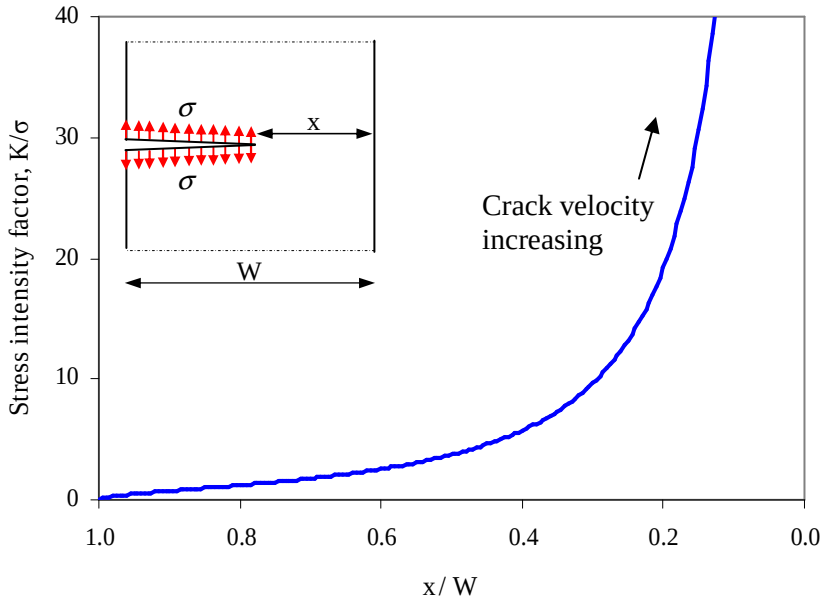

Figure 4.9 Change in stress intensity factor as the crack approaches a free boundary (Analytical solution in Stanford 2003).

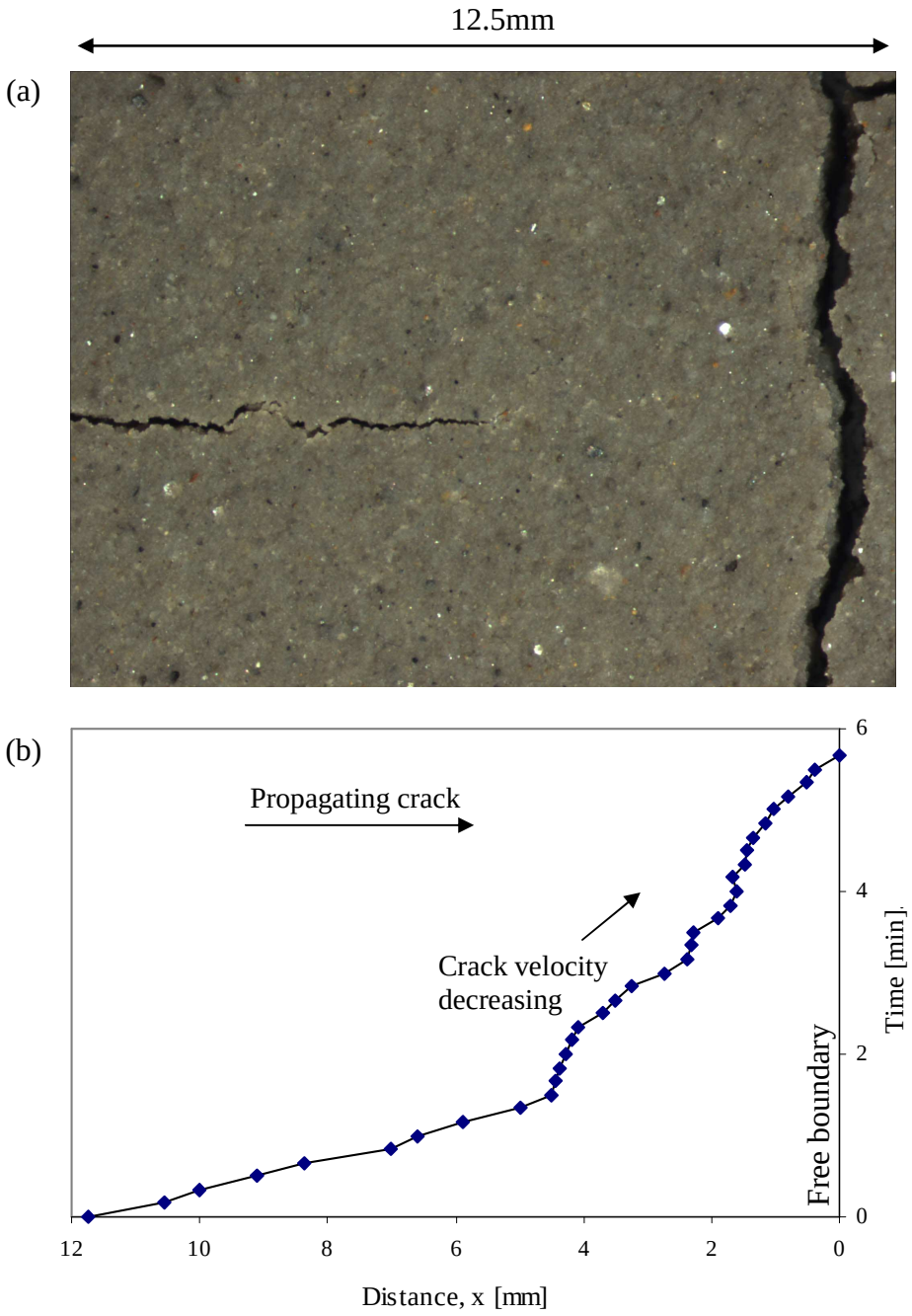

Figure 4.10 Desiccation crack propagation towards an existing crack or free boundary. (a) Micro photograph of crack tip at a distance x=4.8 mm from a preexisting crack. (b) Crack tip propagation versus time. Soil: Ca montmorillonite; initial water content w=150%.

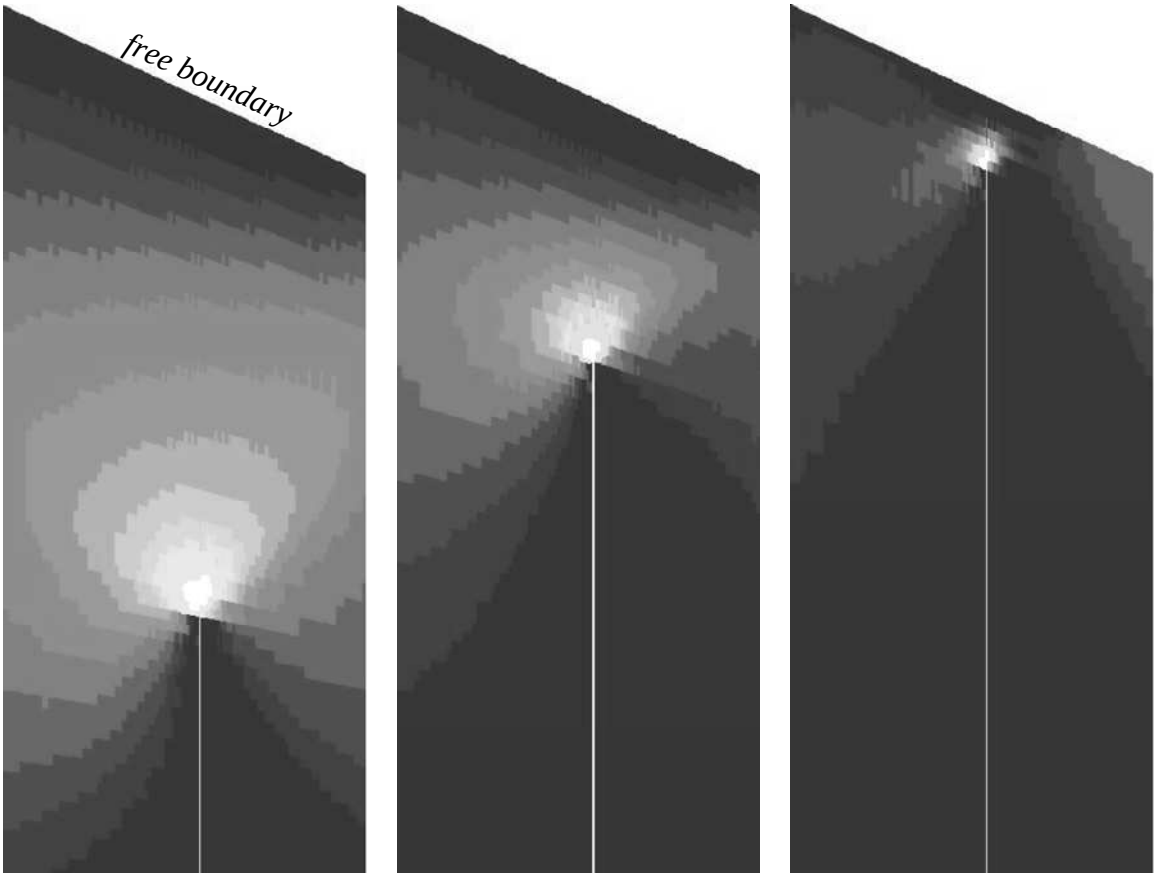

Figure 4.11 Void ratio evolution as the crack advances and approaches a skewed free boundary. The highest void ratio develops at the crack tip (white, e=2.35). The sediment consolidates along the crack behind the tip to reach e =2.05 (shown as dark gray). Model details in Table 4.2b - Plane stress with suction u_c. The simulation is 12mm long and 10mm wide; a 4 mm wide section of the simulated domain is shown.

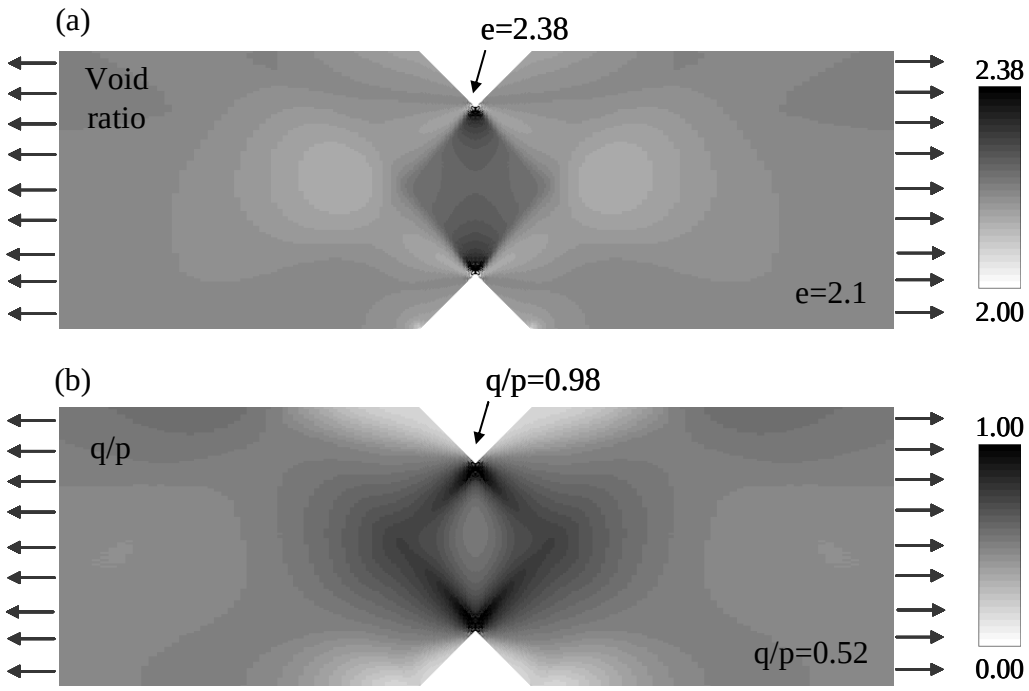

Figure 4.12 Tensile test simulation. Initial suction u_c=100kPa. Condition when a tensile stress σ=50kPa is applied: (a) Void ratio distribution. (b) Deviatoric stress ratio q/p. Model details in Table 4.2a.

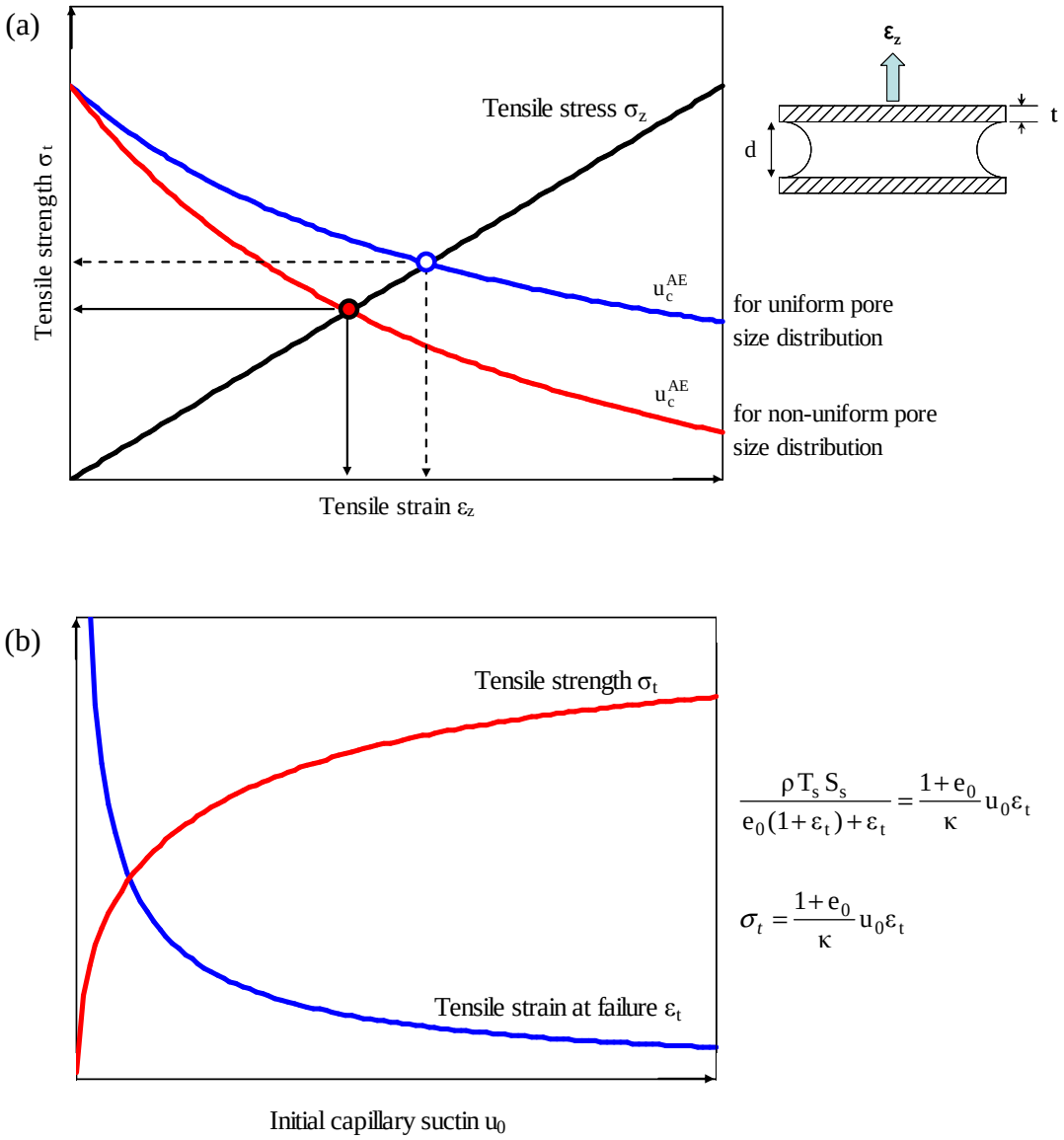

Figure 4.13 Theoretical "apparent tensile strength" from air entry suction: (a) Evolution of air entry suction and tensile stress with tensile strain increasing during tensile loading (both uniform and non-uniform pore size distributions). (b) Apparent tensile strength and tensile strain at failure at various initial capillary suctions.

CHAPTER 5

IMMISCIBLE FLUID DRIVEN FRACTURING IN GRANULAR MATERIALS

5.1 Introduction

Hydraulic fractures affect a wide range of geosystems, and environmental applications (Andersen, et al., 1994; Garagash, 2006; Massarsch, 1978; Soga, et al., 2006). Hydraulic fractures are central to the "geoplumbing" responsible for the development of oil reservoirs where natural fractures serve as migration paths, are extensively used to enhance productivity in oil and gas recovery, and to improve the injection capacity in waste disposal.

Fluid-driven fracture initiation and propagation in brittle solids are dominated by tensile failure (Bohloli and de Pater, 2006). This cannot be the case in cohesionless-frictional sediments where fluid-driven fracture initiation and propagation reflect the interaction between particles and invading fluids. Indeed, contrary to solid materials, uncemented granular materials - both fine and coarse grained- are already "separated" at the particle scale and exhibit no cohesion. Hence, soil behavior is effective stress dependent and is characterized by cohesionless-frictional strength: soils can carry no tensile stress so that stress states must be in compression everywhere. Yet, current hypotheses for fracture initiation still consider tensile failure, shear failure, or a combined failure mode.

Note that shear failure is compatible with Mohr-Coulomb's failure criterion. However, the observed predominant failure characteristics during hydraulic fracture in soils is in opening mode (e.g. Soft X-ray images from Toshikazu, et al., 2002), and the orientation is perpendicular to the minor effective principal stress, rather than in the 45°

orientation required for shear failure. Predictions based on total stress parameters may match the opening failure pressure, but they need to assume tensile resistance which can not be justified in effective stresses. These observations categorically imply that previous hypotheses for hydraulic fracture are not compatible with the fundamental behavior of uncemented granular materials.

While dry or drained granular materials fail only in shear (in agreement with the Coulomb criterion), saturated granular materials can couple granular behavior with fluid flow to give rise to opening type failure modes where the fracture walls are kept open by the interaction between the invading fluid and the granular medium.

Fluid pressure against an “even and homogenous” soil surface causes uniform compaction of a flat surface, and uniform cavity expansion of cylindrical or spherical surfaces (Jaworski, et al., 1981). Conversely, fluid-driven separation may develop when surface conditions lead to particle forces that prompt grain separation to favor “hydraulic wedging”. In other words, surface defects play a critical role for fracture initiation. Defects include discontinuities, existing cracks, loose packing adjacent to hard inclusions (Terzaghi, et al., 1996), topographic features, shrinkage distortion as in desiccation cracks (Towner, 1988; Weinberger, 1999). Porosity changes in fine grained soils can also be due to changes in pore fluid ionic concentration, permittivity or pH (Palomino and Santamarina, 2005; Zabat, et al., 1997). In particular, fine grained soils mixed with high concentration salt solutions form aggregated fabrics and exhibit larger pore diameters than dispersed fabrics at the same confining stress (Wang and Xu, 2007); large pores act as triggering points as well.

Particle level forces on the fracture walls are affected by the miscibility between the saturating fluid and the invading fluid. The main difference between immiscible and miscible fluid invasion is the presence of a fluid-fluid interface. The purpose of this study is to identify an effective-stress compatible mechanism for fracture formation and propagation in granular materials caused by the forced invasion of an immiscible fluid.

We identify particle-level mechanisms, and explore the macro-scale evolution of effective stress and void ratio with time. Together, particle-scale and macro-scale perspectives provide an unprecedented understanding of hydraulic fracture in granular materials.

5.2 Methodology

We study fluid-driven fracture formation in fine-grained soils using a combination of experimental and numerical methods.

5.2.1 Experimental devices and methods

Most experiments involve slurries prepared by mixing Ca-montmorillonite (Panther Creek 150; liquid limit=97%; plastic limit=47%; excess salts are expected) and deionized water (initial water content: 150%). The cylindrical, stainless steel chamber has a see-through window built in the top plate, and a porous stone on top of the drainage port in the bottom plate. A pressure port, pressure transducer, and an illumination port are attached to the side wall (Figure 5.1).

The slurry is initially placed in the oedometer cell (thickness ~25.4mm) and preloaded to σ'_z=2kPa. After consolidation for 24 hours, the top porous stone is carefully removed to prevent disturbing the soil surface. Oil is placed over the specimen (safflower oil with colorless and transparent, viscosity μ=50cP). Then, the top cap is assembled and the fluid is pressurized to the desired value while allowing no drainage through the bottom port.

The chamber sits under an optical microscope (LEICA MZ6) augmented with a digital camera (Qimaging) to obtain high resolution digital photographs (0.8 to 5 μm/pixel resolution). Soil surface also is photographed using a digital camera operating

in time-lapse mode (Nikon Coolpix P5000; 3468×2736 pixels; resolution 0.013mm/pixel; photograph every 30 sec).

The time-dependent fracture process starts when the bottom drainage port is opened. We monitor the effluent mass with time (Pinnacle 6001 with 1 mg resolution). Images are gathered every 15 sec. Successive images captured from the microscope are compared using digital image correlation to compute horizontal displacement and strain fields (Matlab code modified from UraPIV). This test configuration and measurement allow us to obtain detailed information on fracture initiation and propagation mechanisms.

5.2.2 Numerical model and boundary conditions

Complementary numerical simulations are run to gain additional information not attainable through experimentation. All studies are conducted in terms of effective stress. We represent contractive soils using the Modified Cam Clay model, and dilative soil conditions adopting the Hvorslev surface (Muir Wood, 1990; Schofield, 1980), to avoid overestimating the peak shear strength (Bolton and Britto, 1993; Bolton, et al., 1989). Zero soil cohesion is assumed in all cases and imposed through a tension cut-off boundary. Other constitutive model parameters, simulation details and boundary conditions are summarized in Table 5.2.

5.3. Results from the experimental study

Experimental observations confirm the relevance of surface defects on fracture initiation. In our tests, sub-millimeter surface defects form before pressurization or appear during pressure diffusion. Open fractures always start at these defects, and they propagate sideways towards the cell wall (Figure 5.2).

Drainage starts immediately after opening bottom drainage port. However, there is a time delay for fracture initiation. Hence, hydraulic fracture formation is intimately

linked to pressure diffusion. The fracture propagation velocity is high soon after fracture initiation, but it decreases with time. The effluent flow rate shows a marked change at the time of fracture formation (Figure 5.3). If bottom drainage is closed after crack initiation, propagation is halted and the fracture stays open (slow creep). This implies that the driving force for fracture propagation with immiscible fluids vanishes in a closed system.

5.4. Analytical and numerical results

Analyses and numerical simulations are conducted to investigate the underlying mechanisms in the formation of hydraulic fractures driven by the forced invasion of an immiscible fluid. In these studies, we explicitly recognize the particulate nature of granular materials and the decisive role of surface defects on fracture initiation.

5.4.1. Development of capillary pressure during fluid pressure diffusion

Capillary pressure is the pressure difference between the invading fluid and the host fluid in the soil. The effective normal stress acting on the sediment at the free boundary is the capillary pressure.

Just before fluid invasion, the interfacial membrane between the two immiscible fluids has no curvature, thus, it mobilizes zero capillary pressure and it exerts zero normal effective stress on the soil surface (Figure 5.4). As the host fluid pressure decreases during consolidation, the interfacial membrane starts to increase its curvature, capillary pressure increases and the effective stress at the soil boundary increases as well. Initially, the increased capillary pressure causes vertical compaction only.

5.4.2 Capillary pressure at fracture initiation P_C

The capillary pressure at fracture initiation P_C is the maximum pressure difference the granular material can resist against the advancing interfacial membrane. The pore size

at the particle-scale determines P_C. Based on Laplace's equation, the capillary pressure at fracture initiation P_C for parallel platy particles of thickness t and mean distance is

$$P_C = \frac{2\,T_S \cos(\theta)}{\bar{d}} = \frac{\rho\,T_S\,S_S \cos(\theta)}{e} \tag{5.1}$$

where void ratio is estimated as $e = \bar{d}/t$, the specific surface is $S_S[m^2/g]=2/(\rho t)$, $\rho[kg/m^3]$ is mass density of particles, surface tension between two contacting fluids is T_S [N/m], and the advancing contact angle is θ.

Sediments have a non-uniform pore-size distribution (Garcia-Bengochea, et al., 1979; Juang and Holtz, 1986; Tanaka, et al., 2003). The interfacial membrane will invade large pores first. Hence, the capillary pressure at fracture initiation P_C will be lower in a soil with non-uniform pore size distribution than in a soil with uniform pore size distribution at the same global void ratio. Let's assume a log-normal pore size distribution. The standard deviation σ* in logarithmic scale log(d/1μm) is typically between $0.3 \le \sigma^* \le 0.7$. The "characteristic pore diameter" d^* on the soil surface that determines massive invasion can be defined as a pore size that is larger than the mean pore size $\log(\bar{d}/1\mu m)\cdot\log(\alpha\sigma^*)$, then

$$d^* = \bar{d}\cdot 10^{\alpha\sigma^*} \tag{5.2}$$

The statistically modified capillary pressure at fracture initiation P_C becomes

$$P_C = \frac{\rho\,T_S\,S_S \cos(\theta)}{e}\,\frac{1}{10^{\alpha\sigma^*}} \tag{5.3}$$

The normalized parameter $\alpha \equiv \log(d^*/\bar{d})/\sigma^*$ determines the percentage of surface pores invaded at P_C.

5.4.3. Void ratio evolution during fracture initiation

The membrane acts against the walls of large pores and surface defects to distort the distribution of void ratio and effective stress on the soil surface while the internal fluid pressure diffuses towards the bottom drainage. Numerical simulation shows that the

existence of surface defect distorts the distribution of void ratio and effective stress during pressure diffusion, especially void ratio follows quite different path near the surface defect (Figure 5.5).

The void ratio contracts following the 1D normal consolidation line in the far field away from a surface defect (1D - “I” in Figure 5.6), and it decreases even more around the edge of a surface defect due to quasi-isotropic membrane compression (~isotropic - “II” in Figure 5.6). However, the void ratio increases or it remains higher than anywhere else (“III” in Figure 5.6).

The higher local void ratio at the tip of a surface defect implies a lower P_C for membrane invasion, leading to fracture initiation at the tip (Equation 5.1). Note that it is not necessary for the tip void ratio to increase during pressure diffusion; it only has to be the maximum void ratio along the soil surface so that the membrane invades it first.

Once the membrane invades the soil mass at the tip, further wedge action leads to a sustained increase in local void ratio at the advancing fracture tip and cause fracture propagation.

5.4.4 Effect notch geometry on initial propagating direction

The scale of surface defects such as dimples and notches is typically much larger than the scale of pores in fine-grained soils. In fact, there are experimental results that show that notches have little or no effect on the fracture initiation pressure (Alfaro and Wong, 2001; de Pater and Dong, 2007; Yanagisawa and Panah, 1994). Furthermore, fractures may not necessarily initiate at notches, or the direction of the notch does not necessarily define the orientation of the propagating fracture which may choose an angle of ~45º with the notch or perpendicular to the direction of the least principal stress. When misinterpreted, these observations may mislead us to conclude that the shear failure hypothesis is valid for hydraulic fracture. In this section, we reconsider the effect of notches on the fracture initiation pressure and direction of fracture propagation.

The numerical simulation study investigates the effect of notch geometry on changes in local void ratio. Once again, we select a soil-type model (Cam-Clay) and plane strain conditions (details in Table 5.2a).

Numerical results show that a relatively wide notch t/L≈0.25 produces a high increase in void ratio in the oblique direction at corners (Figure 5.7a). Therefore, the fracture would appear to grow at an angle, giving the false impression of a shear failure. This is not the case in slender notch t/L<<1 (Figure 5.7b) where the increase in void ratio is clearly aligned with the direction of the notch, prompting fracture propagation along the notch direction.

We conclude that the slenderness t/L of notches determines fracture opening, changes in local effective stress and void ratio, and the invasion of the interfacial membrane leading to hydraulic fracture in granular materials.

Experimental (Figure 5.2) and numerical evidence (Figure 5.5 and 5.7) clearly show the relevance of surface defects (mm size scale) in fracture initiation. However, it is important to highlight that the capillary pressure at fracture initiation P_C is determined by pore size (d-scale) as given by Equation 5.1 or 5.3. In other words, the particle scale defines the pore size for membrane invasion, but the scale and geometry of surface defects cause local changes that favor fracture nucleation.

5.4.5 Fracture initiation time

The fracture initiation time in the test configuration selected for this study is controlled by pressure diffusion and can be estimated using consolidation theory, and the imposed pressure and flow boundary conditions (P=0 at z=0, ∂P/∂z=0 at z=H). The host fluid pressure distribution with depth z and time t is (Figure 5.8a):

$$P(Z,T) = \sum_{n=0}^{\infty} \frac{2P_0}{M_n} \sin(M_n Z) \exp\left(-M_n{}^2 T\right) \qquad (5.4)$$

where P_0 is fluid pressure applied to the oil that fills the cell, $M_n = \frac{\pi}{2}(2n+1)$, the dimensionless depth is Z=z/H and dimensionless time is $T = c_v t/H^2$. The interfacial membrane invades the sediment and triggers fracture initiation, when the capillary pressure at the surface z=H, P_0-P(H,t), reaches the capillary pressure at fracture initiation P_C in Equation 5.1 (Figure 5.8c).

Measured fracture initiation times are plotted and compared against predictions in Figure 5.8d. The diffusion coefficient c_v is inverted from flow data (Figure 5.8b). Note that:

- The fracture cannot develop if the applied pressure is lower than $P_0<P_C$; in this case, only vertical compaction is measured in the oedometer cell.
- The fracture initiation time decreases asymptotically as the applied fluid pressure P_C increases.

5.4.6 Fracture propagation

In analogy to fracture initiation, we anticipate that the tip void ratio will increase during fracture propagation, lowering the capillary pressure at fracture initiation P_C to form membrane invasion and fracture propagation. We test this growth mechanism using a three-dimensional model of a homogeneous, single layer with a transverse fracture. Constant external pressure (applied fluid pressure) is applied on the top of the layer. The constitutive model for the sediment and boundary conditions are summarized in Table 5.2b.

The invading fluid pressure is applied on the fractured walls. The excess host fluid pressure diffuses through the far field boundaries in time. Results confirm that the void ratio at the fracture tip is higher than anywhere else favoring fracture growth, which is modeled by disconnecting the node that exhibits highest extension. After fracture growth, the stretched sediments that were at the previous tip location become part of the wall, reconsolidate under the imposed capillary pressure and the void ratio decreases

(Figure 5.9). The horizontal effective stress is highest on the fracture walls and decreases to the far field stress behind the tip

5.4.7 Fracture separation - Saturation

All surface defects are potential nucleation points for fracture initiation. However, the fracture density does not increase monotonically with capillary pressure. In fact, the degree of fracturing evolves towards an asymptotic saturation state (Bai, et al., 2000). Within the model hypothesized above, successive fracturing towards saturation would proceed as follows: (1) few fractures start at the largest pores, (2) as the capillary pressure increases, the soil mass becomes stiffer, and new pores are invaded triggering new fractures, (3) eventually, the soil is stiff enough that invasion causes no further strain nor fracture (i.e., saturation), and the medium is massively invaded by the immiscible fluid.

The block size B at fracture saturation can be estimated following invasion concepts hypothesized in this study. Let's assume a mean pore diameter $\bar{d}$ (Figure 5.10a), and a log-normal distribution of pore sizes. The characteristic pore diameter when a fracture initiates $d^* = \bar{d}10^{\alpha\sigma^*}$ is at a distance $\alpha\sigma^*$ from the mean $\bar{d}$. The probability of pores being $d > d^*$ is

$$F(\alpha) = \frac{1}{2}\left[1 - \frac{2}{\sqrt{\pi}}\int_0^{\alpha/\sqrt{2}} \exp\left(-t^2\right)dt\right] \qquad (5.5)$$

For a card-castle arrangement of platy particles of thickness t, porosity is estimated as $n \approx \bar{d}/(\bar{d} + 2t)$, and specific surface is $S_S=2/(\rho t)$. In the domain size L×L, the area of pores is $A_p = n \cdot L^2 = e \cdot L^2/(1+e)$, and the number of pores on the surface can be estimated as $N_p = A_p/\bar{d}^2$. When the number of potential fracturing pores is $N_P \times F(\alpha)$, the saturated fracture spacing is $B = L/\sqrt{N_p F(\alpha)}$ for a homogeneous spacing of pores on the plane. Combining these expressions, the fracture spacing is when pore size d* are invaded is

$$B = 4\sqrt{\frac{e(e+1)}{F(\alpha)}}\frac{1}{\rho S_S} \quad \text{for invaded pore size} \quad d^* = \bar{d}10^{\alpha\sigma^*} \quad (5.6)$$

where ρ [g/cm3] is the mass density of the particle. The observed distance between small surface defects and analytical predictions using Equation 5.6 are plotted in Figure 5.10b and 5.10c.

The analysis can be extended for saturation, however, we need to know the evolution of pore size with capillary pressure or effective stress. Conversely, knowing the capillary pressure at fracture saturation, we can compute the corresponding characteristic pore size d* (Equation 5.3), determine the value of $\alpha = \log(d^*/\bar{d})/\sigma^*)$ and predict the block size at fracture saturation with Equation 5.6.

5.5. Discussion

The previous section presented experimental, analytical and numerical results on the mechanisms for immiscible fluid driven fracture initiation and propagation. The central role of the invading interfacial tensile membrane was highlighted. In this section, we extend these concepts and explore their implication to field situations.

5.5.1 Fracture pressure in boreholes

The most common situation for hydraulic fractures is around boreholes. Let's explore this case within the framework of hydraulic fracture mechanisms with immiscible fluids identified above.

The borehole experiences axi-symmetric cavity expansion during the early stages of pressurization. The capillary pressure at fracture initiation P_C decreases as the tangential extensional strain ε_θ around the borehole increases. Then Equation 5.1 becomes:

$$P_C = \frac{\rho T_S S_S \cos(\theta)}{e(1+\varepsilon_\theta)}\frac{1}{10^{\alpha\sigma^*}} \quad (5.7)$$

Cavity expansion will continue until the borehole pressure reaches $P_{bore}=P_C$ and a fracture initiates. An explicit analytical solution does exist for the critical state constitutive model, therefore numerical simulation is used to estimate the tangential strain ε_θ at the borehole wall with increasing pressure and the corresponding fracture pressure. The simulated geometry, boundary conditions and sediment model are summarized in Table 5.2c.

Results in Figure 5.11 show that the required fracture pressure can be 2-to-6 times higher than the in situ confining stress at shallow depth, however the difference between fracture pressure and confining stress decreases with increasing depth; still, the borehole pressure needed to form an open fracture remains greater than the in situ confining stress. The decrease in sediment stiffness and/or friction (i.e., shear strength parameter M) results in reduced fracture pressure because of the additional volumetric contraction around the borehole in Figure 5.11. Finally, the applied fluid pressure for hydraulic fracture initiation is a summation of capillary pressure at fracture initiation P_C determined by effective confining stress and in-situ fluid pressure.

5.5.2 Boreholes in an anisotropic stress field: Fracture reorientation

Hydraulic fractures orient normal to the minor principal stress in both cohesive and granular media (Lachenbruch, 1962; Wright and Weijers, 2001). The particle-scale mechanisms that define fracture orientation in granular media are explored herein.

Let's apply the Cam-Clay type soil model described earlier to study changes in void ratio (i.e., pore size and membrane invasion) at fracture tips in a 2D plane strain configuration (model details in Table 5.2a). We consider two cases: near the borehole and far away from the borehole wall. The imposed far field effective stress is anisotropic $\sigma'_2 = \sigma'_3$ and the far field pore pressure is kept constant.

Results are summarized in Figure 5.12. When the fracture tip is close to the borehole, r=0.3R, deformation mode is in the radial direction and controlled by the

applied borehole pressure. The prevalent direction for void ratio changes is normal to the borehole, and the far field stress anisotropy has a minor effect on the direction of fracture propagation (Figure 5.12a). However when the fracture tip is at a distance r ≥ 2R, changes in void ratio rotate towards a plane perpendicular to the least principal stress and the propagating fracture aligns in this direction (Figure 5.12b).

5.5.3 Two end-members in hydraulic fracturing

Distinct failure mechanisms explain hydraulic fracture initiation and propagation in granular media depending on the miscibility between invading and host fluids (Table 5.3). Both fractures are opening-type failure mode in granular media, and their initiation and propagation must be effective stress compatible.

Hydraulic fracture driven by the invasion of an immiscible fluid does not involve invading fluid leak off into the sediment, and the host pore fluid diffuses away from the surface as part of the imposed consolidation. The capillary pressure at fracture initiation P_C is high for fine-grained soils and it can effectively cause the wedge action that will promote open fracture propagation ("a" in Figure 5.13).

This is not the case in coarse-grained soils where the capillary pressure at fracture initiation P_C is much lower as can be estimated for the packing of spherical particles of radius R:

$$P_C = \frac{2\,T_S/R}{\sqrt[3]{\frac{2}{3}\pi(1+e)} - 1} \qquad (5.8)$$

In this case, the capillary pressure is not enough to displace particles and the interfacial membrane invades the sediment when it exceeds the capillary pressure at fracture initiation P_C, and it causes no localized opening ("b" in Figure 5.13).

Hydraulic fracture initiation in granular media driven by miscible fluid requires sufficient flow rate and drag to open and support the fracture walls (filter-cake formation

helps create the drag force in Khodaverdian and McElfresh, 2000). Then, it is the seepage force associated to the hydraulic gradient that generates the effective stress field within the soil mass to drive the opening mode fracture when miscible fluids are involved (Figure 5.13d). The tip of the propagating fracture experiences a positive-feedback condition between void ratio (pore size) and hydraulic gradient (e.g. Kozeny-Carman equation) because the direction of increasing hydraulic conductivity is orthogonal to the acting seepage force. Combined conditions may develop where seepage and capillary forces add to cause the localization ("c" in Figure 5.13).

5.6. Conclusions

Fluid-driven hydraulic fracture initiation and propagation in granular materials have been explained either as tensile failure or shear failure, in part due to apparent similarities with fracture patterns in solid materials. However, contrary to solid materials, the behavior of "already fractured" frictional granular materials is governed by effective stresses. Hence, previous hypotheses are not compatible with the fundamental characteristics of granular materials. Furthermore, the miscibility of the invading fluid and host fluid leads to distinct failure mechanisms.

A fundamental, effective stress compatible understanding of hydraulic fracture driven by the forced invasion of an immiscible fluid in granular materials is suggested. It centers on the development of a higher local void ratio at the tip of surface defects to facilitate the invasion of the interfacial membrane into the soil mass. This is the starting point for immiscible fluid driven fracture formation in fine-grained soils. Once the membrane invades, wedge action at the tip increases the local void ratio to sustain fracture propagation.

The presence of a surface defect does not necessarily lead to fracture initiation: fracture initiation and the required capillary pressure are pore-scale phenomena. The

geometry of surface defects must lead to higher void ratio and larger pore diameter at the tip to facilitate membrane invasion for fracture initiation. The slenderness of notches determines their effect on fracture initiation and early propagating direction.

Hydraulic fracture formation is not an undrained problem, but it is intimately linked to pressure diffusion to cause the needed capillary pressure at the soil surface. Thus, the fracture initiation time depends on the applied fluid pressure and the diffusion coefficient. Furthermore, a fluid pressure lower than the critical pressure causes vertical compaction only.

The borehole pressure needed to initiate a fracture can be several times higher than the confining stress at shallow depth; however, the pressure difference decreases with increasing depth. Low sediment stiffness and shear strength decrease the fracture initiation pressure due to the high volumetric deformation and enlarge pores around the borehole.

Confining stress anisotropy determines the direction of fracture propagation normal to the minor principal stress when the fracture has reached far field of the borehole ($r/R>2$). However, the fracture propagates normal to the borehole wall in the near field ($r/R<1$) due to the isotropic stress field imposed by the pressured fluid inside the borehole.

Contrary to hydraulic fracture with immiscible fluids, the driving force for fracture initiation with miscible fluids is the seepage force. The increase in void ratio and hydraulic conductivity at the tip of the fracture can couple to exhibit the runaway positive feedback that causes the hydraulic fracture.

Open fracture formation with the two different types of fluid suggests new emergent failure mechanism in granular materials as a result of fluid-sediment interaction.

Table 5.1 Hydraulic fracture in granular materials - Previous hypotheses

Failure	Mechanism	Reference
Tensile	The seepage drag force caused by excess fluid pressure causes tensile stress until the tensile strength is reached under steady state condition	Bjerrum, et al., 1972
	Fluid pressure during injection under undrained condition exceeds the tensile strength	Andersen, et al., 1994
	The difference between σ'_r and σ'_θ caused by the injection pressure causes shear deformation and excess pore pressure	Alfaro and Wong, 2001
	A uniform increase in the pore water pressure in continuous and homogeneous soil mass will not result in tensile stresses and will therefore not lead to hydraulic fracture. But the presence of discontinuities leads to tensile stress through a wedge action by the fluid onto the soil	Jaworski, et al., 1981; Terzaghi, et al., 1996
Shear	Shear failure in total stress analysis (Mohr-Coulomb failure criterion)	Atkinson, et al., 1994; Komak Panah and Yanagisawa, 1989; Mori and Tamura, 1987
	Localized shear band from a small-scale boundary instability of the initial cavity expansion	Chang, 2004; Wu, 2006
	Non-uniform deformation around a borehole due to plastic instability, followed by tensile strain development induced at the fracture tips	Soga, et al., 2006

Table 5.2 Numerical simulation: Geometry and constitutive model

<table>
<tr><td colspan="3">Element type and boundary conditions</td></tr>
<tr>
<td>(a) Study reported in Figure 5.5,5.7 and 5.12
▪ Element type: 8 node displacement and 4 node pore pressure, 2D plane strain
▪ No friction against boundaries
 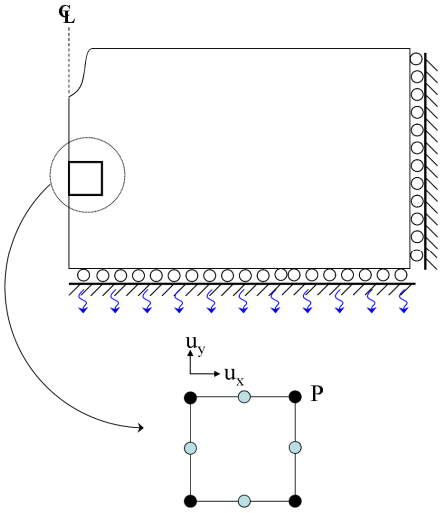
</td>
<td>(b) Study reported in Figure 5.9
▪ Element type: 20 node displacement and 8 node pore pressure, 3D
▪ No friction against boundaries
 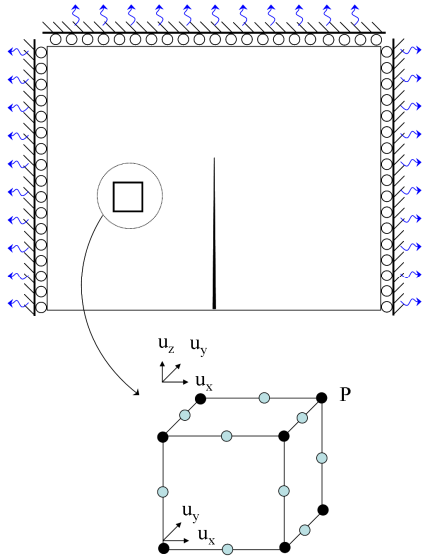
</td>
<td>(c) Study reported in Figure 5.11
▪ Element type: 8 node displacement, 2D-axisymmetric
▪ No friction against boundaries
 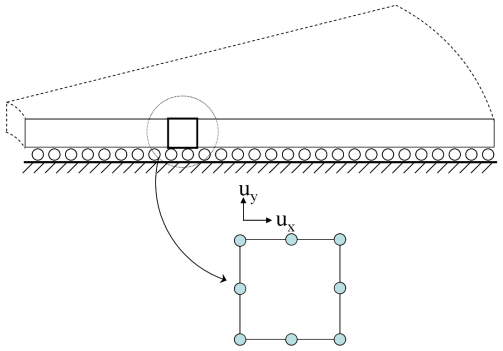
</td>
</tr>
<tr><td colspan="3">Model and material properties
▪ Constitutive model: Modified Cam clay model on the wet side; Hvorslev surface and tension cut-off on the dry side. Associated flow rule
▪ Soil properties: normally consolidated , compression index C_c=0.46, swelling index C_s=0.15, void ratio at 1 kPa e_{1kPa}=3, failure stress ratio M=1.2, Drained Poisson’s ratio ν=0.3</td></tr>
</table>

Table 5.3 Hydraulic fracture in granular materials: Comparison between two end-members

Fluid type	Immiscible fluid	Miscible fluid
Driving force	Interfacial membrane → capillary force	Seepage drag force on soil particles
Mechanism	Interfacial membrane preferentially invades the largest pores first → change pore size → wedge action for further invasion	Preferential seepage into large pores → increase in local porosity → increase in hydraulic conductivity → runaway positive feedback
Applications	Air-water: Desiccation Oil-water: Enhanced oil recovery Ch_4-water: Gas production -hydrate CO_2-water: CO_2 sequestration	Typical hydraulic fracture

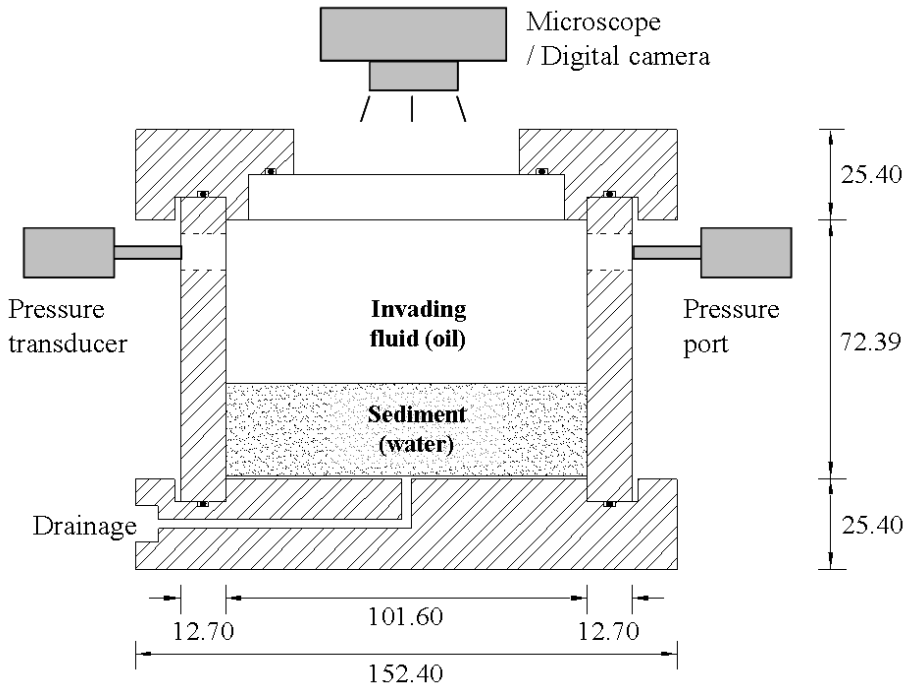

Figure 5.1 Experimental device for hydraulic fracture tests. Cylindrical, stainless steel chamber with a see-through window on the top cap. (unit: mm)

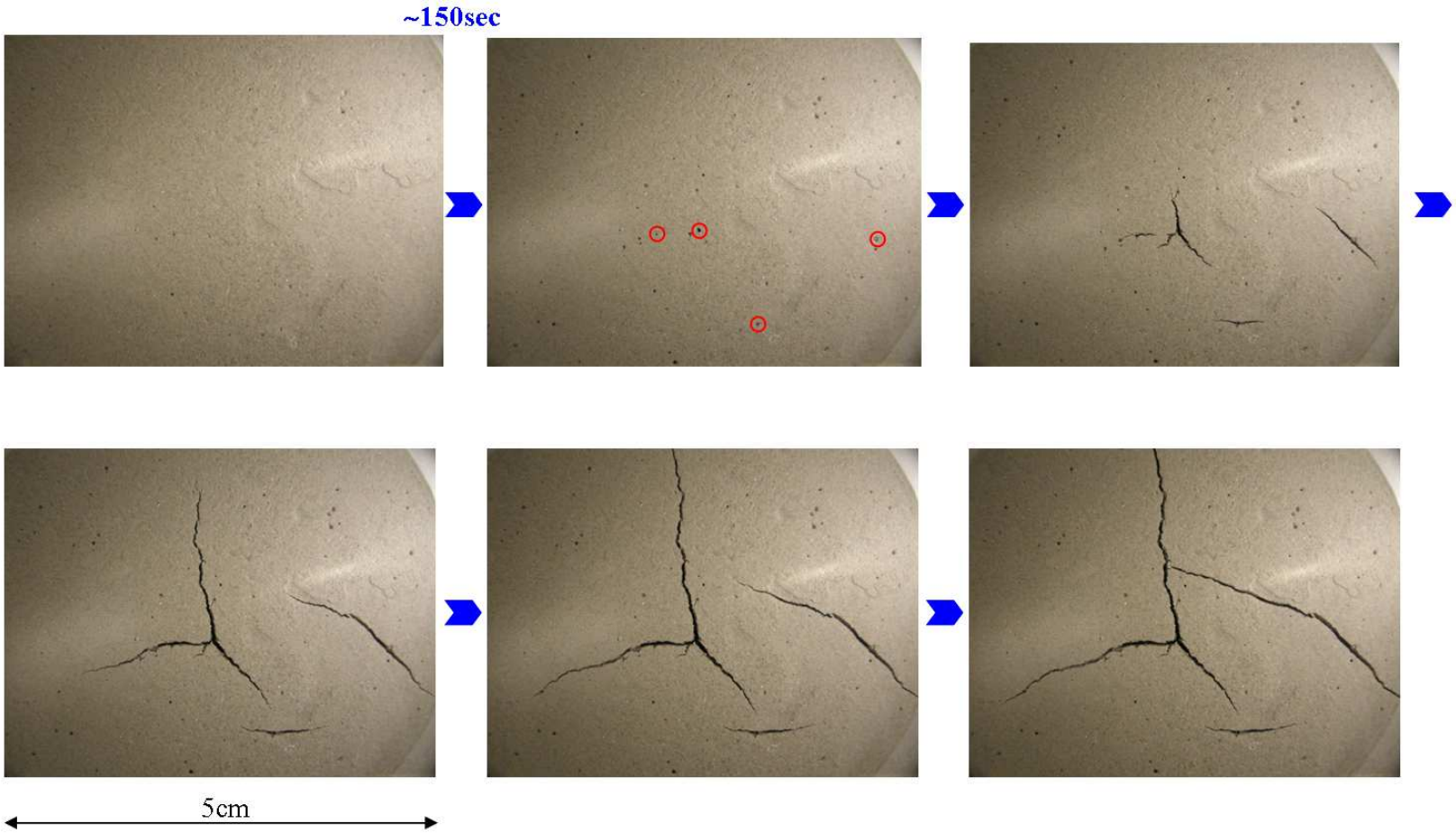

Figure 5.2 Evolution of hydraulic fractures observed at the soil surface. Very soft, water saturated bentonite sediment invaded by immiscible oil subjected to a fluid pressure u=200 kPa (red circles in the second frame highlight fracture initiation points).

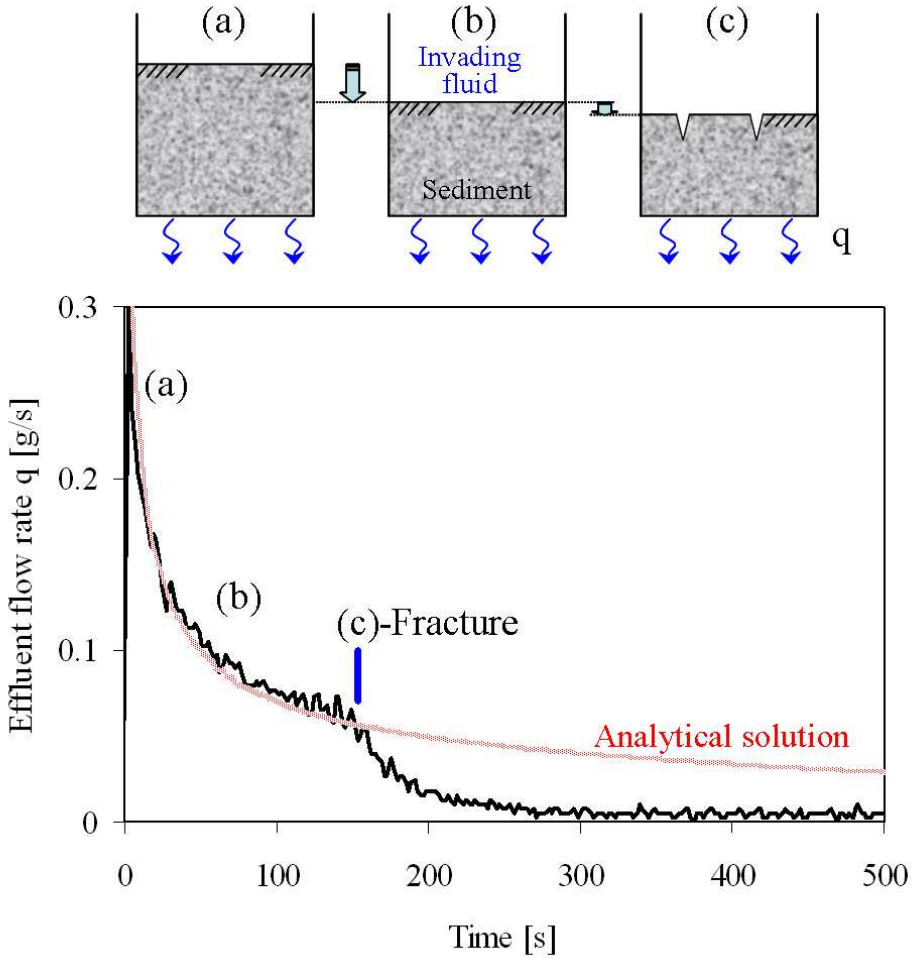

Figure 5.3 Effluent flow rate. Very soft, water saturated bentonite sediment invaded by immiscible oil subjected to a fluid pressure of u=200 kPa. The analytical solution from 1D pressure diffusion equation is superimposed on the data (refer to section 5.4.5).

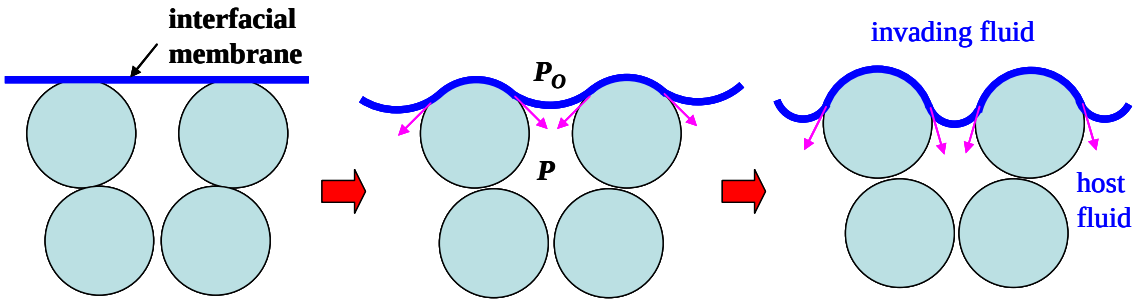

Figure 5.4 Schematic particle-scale diagram for the progressive invasion of the interfacial membrane into the granular medium eventually leading to the formation of hydraulic fractures. The pressure difference across the membrane is the capillary pressure that causes interparticle forces.

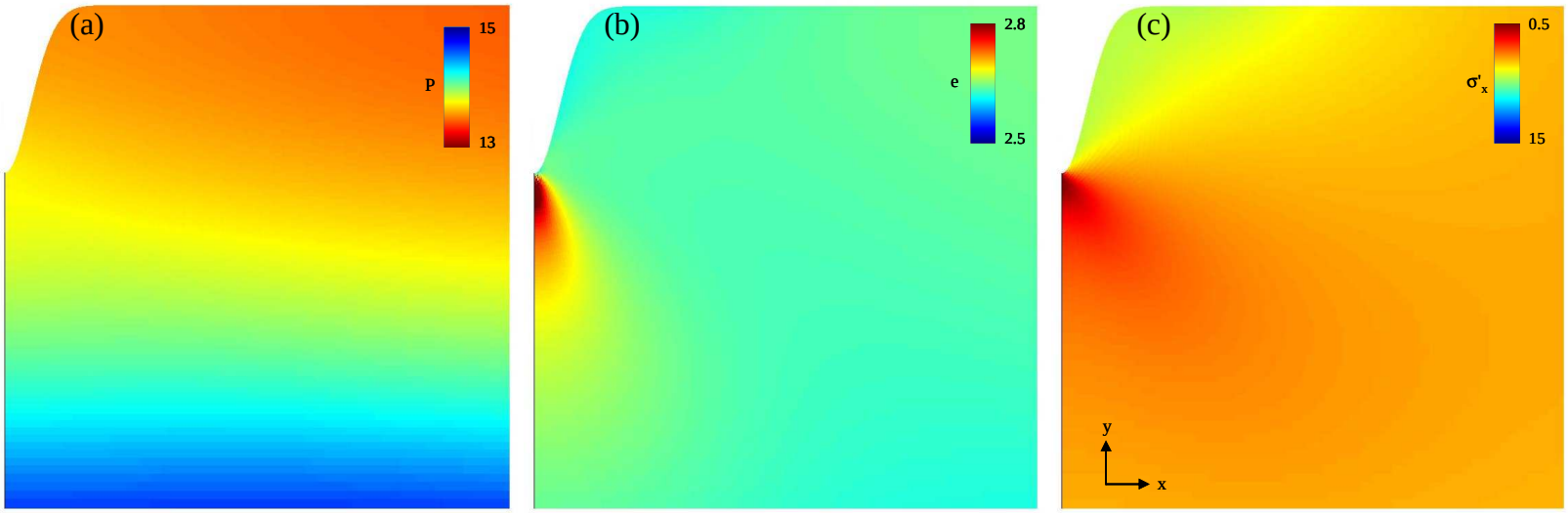

Figure 5.5 Numerical simulation on fracture initiation. Evolution of surface defects when an immiscible fluid is forced to invade a granular mass. Results shown at dimensionless time T=0.33. Distribution of (a) pore pressure, (b) void ratio, and (c) horizontal effective stress. Bottom drainage (refer to Table 5.2a for boundary conditions and material properties)

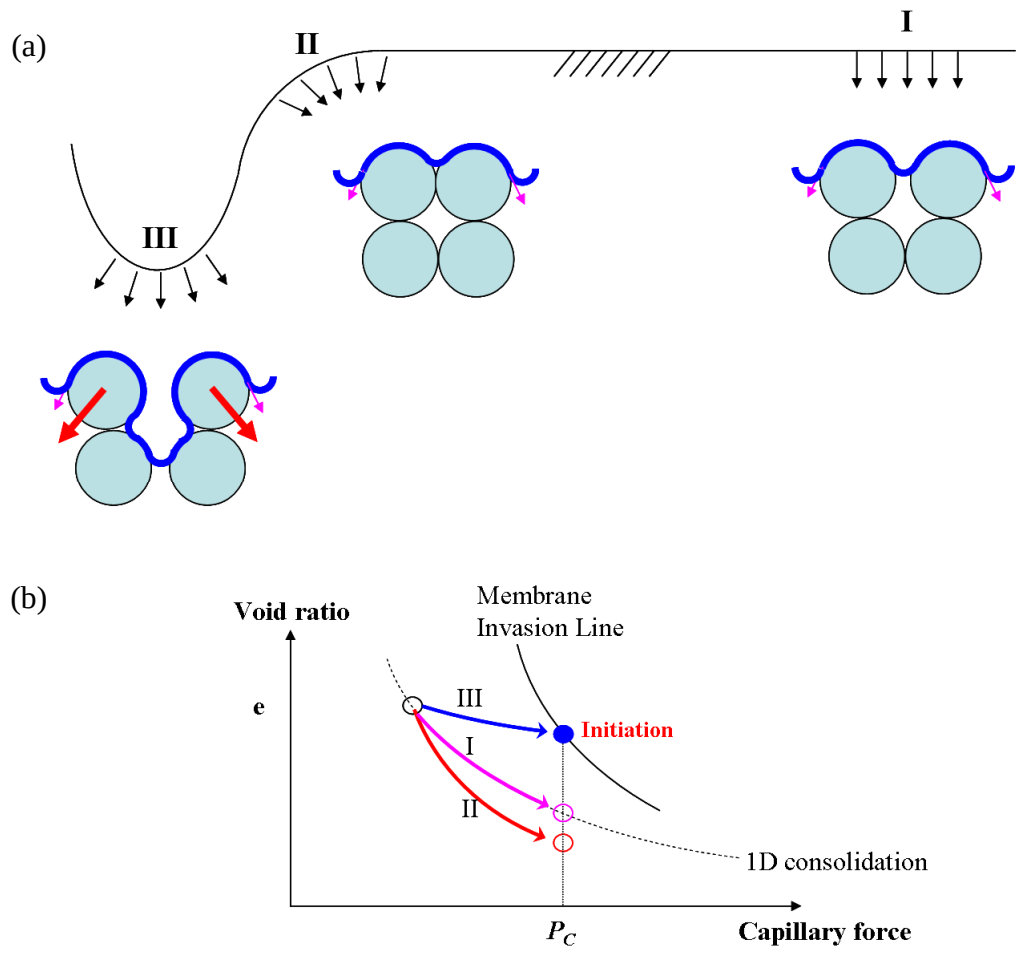

Figure 5.6 The evolution of void ratio and capillary stress along the soil surface. (a) Schematic diagram, (b) The line for the capillary pressure at fracture initiation P_C by membrane invasion corresponds to Equation 5.1. The 1D consolidation line captures $e=e_{atm}-C_C \log(P_C/atm)$.

(a)

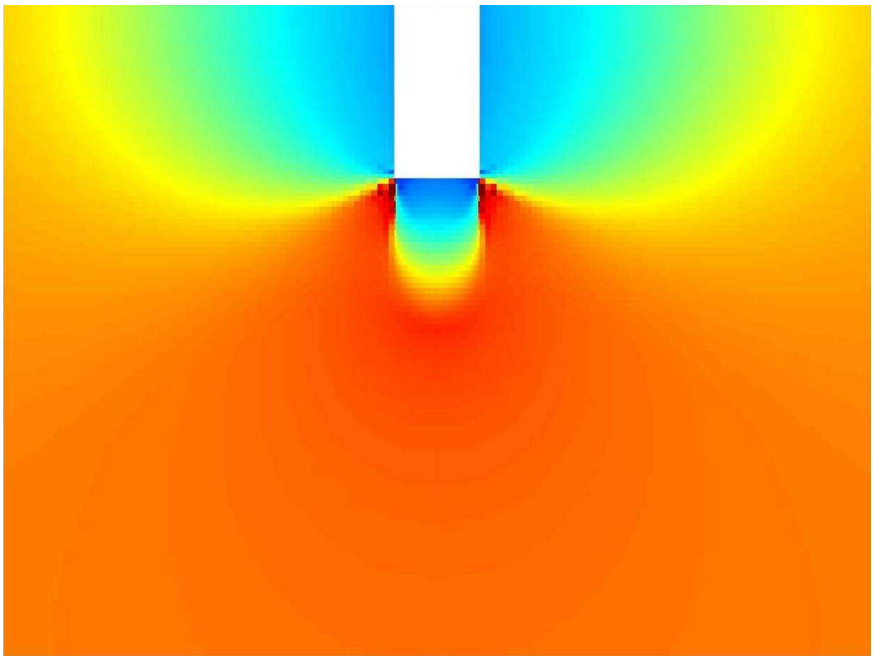

(b)

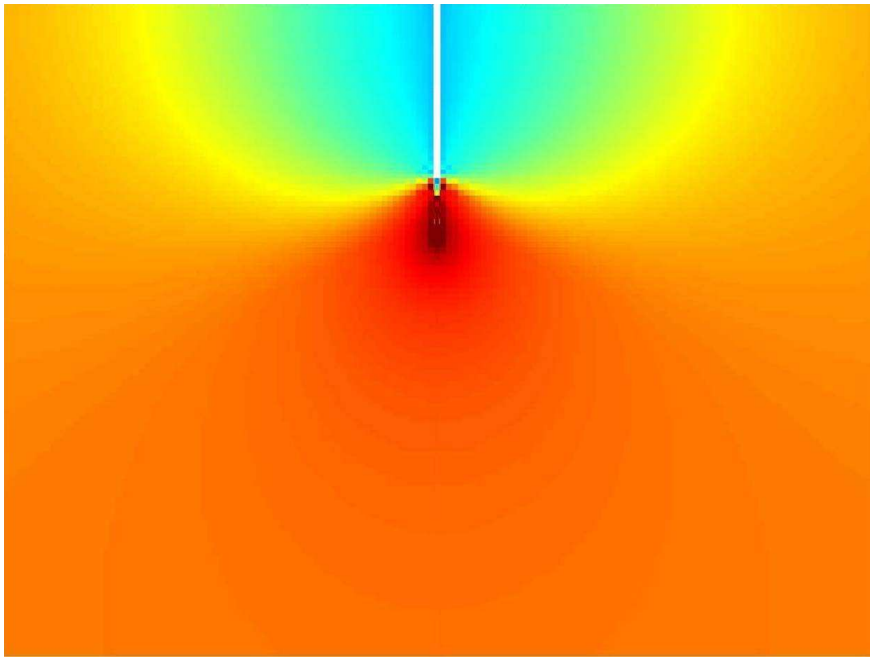

Figure 5.7 Numerical simulation for the effect of the notch sharpness on void ratio (Blue=contraction, red=dilation). (a) A wide notch causes an increase in void ratio oblique to the notch alignment. (b) A narrow notch causes void ratio expansion in the direction of the notch (refer to Table 5.2a for boundary conditions and material properties).

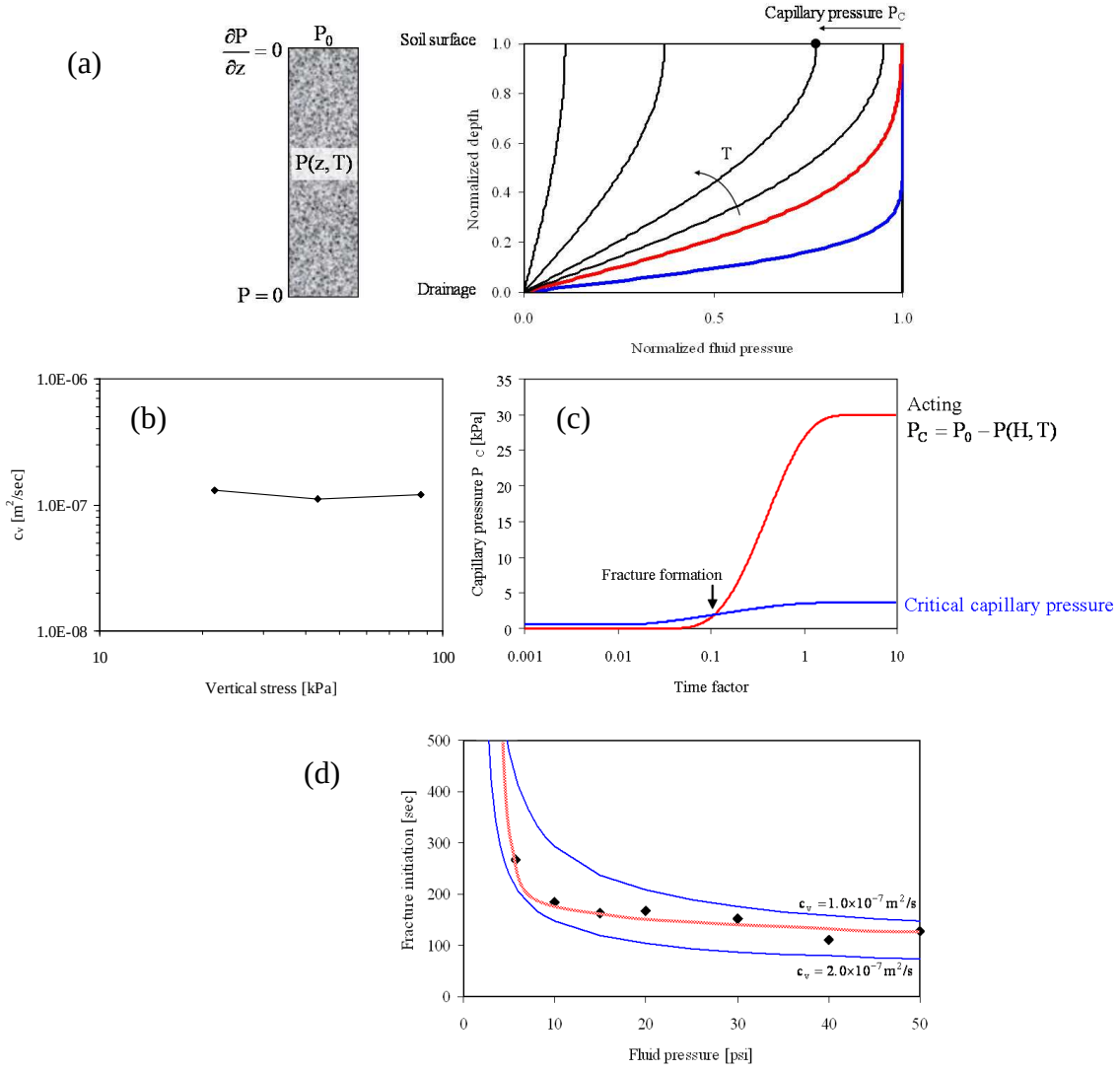

Figure 5.8 Fracture initiation time versus applied pressure - Prediction and observations. (a) Evolution of the host fluid pressure with time and depth. (b) Interval value of diffusion coefficient c_v. (c) Acting and resisting capillary pressure on the soil surface versus time. (d) Estimated and observed fracture initiation time.

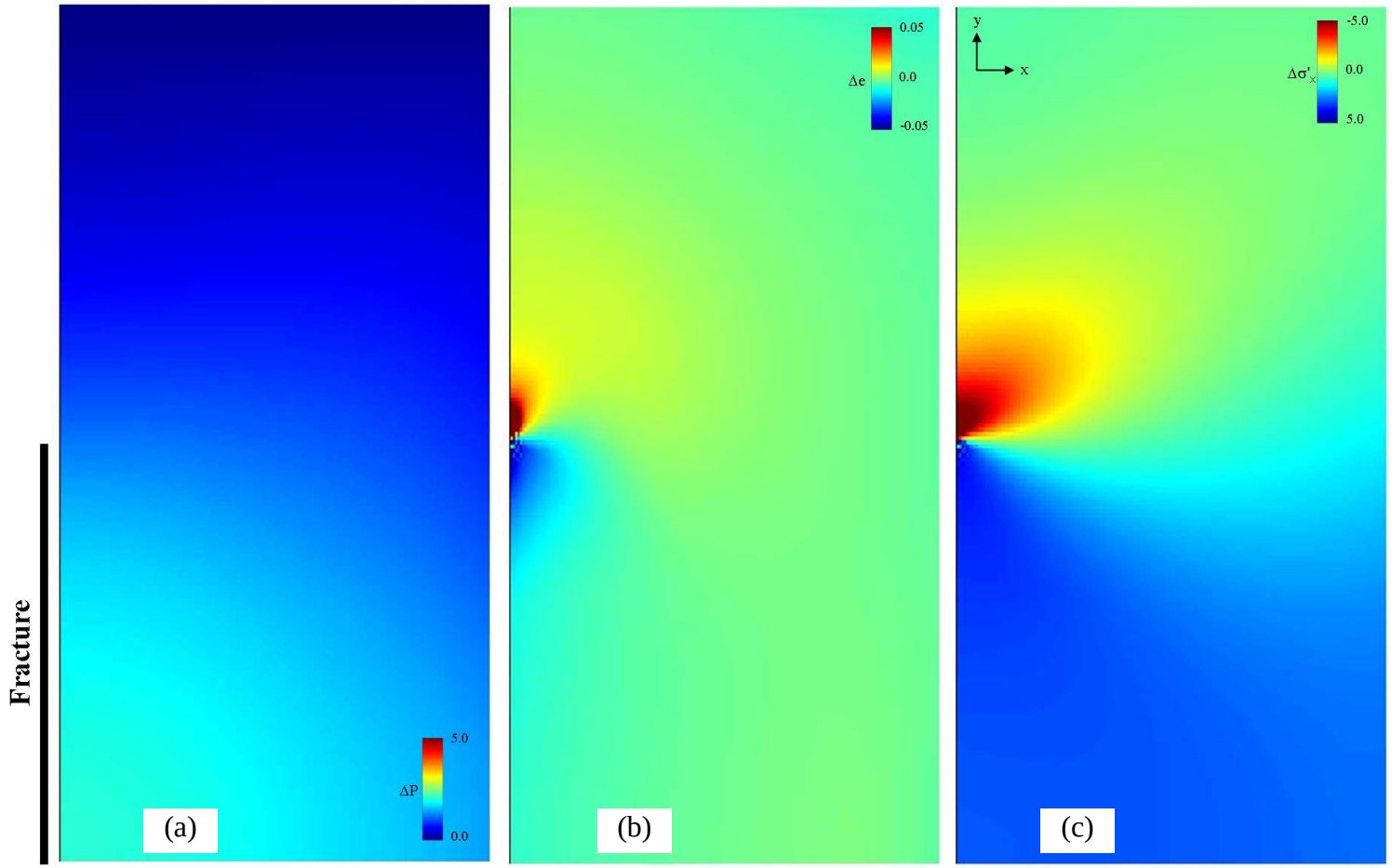

Figure 5.9 Pore pressure, void ratio, and horizontal effective stress distribution during the propagation of a hydraulic fracture driven by the forced invasion of an immiscible fluid (refer to Table 5.2b for boundary conditions and material properties).

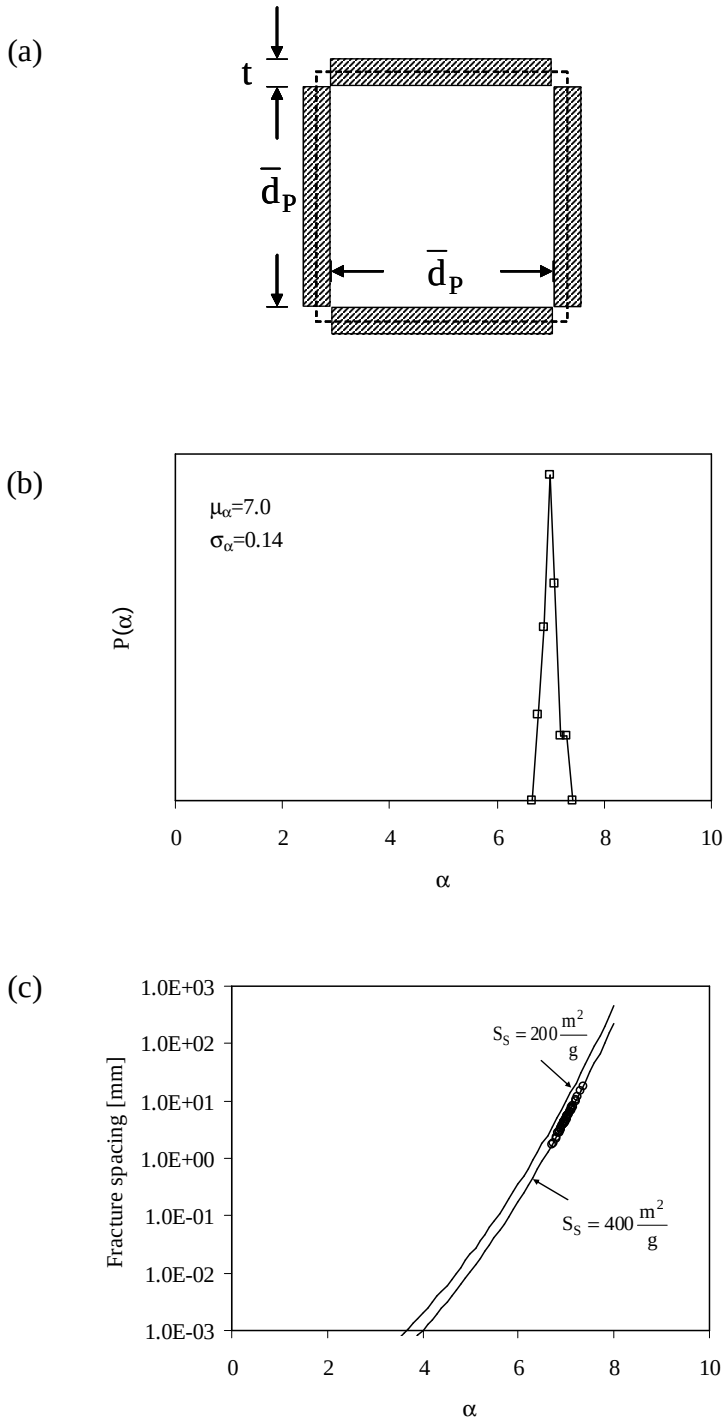

Figure 5.10 Estimation of fracture spacing as a function of the characteristic pore size d* in terms of $\alpha = \log(d^*/\bar{d})/\sigma^*)$. (a) Card-castle arrangement of platy particles, (b) Distribution of α from fracture spacing observation, (c) Fracture spacing as a function of α and soil specific surface S_S.

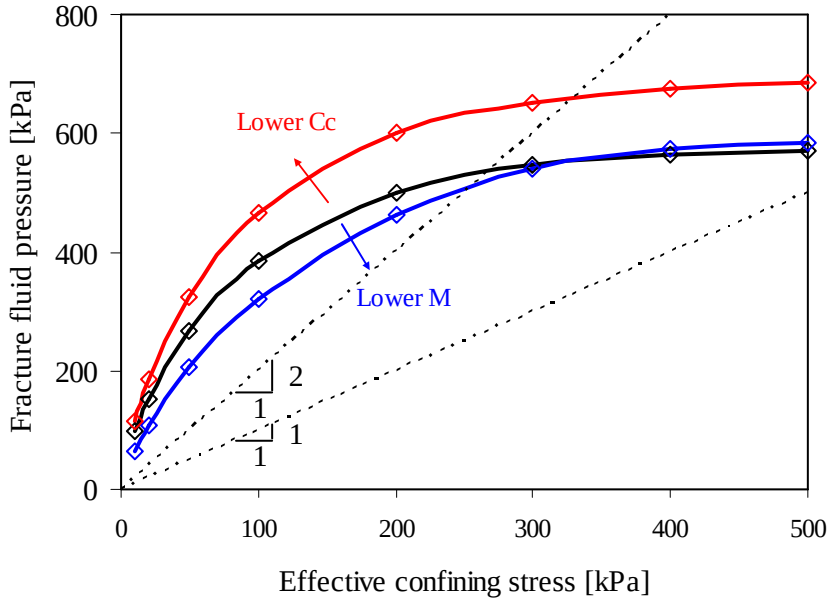

Figure 5.11 Capillary pressure at fracture initiation P_C for boreholes filled with an immiscible fluid. The effects of sediment stiffness and shear strength on P_C are also shown. Borehole radius R=0.1m. Characteristic parameter $\rho T_S S_S / 10^{\alpha\sigma^*}$ =1000kPa.

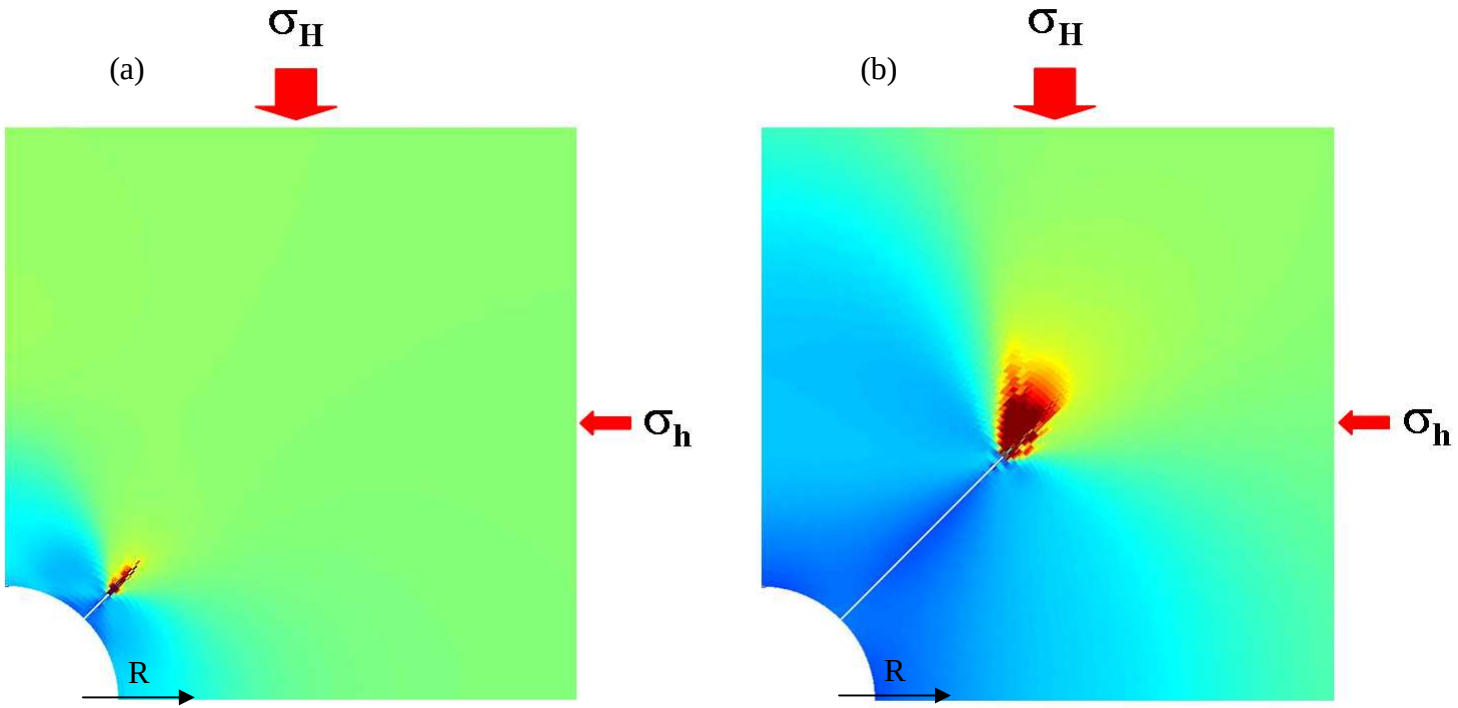

Figure 5.12 Fracture propagation by the forced invasion of an immiscible fluid around a borehole in an anisotropic stress field (Anisotropic far field stress: σ_h/σ_H=0.7). (a) When the fracture tip is at a radial distance r/R=0.3. (b) When the fracture tip at r/R=2.

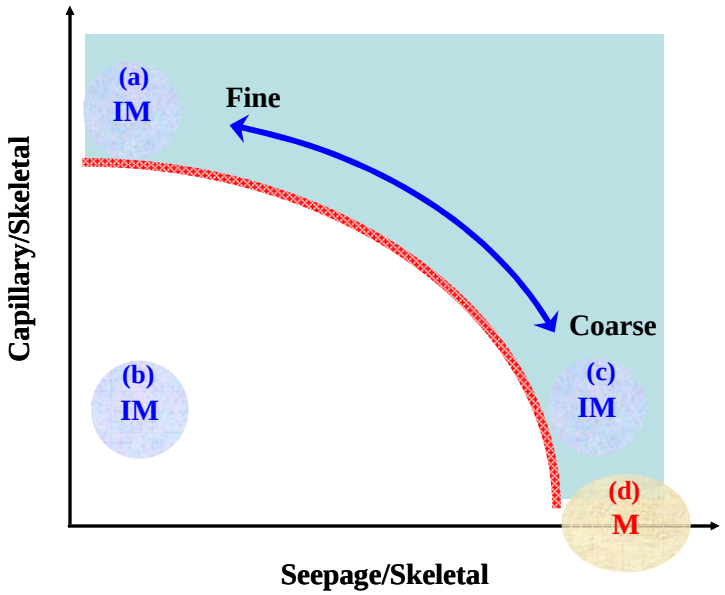

Figure 5.13 Hydraulic fracture regimes depending on fluid and soil type. Balance between capillary $\pi d T_S$, skeletal $\sigma' d^2$, and seepage $3\pi\mu d v_f$ forces: (IM: immiscible fluid; M: miscible fluid). Letters: refer to text.

CHAPTER 6

DISPLACEMENT FIELD IN CONTRACTION DRIVEN FAULTS

6.1 Introduction

The structural analysis of tectonic normal fault systems is widely based on mechanical boundary conditions that faults experience in a regional or local tectonic context in which lateral confinement is locally reduced by lateral extension (e.g., Ramsey and Lisle, 2000). However, not all normal faults can be considered with these classical boundary conditions.

Polygonal faults are a notable exception: they are widely accepted to form during shallow burial, in tectonically passive settings, and under no lateral extension i.e. in strong contradiction to the conditions for tectonic normal faulting (Cartwright and Lonergan, 1996; Cartwright et al., 2003; Nicol et al., 2003). Polygonal faults also represent a major challenge for soil mechanics: they are an expression of shear failure, hence the stress path cannot follow the classical 1-D K_0-stress condition that would prevail under zero-lateral strain conditions. Polygonal faults occur widely in passive continental margin basins where hydrate resources are contained (e.g., Berndt et al., 2003), and occur pervasively in sediments that constitute the major sealing sequences for petroleum accumulations (e.g., Watterson et al., 2000; Stuevold et al., 2003; Cartwright et al., 2007). Therefore, the understanding of polygonal fault systems can be of crucial importance.

In this paper we explore the displacement field on normal faults where the system is laterally confined i.e. the widely agreed boundary condition for polygonal faults. We start by reviewing the genesis of polygonal faults, followed by description of displacement data collected from a wide range of polygonal fault systems. Then, we

present analytical results and numerical simulations of a single contraction-driven normal fault embedded in a granular medium. We build our understanding on previous numerical studies that showed agreement between natural displacement fields and those obtained in models where the elastic strain accumulation results from remote loading of a medium with an embedded shear plane (Eshelby, 1957; Pollard and Segall, 1987; Burgmann et al., 1994; Willemse et al., 1996). As part of the study, we evaluate the material properties that are required to justify the magnitude of displacements typically observed in polygonal fault systems worldwide.

6.2 Genesis of contraction driven faults

The precise mechanism leading to the formation of polygonal faults has been widely debated. Current models include gravitational instability and overturn due to rapid loading (Henriet et al., 1991; Watterson et al., 2000), contraction due to syneresis (Cartwright and Dewhurst, 1998), gravity sliding (Higgs and McClay, 1993), and mineral dissolution during early diagenesis (Shin et al., 2008) (see details in Table 6.1).

A theoretically plausible failure mechanism must satisfy the general observation that polygonal faults begin to form in the first tens of meters of burial (Cartwright et al., 2003; Gay et al., 2004). The recent model proposed by Shin et al., (2008) demonstrates that mineral dissolution at zero lateral strain brings the state of the stress from the K_0-condition to the Coulomb active failure K_a-condition, thus triggering the sediment failure. Shin et al. (2008) also show that shear displacement can localize under these stress conditions when the sediment exhibits post peak strain softening, and listed multiple soil conditions that exhibit this behavior. Low residual friction on polygonal fault planes is one possible mechanism to explain the displacement accumulation, as identified in Goulty (2002, 2008) and Goulty and Swarbrick (2005). However low residual friction does not explain the genesis of faults or the localization of shear into planes, and this

model must also explain the magnitude of the observed displacement fields associated with polygonal faults for the range of physical properties that capture the diversity of sediment types in which polygonal faults are hosted. Furthermore, the deviatoric stress after fault slippage must be compatible with the failure criterion and boundary conditions. The analyses presented herein satisfy equilibrium and compatibility requirements

6.3 Field observations

The displacement distributions in polygonal fault systems are obtained from 3D marine seismic surveys of shallow-buried sedimentary successions in different basins (an example is shown in Figure 6.1a). Data reduction typically involves depth conversion from two way travel time information using interval velocities derived from seismic data processing or from borehole petrophysics. It is assumed that the motion is dominantly dip-slip in these steep fault planes where the fault plane dip is typically $\beta>60°$ (Lonergan et al., 1998; Cartwright et al., 2003; Nelson, 2007).

Characteristic displacement-versus-depth profiles for polygonal faults are presented in Figure 6.1b in the form of throw δ versus depth z plots (herein, throw δ refers to the displacement along the fault plane projected onto the vertical direction). These examples show a maximum throw near the center of the fault, and are similar in many respects to those observed for blind, tectonic normal faults in shallow-buried sedimentary sequences (see Baudon and Cartwright, 2008b for a detailed review). They exhibit the classical end-member forms of C-type or M-type configurations where the displacement maximum has the form of a sharp peak or a broader set of plateau values (Muraoka and Kamata, 1983; Walsh and Watterson, 1988). In typical blind normal faults and polygonal faults, the displacement patterns are generally symmetric with depth, but when a weak layer is present near the base or where a shallow propagating fault approaches the free surface (sediment-water interface), a significant increase in local

displacement gradients is observed (e.g., Watterson et al., 2000; Nicol et al., 2003; Stuevold et al., 2003).

Furthermore, the geometry of polygonal faults is remarkably similar to that of small tectonic normal faults. When observed close to their original position i.e. with their upper tips close to the modern sea bed, they are generally planar (e.g., Figure 6.1a), and exhibit a range of fault plane dips from 50 to 80° (Cartwright et al., 2003). Once buried and inactive, they are passively flattened by vertical compaction, and have much shallower dips, often in the range of 30-50° (Lonergan et al., 1998; Stuevold et al., 2003).

The regions surrounding individual polygonal faults show evidence of local strain accumulation that closely matches the theoretically predicted near-field strain for blind normal faults (Barnett et al., 1987). A good example of this strain distribution is seen in Figure 6.1a, where stratal reflections in the hangingwall are deflected below the regional datum. The zone of near-field strain varies from fault to fault, but its lateral extent away from the fault in both hangingwall and footwall locations is usually between 10-50% of the fault height. The strain is manifested in stratal rotation and deflections below and above regional, and also in localized thinning, particularly in the lower hangingwall quadrant of the fault (c.f., Barnett et al., 1987, their Figure 1c). The magnitude of these near field strains reaches a maximum close to the fault plane where it effectively equals the strains measured parallel to the fault in the presumed slip direction (the dipslip condition of Walsh and Watterson, 1988 and Ramsey and Lisle, 2000).

Tectonic normal faults are widely considered to follow a simple scaling relationship between maximum displacement and maximum dimension (Cowie and Scholz, 1992; Schultz et al., 2006). For comparison, we plot the maximum throw δ versus fault height H in Figure 6.2 for a collection of 629 faults in polygonal systems worldwide (Note: height H is measured in the vertical direction). Data scatter is due in part due to blocking during lateral propagation (Nicol et al., 2003). Most of the data are bound within $\delta/H=0.045\pm0.016$. These are surprisingly large displacements for systems that

have not experienced extension in their basal planes, and the δ/H values are much larger than for most tectonic normal faults (as compared to trends in Cowie and Scholz, 1992 at an effective stress $\sigma' < 40$MPa). The following sections attempt to model the displacement distribution observed in polygonal fault systems.

6.4 Analyses

Our analysis of strain accumulation adopts a simple geometrical configuration reminiscent of the earlier studies, but we select material parameters and boundary conditions that apply to granular materials such as soils or uncemented sediments. Most importantly, our remote driving stress is gravitational loading under zero-lateral strain conditions, in order to replicate those suggested in recent models for polygonal fault growth (Goulty, 2008). The approach is two dimensional and it does not capture the full complexity of lateral propagation effects of a fully three-dimensional array of normal faults that typifies polygonal fault systems. Nevertheless, these limitations do not invalidate our primary conclusions regarding first-order estimates of the material properties necessary to justify the observed field strain in polygonal fault systems.

Studies of the dip of normal faults in natural systems and shear localization in sediments suggest that the fault orientation β is dictated by the peak friction angle ϕ (Walsh and Watterson, 1988; review in Vermeer, 1990). Therefore, our analyses and simulations start by presuming a shear plane at $\beta = 45° + \phi/2$.

The stress redistribution caused by a residual friction angle $\phi_r < \phi$ acting on a fault at orientation $\beta = 45° + \phi/2$ leads to a new horizontal effective stress σ'_{hr} that is higher than the initial horizontal stress $\sigma'_{ho} = K_0 \sigma'_z$. We can relate σ'_{hr} to the vertical effective stress so that $\sigma'_{hr} = K_r \sigma'_z$. Equilibrium dictates (Figure 6.3a and 6.3b):

$$K_r = \frac{\cos(\beta)\sin(\beta - \phi_r)}{\sin(\phi_r) + \cos(\beta)\sin(\beta - \phi_r)} \tag{6.1}$$

The horizontal stress change from the initial K_0-state to the final residual stress state $\Delta\sigma'_h=(K_r-K_0)\sigma'_z$ produces a contractive strain ε_h in the horizontal direction normal to the strike of the fault that can be estimated as:

$$\varepsilon_h = \frac{\Delta\sigma'_h}{E} = (K_r - K_0)\frac{\sigma'_z}{E} \tag{6.2}$$

The effective horizontal length L(z) for strain accumulation away from the fault plane relates horizontal strain to horizontal displacement $u_h(z)$ as $u_h=\varepsilon_h/L$. We assume a parabolic function with depth $L(z)=z(1-z/H)$, so that there is zero displacement at ends and the maximum length of influence is L(z)=H/4 on each side of the fault at a depth z=H/2, i.e., the effective zone for horizontal displacement around the fault is about half of fault height H (Figure 6.3c - Barnett, et al., 1987).

An associated vertical displacement $u_z=u_h\tan\beta$ must take place to satisfy compatibility. The parabolic displacement field (in agreement with field trends in Figure 6.1b) is evaluated with the displacement constraints at the top and bottom of the fault, $u_z(z)= \varepsilon_h \tan\beta\, z(1-z/H)$. The maximum throw δ along the fault is twice the relative displacement at the mid-height of the fault, $\delta=2u_z(H/2)$; then

$$u_z(H/2) = \frac{H}{4}\varepsilon_h \tan(\beta) = \frac{(K_r - K_0)\tan(\beta)}{4}\frac{\sigma'_z}{E}H \tag{6.3}$$

Finally, the normalized throw δ/H becomes

$$\frac{\delta}{H} = \frac{(K_r - K_0)\tan(\beta)}{2}\frac{\sigma'_z}{E} \tag{6.4}$$

This order-of-magnitude expression predicts that the normalized throw δ/H increases linearly with the stress-to-stiffness ratio σ'_z/E and the normalized stress change K_r-K_0.

In the case of a surface fault, the normalized throw can be estimated using a fictitious height 2H, where H is the real height of the surface fault.

Since the horizontal contractive strain at the bottom of the hanging wall is constrained by the surrounding medium, the volumetric strain around the tip of the fault is dominated by the vertical strain:

$$\varepsilon_v \approx \varepsilon_z = \left.\frac{\partial u(z)}{\partial z}\right|_{z=0} = \varepsilon_h \tan(\beta) \qquad (6.5)$$

6.5 Numerical study

Numerical simulations are conducted to verify the previous analytical estimates and to gain additional insight into fault displacements and strain fields. In these simulations, we represent the sediment using the Drucker-Prager model where the Coulomb-type strength criterion is linearly proportional to the effective confining stress, i.e., we explicitly avoid cohesive strength so that effective stress dependent material parameters can be adopted particularly in the case of shallow faults. Constitutive model parameters and numerical simulation details including boundary conditions are summarized in Table 6.2.

Two stiffness models are considered in this study to replicate likely end member propagation modes for polygonal faults. The first model assumes that the fault height is much shorter than the burial depth, i.e., a deep blind fault, and the stiffness is considered constant in the region under study. This is intended to simulate the possible situation where polygonal faults first propagate as blind faults so that their tiplines do not intersect with another fault or feel the effects of a free surface. The second model applies to near-surface faults and the stiffness at depth z is assumed to be linearly dependent on the mean stress at that depth (linearity with effective stress applies to large strain processes as those modeled here – Terzaghi and Peck, 1967). This second case is intended to simulate the

case where polygonal faults initiate within a few tens of meters of burial, and propagate to the free surface, where they subsequently behave as small syn-sedimentary faults, displacing the sediment-water interface (see examples in Stuevold et al., 2003). Results for both end-members are presented below together with a modification to incorporate addition of new load due to continued sedimentation during fault propagation.

6.5.1 Case 1 - Constant stiffness (deep, blind faults)

Predicted volumetric strains and throw are shown in Figure 6.4. The volumetric strain ε_v is normalized by the vertical load q at the burial depth and the constant sediment stiffness E. Likewise, throw δ is normalized by fault height H. Results show a crude bilateral symmetry with upper footwall and lower hangingwall quadrants being regions of contractile straining, and upper hangingwall and lower footwall regions experiencing unloading and expansion. This trend equates to deflections of originally horizontal stratal surfaces from their regional datum (Figure 6.1b). The volumetric strain field shown in Figure 6.4a bears a striking resemblance to strain fields published in previous studies (Barnett et al., 1987; Pollard and Segall, 1987).

The normalized throw $(\delta/H)(E/q)$ overlaps for all cases simulated with different E/q values in this study (E/q=0.1, 1, 10, 100). In other words, the maximum throw δ in a given fault is directly proportional to the fault height H, the overburden stress q and inversely proportional to the sediment stiffness E (Figure 6.4). This observation confirms the possibility of crude scaling between δ and H for polygonal faults as discussed above (Equation 6.3). Once again, we find that although all models show strain distributions that match those associated with natural polygonal faults, small stiffness is required to match the observed natural strain magnitudes.

The effect of peak friction angle, fault orientation and residual friction angle on throw and maximum volumetric strains around the fault are explored in Figures 6.4b and 6.5. It can be observed that the steeper faults with higher peak friction angle lead to

higher normalized throws at the same residual friction angle (Figure 6.5a). The magnitude of the throws with the peak friction is well matched with the theoretical solution (Equation 6.3), except for the sediments with very high peak friction angle ($\phi \geq 50°$) where the numerical solution captures geometric constraints not considered in the analytical solution: eventually, a fault at right angle $\beta=90°$ would have no slippage or horizontal stress change. The maximum volumetric strain values of the four quadrant regions are reasonably well matched by the analytical approximation (Equation 6.4), except at very high peak friction angle (Figure 6.5b).

The maximum throw and the volumetric strain are directly related by the residual friction angle, because it determines the stress change the medium will experience after fault propagation (Equation 6.3). The decrease in friction angle from the peak ϕ to the residual ϕ_r is strongly related with mineralogy: ϕ_r in kaonite > illinte > montmorrilonite. Furthermore, the volume fraction of platy clay particles must exceed 10~15% for a significant strain softening behavior to develop (Kenney, 1959; Olson, 1974; Lupini, et al., 1981; Skempton, 1985; Mesri and Cepedadiaz, 1986). The effect of the residual friction on the displacement field, the magnitude of the normalized throw, and the volumetric strain is reported in Figures 6.4b, 6.5a and 6.5c. It can be observed that both the normalized throw and the volumetric strain increase as the residual friction decreases. The volumetric strain of the four quadrant regions retains the near bilateral symmetry (Figure 6.5b).

6.5.2 Case 2 - Proximity to a free surface

These simulations are conducted with the second stiffness model E/σ'_m=constant to approximate the inherent stress-dependent sediment stiffness at large strains. Proximity to the free surface markedly affects the strain pattern, particularly as the normalized burial depth $e_1/H<0.5$ (sketch in Table 6.1). When the fault intersects the surface, contractile strains develop along the entire hangingwall, and only dilatant strains take

place in the lower footwall. Furthermore, interaction of the fault with the upper free surface significantly modifies the geometry of displacements in the near-field to the fault, leads to greater asymmetry in fault displacements, and causes an increase –albeit minor- in the maximum throw (Figure 6.6). This pattern of displacement variation is similar in many respects to that observed for small synsedimentary normal faults (e.g., Childs et al., 2003; Baudon and Cartwright, 2008a), although exact comparison is difficult because the timing for the transition from blind propagation to free-surface intersection is unknown in the natural examples.

6.5.3 Case 3 - Additional loading after fault formation

Additional sedimentation after fault formation causes further displacement along the fault in both blind and near surface faults. The additional stress applied $\Delta\sigma'_z$ is normalized by the initial vertical stress at the base of the modeled region σ'_{zo} in each case, $s=\Delta\sigma'_z / \sigma'_{zo}$, in other words, a value of s=1 implies doubling the burial depth at the base. Results summarized in Figure 6.7 show the pronounced increase in fault displacement, particularly for the near surface faults. This indicates that additional gravitational loading onto pre-existing faults could be sufficient to maintain active slip conditions, provided that the requisite material properties apply for the granular medium and fault plane, respectively. The corollary of this is that cessation of additional sedimentation should cause the fault to become inactive, unless added complexity such as further changes in material properties or secondary consolidation (creep) are considered explicitly.

6.6. Discussion

This study has attempted to simulate natural strain accumulation in polygonal faults, and to determine the relative relevance of controlling factors with respect to the strain distribution and magnitude. Results obtained for the end member cases of blind and

surface faults, show that continued slip on a normal fault can occur entirely due to vertical loading, even though there is no net extension. This fundamentally differs from classical views of normal fault growth in which a driving stress is required to maintain conditions of fault activity, and where that drive involves a true tectonic extension. This alternative growth mechanism to normal faulting is therefore entirely compatible with the boundary kinematic conditions for polygonal fault growth in many natural settings, as first suggested by Goulty (2002). However, the strain magnitude observed in natural polygonal fault systems is sufficiently large, that both the theoretical and modeling approaches undertaken here suggest that a very low value of stiffness is implied, along with a requirement for strain softening behavior. The question therefore arising, is under what conditions can these physical property requirements be met such that the typical strains can thus accumulate? The following analysis demonstrates that strain softening and low stiffnesses are most likely to be encountered as the natural response of sediments that have experienced mineral dissolution.

6.6.1. Strain softening after dissolution - Effective stress analysis

Analytical and numerical studies presented earlier assumed a low residual friction angle. Further insight is gained by anticipating the evolution of dissolution and failure in the four main dimensions that capture sediment behavior (Figure 6.8): effective confinement $\sigma'=(\sigma'_1+\sigma'_3)/2$ or mean stress p', shear stress $\tau=(\sigma'_1-\sigma'_3)/2$ or deviatoric stress q, axial strain εa, and void ratio e. Note that p'-q define the apex of the Mohr circle, and that the axial strain is determined by volume change in one dimensional loading $\varepsilon_a=-\Delta e/(1+e_0)$. Two types of sediment responses experiencing mineral dissolution are plotted in Figure 6.8. We first consider starting with the drained failure case (Figure 6.8a – Interpretation based on Shin et al., 2008, and Shin and Santamarina, 2009):

- Sedimentation: The sediment follows the normally consolidated line NCL to reach point ① where the void ratio is in equilibrium with the overburden stress, and the initial horizontal stress is $\sigma'_{ho}=K_0\sigma'_z$ where $K_0\approx 1-\sin\phi$ according to Jaky's equation (Jaky, 1944).

- Diagenesis: Dissolution increases the void ratio to point ② and lowers the horizontal stress to the failure condition $\sigma'_h\approx K_a\sigma'_z$ where $K_a=\tan^2(45°-\phi/2)$. Note that the soil mass is at the verge of failure in τ-σ', yet away from the critical state line CSL in the e-σ' space.

- Drained failure: The sediment shears and collapses, and often returns to a state similar to K_0 (path from ② to ③). The void ratio may end near the NCL or even the CSL lines (point ③).

We next consider a second case, and explore the undrained shear and collapse of the sediment following dissolution (Figure 6.8b). Points ① and ② are the same as in the previous case, then:

- Undrained failure: The undrained shear and collapse occurs at constant volume, and the sediment evolves towards the critical state line at constant void ratio, as shown by point ③ in the e-σ' quadrant. There is a high increase in pore pressure due to the high porosity in partially dissolved sediments prior to failure. The effective stress σ' decreases and so does the strength according to the Coulomb criterion $\tau_{ult}=\sigma'\tan\phi$, therefore, there is pronounced strain softening.

- Pressure diffusion: After shear, the excess pore pressure dissipates with time, and the sediment evolves towards a reconsolidated stress probably near the normally consolidated line NCL (dotted lines beyond point ③).

Note that post failure strain softening is observed in both cases (trajectories from points ② to ③), and there is no need to involve low residual friction angle ϕ_r to justify shear localization. In any case, low ϕ_r will contribute to localization and strain accumulation.

It is also important to recognize that the sediment at points ① and ② may be profoundly different. For example, fresh volcanic ash is made of silt and sand size amorphous silica and packs at void ratio e=0.8-to-1.7, yet, diagenesis may change it into a clay sediment made of halloysite, allophane and imogolite packed at a high void ratio e=2-to-7 [Herrera et al., 2007].

6.6.2 Low equivalent stiffness

The ratio of normalized throw δ/H to normalized stiffness E/σ' in Equation 6.3 is a function of ϕ and ϕ_r. For a wide range of parameters ($30° \leq \phi \leq 40°$ and $5° \leq \phi_r \leq 15°$), the normalized stiffness must be between $1.5 < E/\sigma'_z < 10$ to match field data $\delta/H \approx 0.045$. This is a surprisingly low number in sediments where E/σ' values range from $E/\sigma' \sim 103$ for small strains to $E/\sigma' \sim 40$ at large strains (Santamarina, et al., 2001). In general, permutations of the main controlling parameters such as orientation, burial depth, and residual shear strength cannot match the strain magnitude observed on natural polygonal faults if typical values of sediment stiffness are used.

Indeed, our results strongly imply that gravitational loading cannot by itself account for the significant deformations observed in polygonal faults, even for very low residual friction angles. Moreover, these extraordinary normal faults often occur on layers with zero basal extension, therefore fault displacements cannot be the result of extension and we cannot appeal to regional extensional kinematics to solve the strain magnitude problem (Cartwright and Lonergan, 1996).

To resolve this difficulty, we consider the processes of dissolution proposed as a triggering mechanism by Shin et al. (2008) and examine whether it can also account for the strain observed in natural systems. Dissolution produces a sediment of high porosity prior to shear, as anticipated in Figure 6.8 and observed in experimental results with sand and salt mixtures and in discrete element simulations with mixtures of rigid and vanishing grains (Shin et al., 2008; Shin and Santamarina, 2009). Consider a sediment with void ratio e* after dissolution but prior to shear; if no global volumetric deformation takes place during dissolution, $e^* = (e_0+\alpha)/(1-\alpha)$ where e_0 is the initial void ratio prior to dissolution and α the dissolved volume fraction. If the void ratio after shear is consistent with either the NCL or CLS lines (Figure 6.8a), the normalized equivalent skeletal compressibility E_{eq}/σ' that governs volume contraction at fault formation can be estimated to a first approximation as

$$\frac{k_r - k_a}{\alpha} > \frac{E_{eq}}{\sigma'_z} > \frac{k_r - k_a}{\alpha + 0.3(1-\alpha)C_c/(1+e_0)} \qquad (6.6)$$

This expression predicts that the normalized stiffness is about $E_{eq}/\sigma' \approx$ 1.5-to-6 during shearing in sediments that have experienced α=10% dissolution.

The argument presented above has a further fundamental implication: it suggests that the strain accumulates in a material in which the stiffness is low to start, or is lowered incrementally as a function of time. This diagenetically 'coupled' model for physical property evolution and stress development then offers an explanation for the fundamental and defining characteristic of polygonal fault systems, namely their polygonal planform geometry. To develop a truly polygonal system with the intersection relationships that are universally observed (Nicol et al., 2003), it is clearly necessary that some faults nucleate and propagate earlier than others, and indeed the displacement transfer that occurs at intersections testifies to this simple principle (Stuevold et al., 2003). It follows from this that as one fault is reaching almost full propagation, and

accumulating strain accordingly, others nearby are only just initiating. This temporal evolution of the network thus matches a driving mechanism that has an inbuilt time dependence, as would be inevitable with dissolution-based diagenesis.

6.7 Conclusions

The genetic mechanism of polygonal fault systems has been extensively debated mainly due to the boundary constraints for fault mobilization, unlike tectonic normal faults.

Mineral dissolution drives the in-situ stress state from the initial at-rest K_0 condition to Coulomb-failure K_a condition, the sediment becomes inherently strain softening, conditions for strain localization are satisfied leading to fault formation, and the equivalent stiffness becomes sufficiently low to justify observed displacement fields. Indeed, displacements measured in polygonal fault systems can only be explained if the whole medium has stiffness much lower than the stiffness for standard sedimentary conditions.

The throw δ in contraction driven shear faults is proportional to the fault height H, and the initial effective stress in the sediment σ, and inversely proportional to the sediment stiffness E and the residual friction angle ϕ_r (or the post-peak strength).

Proximity to an upper free boundary biases the displacement pattern (larger displacements near the boundary), but it does not have a pronounced impact on the magnitude of displacements during fault formation. Additional surface loading after formation causes further fault displacement; the effect is more pronounced when faults are closer to the upper free boundary. Thus additional displacement may take place once a fault has formed by further decrease in ϕ_r (unlikely), further dissolution (i.e., decrease in E for the purpose of modeling), or additional surface loading.

We anticipate that the ratio E/σ and the residual strength are directly related to the diagenetic evolution of the sediment and its current composition (mineralogy and fabric). Therefore, measured δ/H values in polygonal faults around the world may cluster once the sediment composition is taken into consideration.

Table 6.1 Common characteristics of observed polygonal fault systems

Location	Age	Lithology	Boundary lithology	Fault slope (deg)	Fault trace(m)	Throw (m)	Extension strain (%)	Depositional environment	Main observation	Reference
Southern North Sea	Palaeogene	Smectite-rich Clay	Sand (B)	45~80	(20)	several ~10		Marine slope and basin floor	First recognition	Henriet et al. (1991)
North Sea basin	Eocene to Oligocene	Smectite rich Claystone	Claystone/Sandstone	~ 50	100~1000	50~100	~ 13	Marine slope and basin floor	3D systematic feature	Cartwright (1994)
Lake Hope	Lower Cretaceous	Mudstone	Sandstone& siltstone(B)	50~55	~ 350	10~80	2.6	Marine sediment	Density inversion	Watterson et.al. (2000)
Lower Congo basin	Upper Miocene to lower Quaternary	Mudstone/biosiliceous ooze	Mudstone	53-77 (unpub)	(700)	5~20	<5 (unpub)	Onlapping slope wedge	Pockmarks and furrows on the seafloor / relationship between fault network and sediment loading	Gay et al. (2004)
Canadian Atlantic margin	Cenozoic / upper Cretaceous	Mudrock / chalk	Coarse grain (B)	50~70	~ 386	~ 26		Marine shelf and slope	Intersection between polygonal fault and tectonic faults	Hansen et al. (2004)
Mid Norwegian Margin	Eocene-Miocene	Fine grained, hemi-pelagic Biosiliceous mudstone	mudstone	55-75 (unpub)		20~40ms		Slope	Flow path for gas hydrate / opal A to opal CT diagenesis	Berndt et al. (2004)
Lake superior	Early Holocene	Glacio-lacustrine clay	Red varved clay(B)		(<30)	<1m		Lake floor	Pore fluid is low salinity	Cartwright et al. (2004)
Blake Ridge	Miocene	Biosiliceous mudstone/ Calcareous mudstone				<30m		Slope contourite	Associated with gas migration	Hornbach et al. Holbrook et al.
Rockall Basin	Oligo-Miocene	Smectitic claystone/biosiliceous mudstone		>50	300-1500	5-50		Slope		Cartwright and Dewhurst (1998)

Table 6.2 Numerical study: Model, material parameters, and boundary conditions

Geometry and boundary conditions

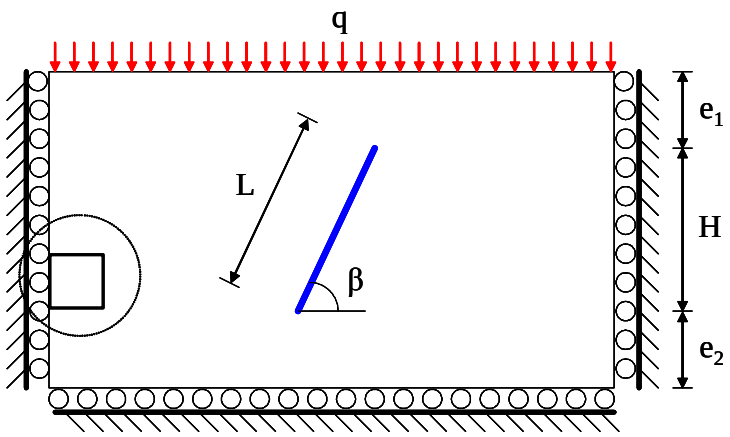

Element type

- Element type: 8 nodes, 2D plane strain
- Number of elements: 10,300
- No friction against boundaries
- Overburden stress on the top boundary

- q for Fig. 6.4, 6.5 and 6.7a
- Zero for Fig. 6.6 and Fig. 6.7b, 6.7c, and 6.7d

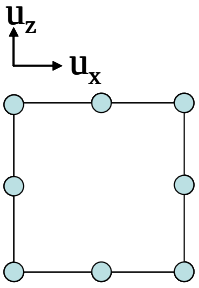

Material properties

- Constitutive model: Drucker-Prager model with non-associated flow rule
- Soil strength: Coulomb $\tau=\sigma' \tan \phi$, peak and residual friction angles ϕ and ϕ_r, zero cohesion.
- Stiffness models
  - (1) E=constant, Poisson's ratio ν=0.3 in Fig. 6.4, 6.5, and 6.7a.
  - (2) E/σ'_m=constant, Poisson's ratio ν=0.3 in Fig. 6.6, 6.7b, 6.7c, and 6.7d, where $\sigma'_m=(\sigma'_1+\sigma'_2+\sigma'_3)/3$.
- Initial state of stress $K_0= \sigma'_x/\sigma'_z$ =1-sin ϕ.
- Fracture orientation $\beta=45°+\phi/2$.

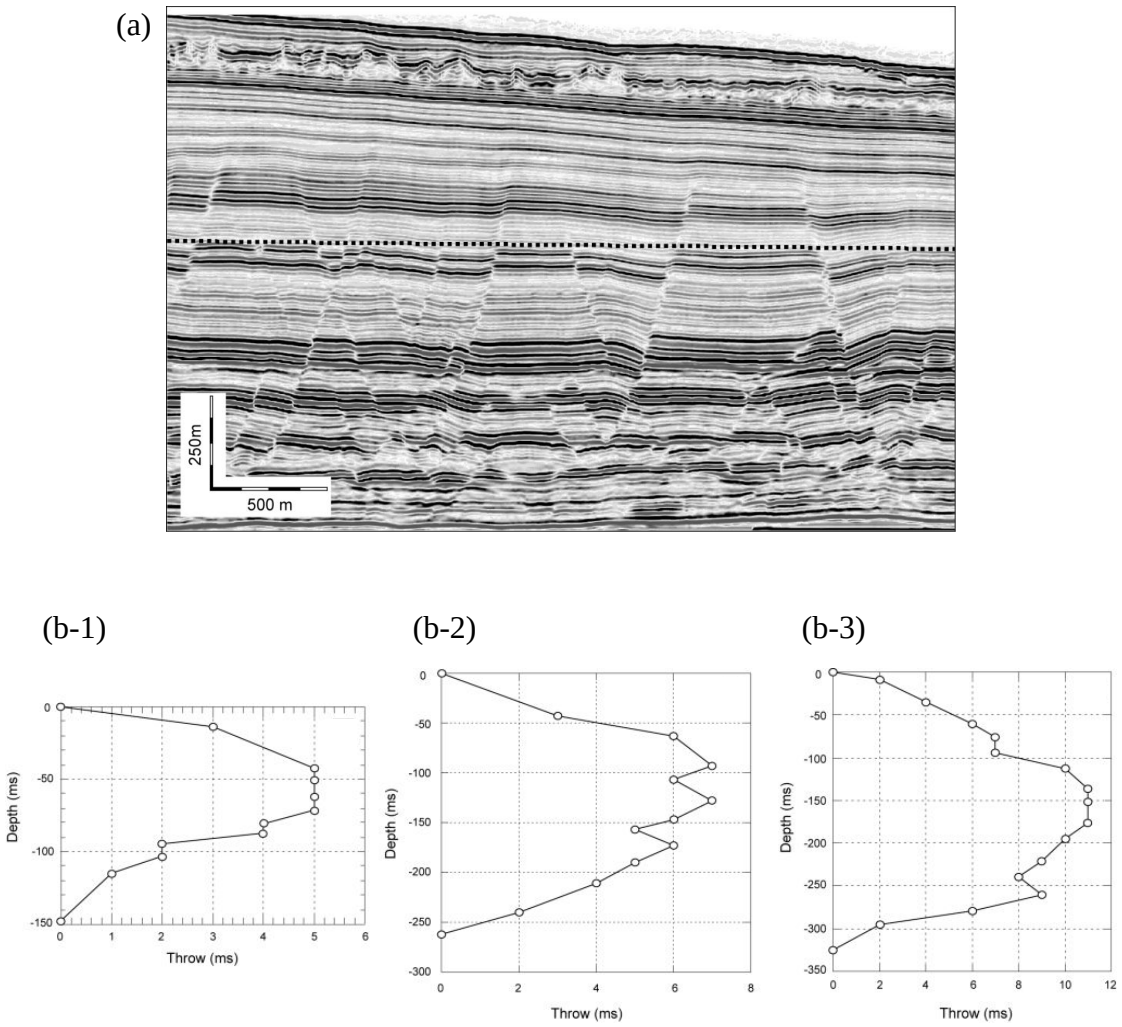

Figure 6.1 Polygonal fault system and its characteristic displacement-versus-depth profiles. (a) Seismic profile showing the typical geometry of polygonal faults in clay-rich sediments offshore Norway. The seabed is at the top of the image. The faults have maximum throw values close to the centers of the fault planes. Many of the faults exhibit small-scale folding close to the fault planes. The dotted line is a pre-faulting datum to allow the relative displacement across faults to be assessed. (b) Plots of throw (in milliseconds two way travel time) versus depth (in milliseconds; Note: 1ms is approximately 1m) for three faults from a polygonal fault system offshore west Africa. These plots all exhibit a central maximum and are hybrid between the end member C and M types of Muraoka and Kamata (1983).

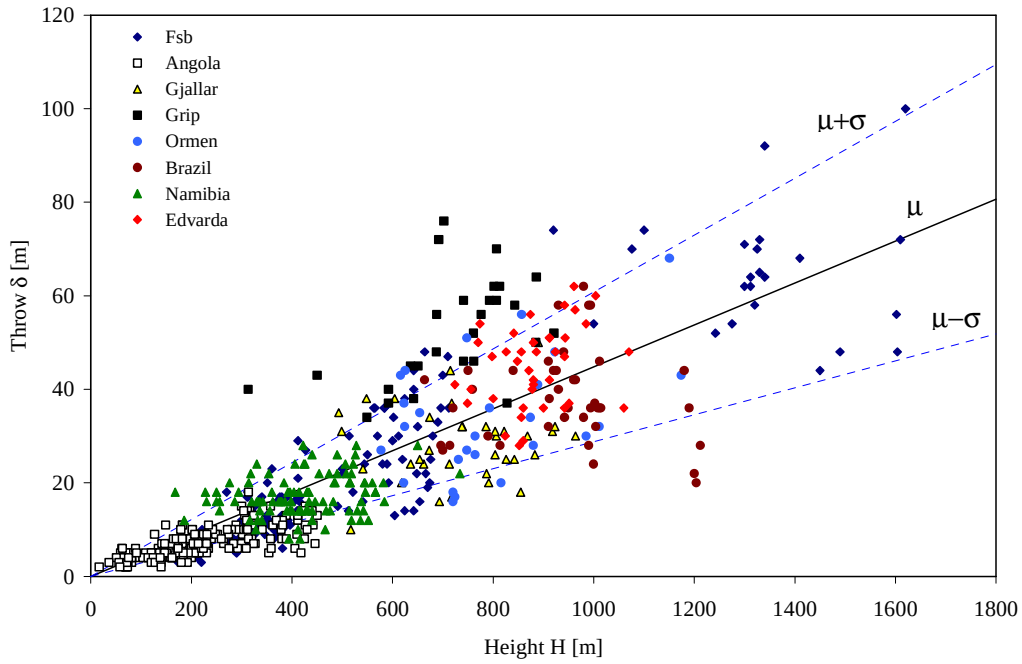

Figure 6.2 Height versus maximum throw for 629 faults from nine separate polygonal fault systems worldwide. Polygonal faults in these nine areas have not been deeply buried and their upper tips are within 20-300m of the surface. Most of the data are bounded within $\delta/H=0.045\pm0.016$.

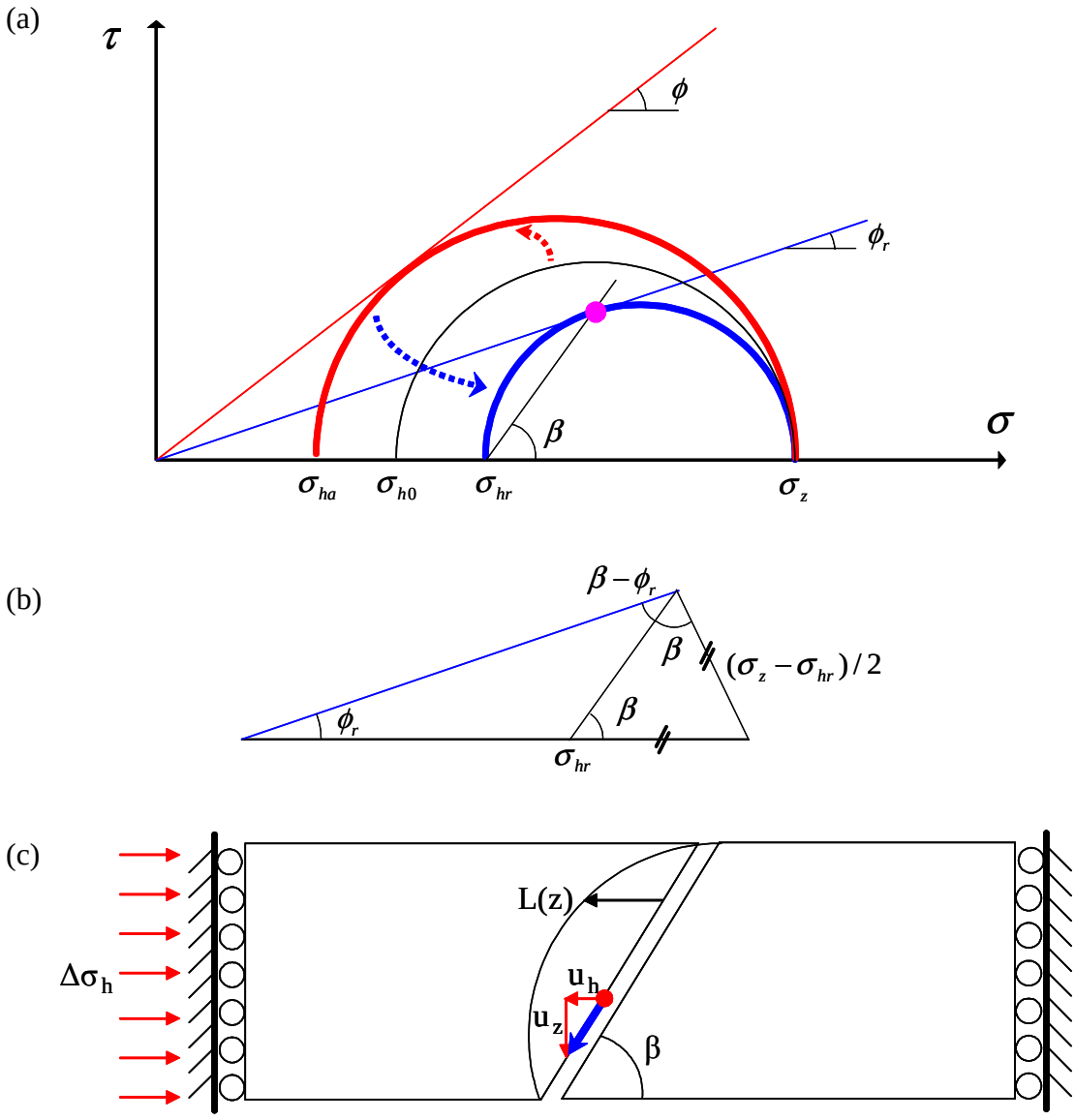

Figure 6.3 Equilibrium and compatibility analyses. (a) Stress path in the Mohr-Coulomb space. (b) Equilibrium at residual stress state. (c) Effective zone L(z) for horizontal strain accumulation and relative displacement compatibility along the fault slope.

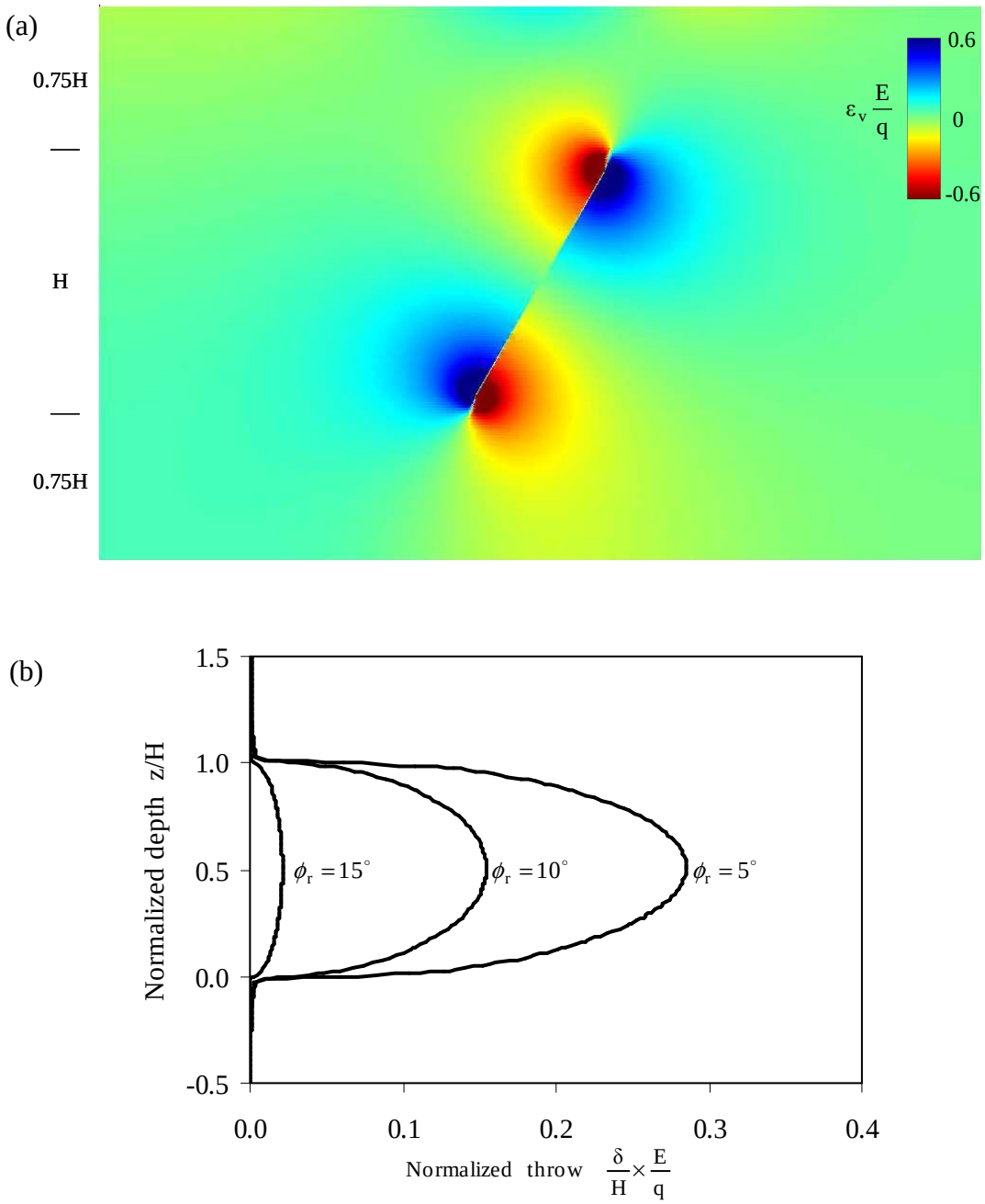

Figure 6.4 Strain and displacement field after fault slippage for a medium with constant stiffness E=constant (resembles deep burial condition). (a) Normalized volumetric strain $\varepsilon_v E/q$ (Contractive is positive - blue). (b) Normalized throw along the fault length for different residual friction angles. Model parameters: sediment friction angles ϕ=30°, ϕ_r=5°, initial state of stress K_0=1-sinϕ=0.5, fracture orientation β=45°+ϕ/2=60°. Distance to boundaries e_1=e_2=0.75H (refer to Table 6.1 for model details).

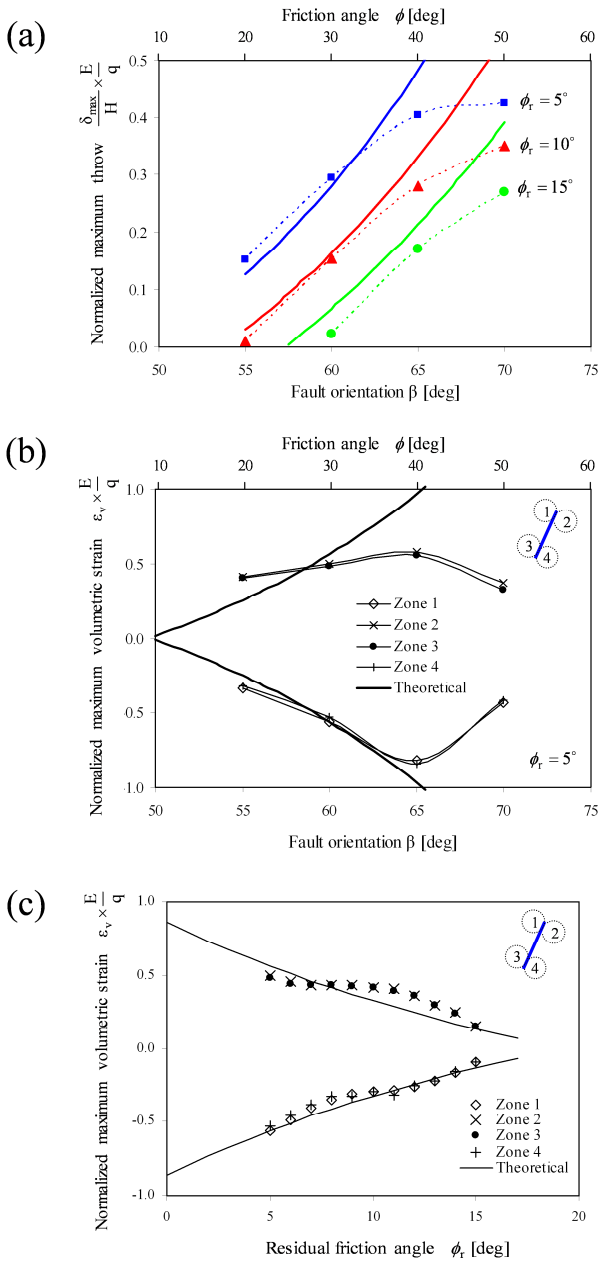

Figure 6.5 Effect of peak and residual friction on the strain and displacement field in a sediment of constant stiffness, E=constant (deep fault). (a) Maximum throw for different peak and residual friction angles. (b) Maximum volumetric strains near the fault ends for different peak friction angles (see insert). (c) Volumetric strains near the fault ends as a function of residual friction angle. Model parameters: initial state of stress K_0=1-sinϕ, fracture orientation β=45°+ϕ/2. Distance to boundaries e_1=e_2=0.75H - refer to Table 6.1 for model details.

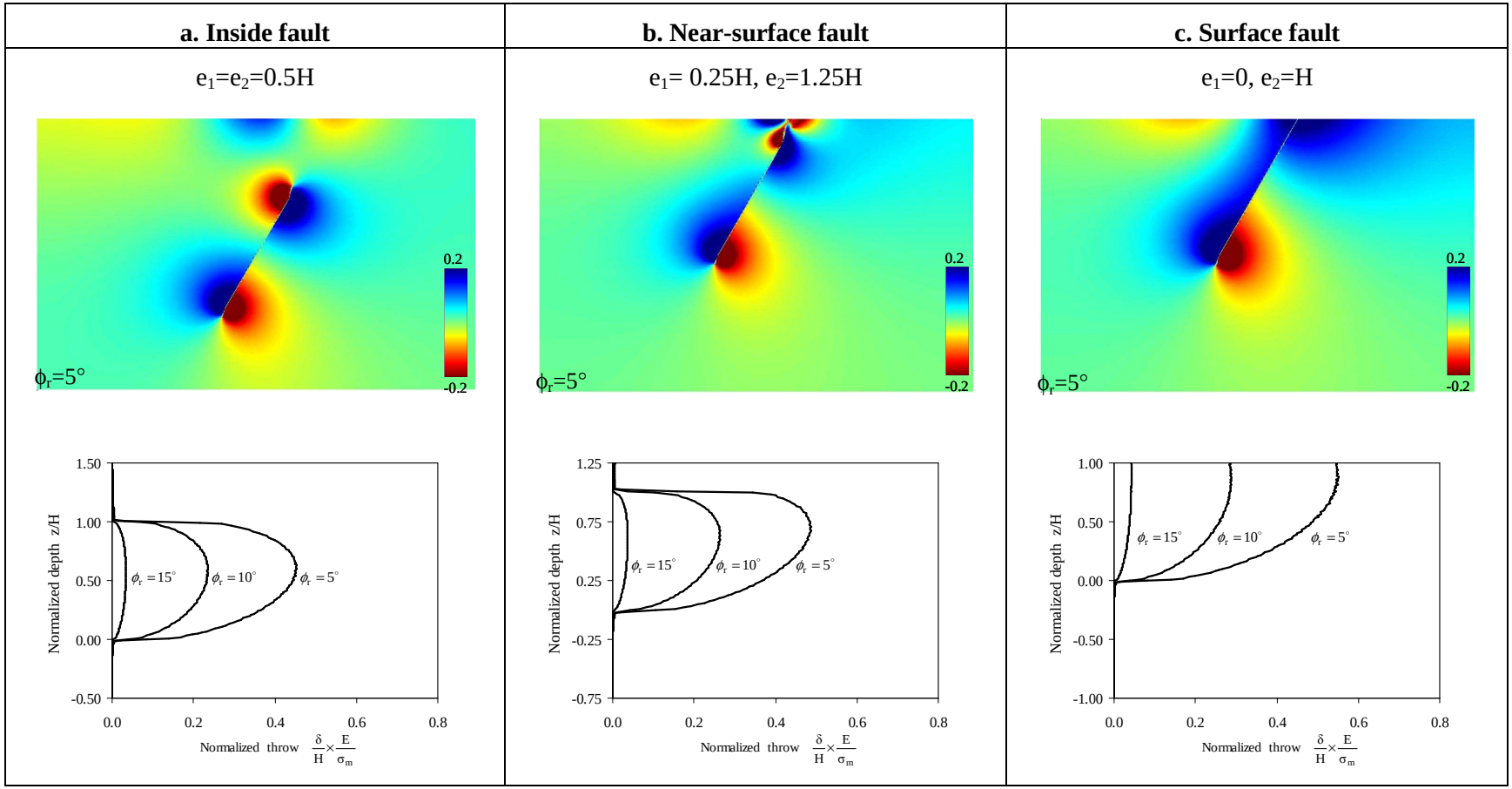

Figure 6.6 Proximity to a free upper boundary - Effect on displacement along the fault and volumetric strain: (a) Blind fault. (b) Near-surface fault. (c) Surface fault. Other boundary conditions in Table 6.1. The sediment stiffness increases with depth in the three cases E/σ_m=constant, in agreement with shallow fault conditions. Model parameters: sediment peak friction angle ϕ=30°, initial state of stress K_0=1-sinϕ=0.5, fracture orientation β=45°+ϕ/2=60°. Distance to boundaries noted in each column - refer to sketch in Table 6.1.

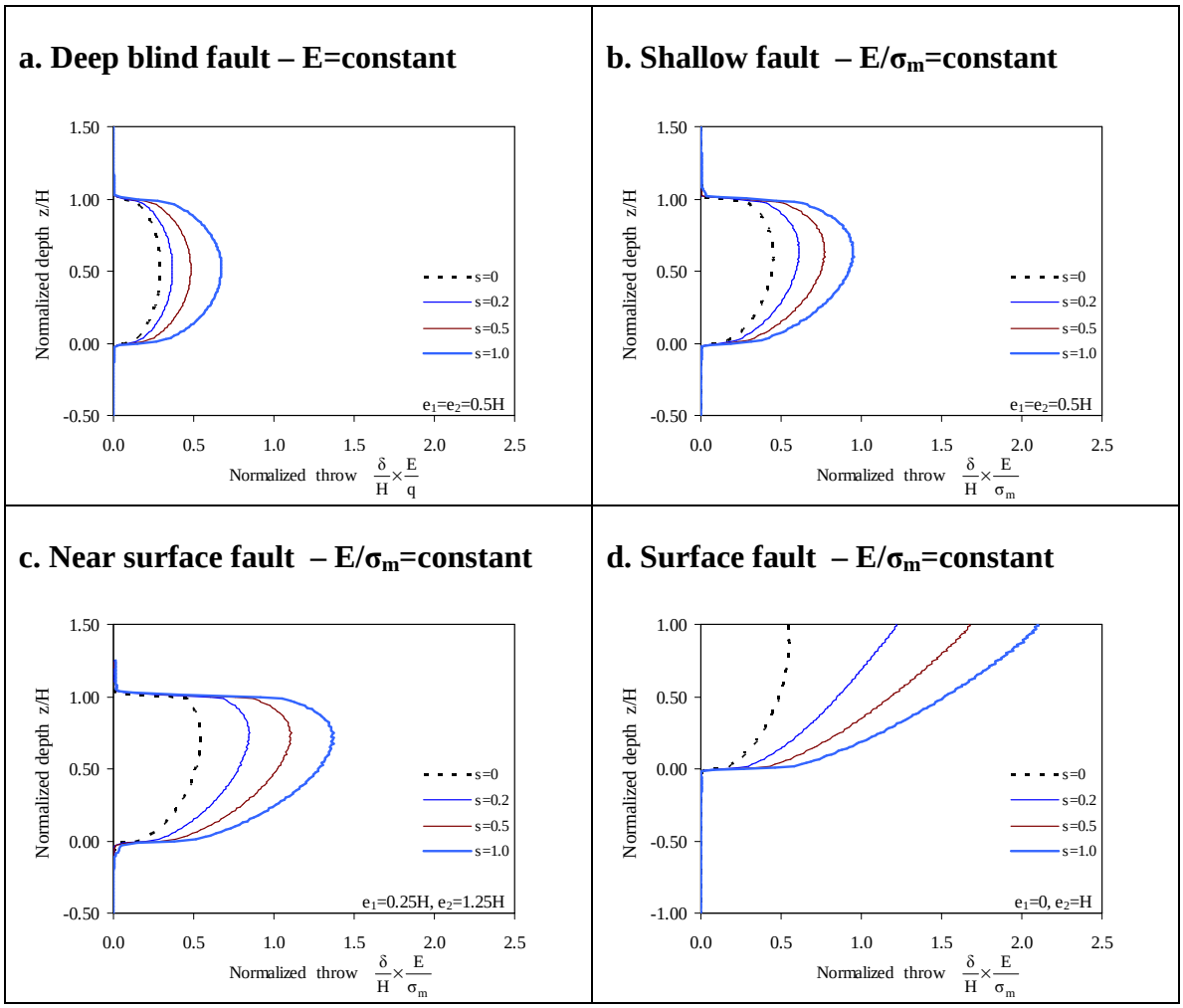

Figure 6.7 Effect of additional surface load on the development of displacements along the fault. The additional vertical stress is normalized by the initial vertical stress at the bottom of the model $s=\Delta\sigma'_z/\sigma'_{zo}$. Model parameters: sediment peak friction angle $\phi=30°$, residual friction angle $\phi_r=5°$, initial state of stress $K_0=1-\sin\phi=0.5$, fracture orientation $\beta=45°+\phi/2=60°$. Distance to boundaries noted in each plot - refer to Table 6.1 for model details.

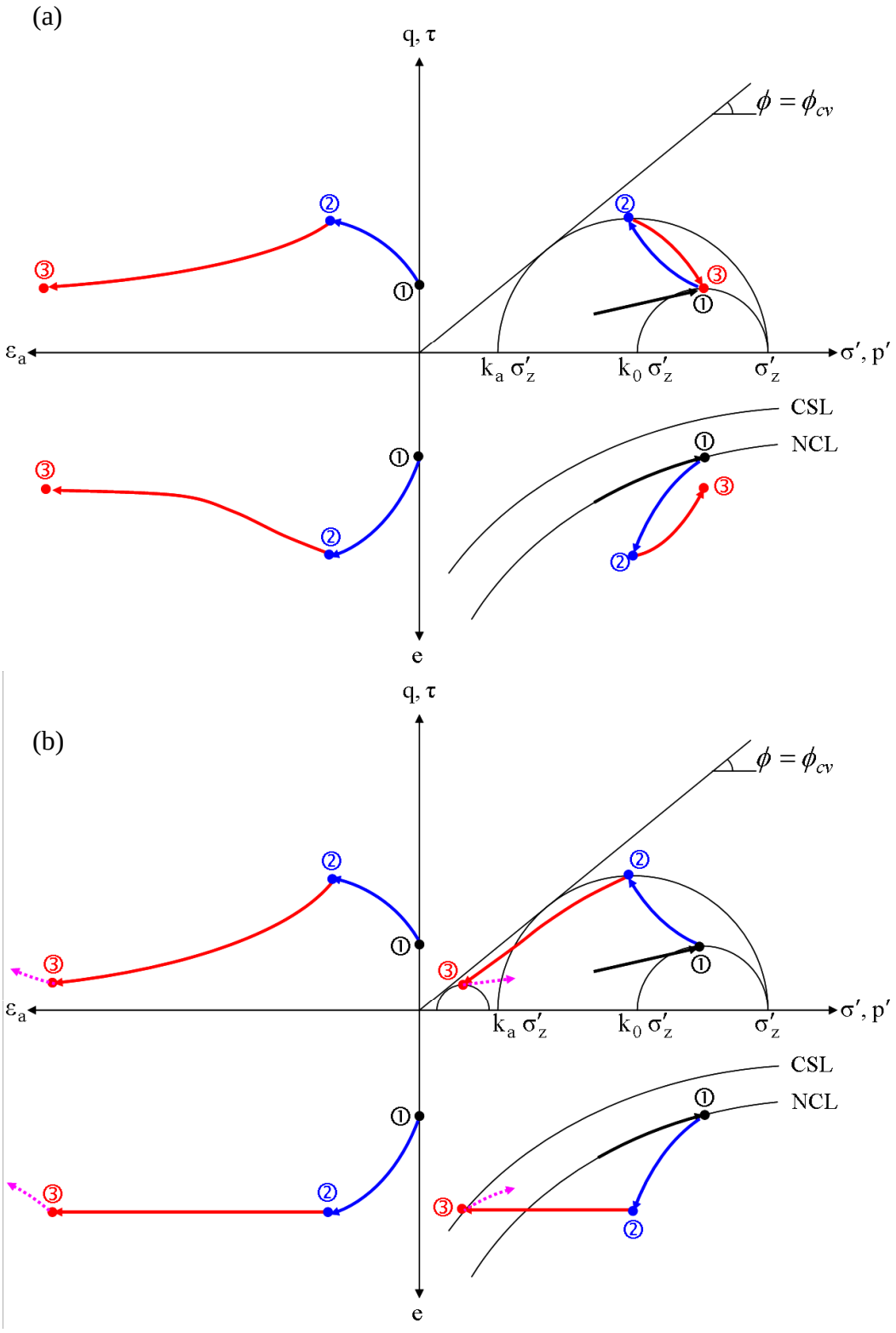

Figure 6.8 Evolution of stress and strain during mineral dissolution and fault formation. (a) Drained failure. (b) Undrained failure.

CHAPTER 7

CONCLUSIONS

This research has attempted to provide a fundamental understanding of the development of discontinuities in granular materials. The scope of the work has included: the evolution of K_0 during grain dissolution, shear failure as a consequence of grain dissolution, displacement fields in polygonal fault systems, desiccation cracks in saturated fine-grained soils, and fluid-driven fractures. Complementary analytical, numerical, and experimental techniques have been implemented to understand the initiation and propagation of localization planes by combining particle-level and macro-scale perspectives based on an effective stress formulation. The main conclusions are presented separately for each study.

Mineral dissolution and the evolution of K_0: Mineral dissolution is an ubiquitous process in soil formation.

- Grain dissolution produces a pronounced horizontal stress drop under zero lateral strain conditions.
- The minimum horizontal stress coefficient K_{min} can be as low as Rankine's active earth pressure coefficient K_a.
- While the lateral stress coefficient may be similar before and after dissolution, the internal fabric is quite distinct due to the rearrangement of the internal granular structure.

Contraction-driven shear failure in compacting uncemented sediments. Particle-scale volume contraction can cause shear failure in uncemented particulate materials under zero lateral strain conditions.

- Shear strain localization is analytically predicted and numerically modeled due to volume loss at the grain scale with no external loading and regional tectonics.
- Dissolution and shear failure provide a robust hypothesis for the genesis of polygonal fault systems: mineral dissolution leads to Coulomb active failure conditions, and post-peak strength softening behavior enhances shear strain localization.

Desiccation Cracks in Saturated Fine-Grained Soils. The mechanism for desiccation crack initiation and growth is centered on the invasion of the air-water interface membrane.

- The air-water interface membrane invades the largest pores and causes particle displacement away from the invasion point. The void ratio increases at the tip and facilitates further membrane invasion and crack growth.
- Desiccation cracks take place while the state of effective stress remains in compression everywhere in the soil mass, including at the crack tip.
- This hypothesis explains known observations related to desiccation cracks including pore fluid and fabric effects on desiccation crack patterns, slower crack propagation as the crack approaches a free boundary or a pre-existing crack, right-angle junction in crack pattern formation, and frictional resistance in axial extension with a normal failure surface.

Fluid driven discontinuities in granular materials. The miscibility of the invading and host fluids leads to distinct failure mechanisms: while the invasion of the interfacial membrane is the central phenomenon when immiscible fluids are involved, the seepage drag-force is responsible for fracture opening when the invading fluid is miscible with the host fluid.

- The pressure difference between invading and host fluids, causes the capillary force that drives grain displacement and further invasion of the interfacial membrane into the tip of the surface defect with the highest local void ratio. Once fractures invade the soil mass, wedge action continuously increases the local void ratio at the tip of fractures and leading to sustained propagating.
- In the case of boreholes pressurized with immiscible fluids, the ratio of fracture pressure in the borehole to the far-field effective confining stress decreases with increasing depth or confining stress. Compressibility and effective friction have a major effect on the fracture initiation pressure. Confining stress anisotropy alters the direction of fracture propagation from normal to the borehole wall in the near field ($r/R<1$), to perpendicular to the minor principal stress in the far field ($r/R>2$).

Displacement field in contraction driven faults. Displacements measured in polygonal fault systems can only be explained if the medium has experienced mineral dissolution.

- The parameters that determine the displacement field for a single normal fault embedded in dissolving sediments are: fault height, overburden effective stress, stiffness, and residual friction angle (or post peak strength).
- While the displacement field in situ and numerical predictions are similar, the measured magnitude requires remarkably low sediment stiffness as well as low post-peak shear strength. Both point to post dissolution-reprecipitation sediments with high porosity and probably high clay fraction.

REFERENCES

Abdelhamid, M. S., and R. J. Krizek (1976), At rest lateral earth pressure of a consolidating clay, Journal of the Geotechnical Engineering Division, ASCE, 102, 721-738.

Alfaro, M. C., and R. C. K. Wong (2001), Laboratory studies on fracturing of low-permeability soils, Canadian Geotechnical Journal, 38, 303-315.

Allen, J. R. L. (1982), Sedimentary structures, their character and physical basis, Elsevier Scientific Pub. Co., Amsterdam, New York

Alshibli, K. A., and S. Sture (2000), Shear band formation in plane strain experiments of sand, Journal of Geotechnical and Geoenvironmental Engineering, 126, 495-503.

Andersen, K. H., et al. (1994), Estimation of hydraulic fracture pressure in clay, Canadian Geotechnical Journal, 31, 817-828.

Andrawes, K. Z., and M. A. El-Sohby (1973), Factors affecting coefficient of earth pressure K_0, Journal of the Soil Mechanics and Foundations Division, ASCE, 99, 527-539.

Atkinson, J. H., et al. (1994), Undrained hydraulic fracture in cavity expansion tests, paper presented at Proceedings of the 13th International Conference on Soil Mechanics and Foundation Engineering, A.A. Balkema, New Delhi, India, 1009-1012.

Bai, T., et al. (2000), Explanation for fracture spacing in layered materials, Nature, 403, 753-756.

Barnett, J. A. M., et al. (1987), Displacement geometry in the volume containing a single normal fault, American Association of Petroleum Geologists Bulletin, 71, 925-937.

Baudon, C., and J. Cartwright (2008a), Early stage evolution of growth faults: 3D seismic insights from the Levant Basin, Eastern Mediterranean, Journal of Structural Geology, 30, 888-898.

Baudon, C., and J. A. Cartwright (2008b), 3D seismic characterisation of an array of blind normal faults in the Levant Basin, Eastern Mediterranean, Journal of Structural Geology, 30, 746-760.

Berndt, C., et al. (2003), Polygonal fault systems on the mid-Norwegian margin; a long-term source for fluid flow, Geological Society, London, Special Publications, 216, 283-290.

Berner, R. A. (1980), Early Diagenesis: A Theoretical Approach, Princeton University Press, New Haven, Connecticut.

Berre, T., et al. (1996), Measurement of small strains and K_0 values in triaxial tests on clay-shales, paper presented at Proceedings of the 8th International Congress on Rock Mechanics, Taylor and Francis, Tokyo, Japan, 3, 1195-1199.

Bishop, A. W., and A. K. G. Eldin (1953), The effect of stress history on the relation between f and porosity in sand, paper presented at Proc. of the Third International Conference on Soil Mechanics and Foundation Engineering, 1, 100-105.

Bjerrum, L., et al. (1972), Hydraulic fracturing in field permeability testing, Geotechnique, 22, 319-332.

Boeck, T., et al. (1999), Self-driven propagation of crack arrays: A stationary two-dimensional model, Physical Review E - Statistical Physics, Plasmas, Fluids, and Related Interdisciplinary Topics, 59, 1408-1416.

Bohloli, B., and C. J. de Pater (2006), Experimental study on hydraulic fracturing of soft rocks: Influence of fluid rheology and confining stress, Journal of Petroleum Science and Engineering, 53, 1-12.

Bolton, M. D., and A. M. Britto (1993), Finite element analysis of bridge abutments on firm clay, Computers and Geotechnics, 15, 221-245.

Bolton, M. D., et al. (1989), Finite element analysis of a centrifuge model of a retaining wall embedded in a heavily overconsolidated clay, Computers and Geotechnics, 7, 289-318.

Brinker, C. J., and G. W. Scherer (1990), Sol-gel science: the physics and chemistry of sol-gel processing, Academic Press, Boston, 908 pp.

Bronswijk, J. J. B. (1988), Modeling of water balance, cracking and subsidence of clay soils, Journal of Hydrology, 97, 199-212.

Brooker, E. W., and H. O. Ireland (1965), Earth pressures at rest related to stress history, Canadian Geotechnical Journal, 2, 1-15.

Bulut, R., et al. (2001), Soil suction measurements by filter paper, Expansive Clay Soils and Vegetative Influence on Shallow Foundations (GSP 115), ASCE, Houston, Texas, 243-261.

Burgmann, R., et al. (1994), Slip distributions on faults - Effects of stress gradients, inelastic deformation, heterogeneous host-rock stiffness, and fault interaction, Journal of Structural Geology, 16, 1675-1690.

Burland, J. B. (1990), On the compressibility and shear-strength of natural clays, Geotechnique, 40, 329-378.

Cailly, B., et al. (2005), Geological storage of CO_2: A state-of-the-art of injection processes and technologies, Oil and Gas Science and Technology, 60, 517-525.

Cartwright, J., et al. (2003), The genesis of polygonal fault systems; a review, Geological Society, London, Special Publications, 216, 223-243.

Cartwright, J. A. (1994), Episodic basin-wide fluid expulsion from geopressured shale sequences in the North-Sea Basin, Geology, 22, 447-450.

Cartwright, J. A., and D. N. Dewhurst (1998), Layer-bound compaction faults in fine-grained sediments, Bulletin of the Geological Society of America, 110, 1242-1257.

Cartwright, J. A., et al. (2007), Topseal bypass systems, AAPG Bulletin, 91, 1141-1166.

Cartwright, J. A., and L. Lonergan (1996), Volumetric contraction during the compaction of mudrocks: A mechanism for the development of regional-scale polygonal fault systems, Basin Research, 8, 183-193.

Castellanza, R., and R. Nova (2004), Oedometric tests on artificially weathered carbonatic soft rocks, Journal of Geotechnical and Geoenvironmental Engineering, 130, 728-739.

Chang, H. (2004), Hydraulic fracturing in particulate materials, Georgia Institute of Technology, Atlanta.

Chertkov, V. Y., et al. (2004), An approach for estimating the shrinkage geometry factor at a moisture content, Soil Science Society of America Journal, 68, 1807-1817.

Childs, C., et al. (2003), The growth and propagation of synsedimentary faults, Journal of Structural Geology, 25, 633-648.

Childs, E. C. (1969), An introduction to the physical basis of soil water phenomena, Wiley, London, New York, 493 pp.

Cho, G. C., and J. C. Santamarina (2001), Unsaturated particulate materials-particle-level studies, Journal of Geotechnical and Geoenvironmental Engineering, 127, 84-96.

Cowie, P. A., and C. H. Scholz (1992), Physical explanation for the displacement length relationship of faults using a post-yield fracture-mechanics model, Journal of Structural Geology, 14, 1133-1148.

Cundall, P. A., and O. D. L. Strack (1979), A discrete numerical model for granular assemblies, Geotechnique, 29, 47-65.

Dally, J. W., et al. (1985), On the uniqueness of the stress intensity factor-crack velocity relationship, International Journal of Fracture, 27, 159-168.

Davies, R. J., and J. A. Cartwright (2007), Kilometer-scale chemical reaction boundary patterns and deformation in sedimentary rocks, Earth and Planetary Science Letters, 262, 125-137.

de Pater, C. J., and Y. Dong (2007), Experimental study of hydraulic fracturing in sand as a function of stress and fluid rheology, Hydraulic Fracturing Technology Conference 2007, Society of Petroleum Engineers, College Station, TX, United states, SPE 105620.

Desrues, J., and G. Viggiani (2004), Strain localization in sand: an overview of the experimental results obtained in Grenoble using stereophotogrammetry, International Journal for Numerical and Analytical Methods in Geomechanics, 28, 279-321.

Eichhubl, P., et al. (2001), Opening-mode fracture in siliceous mudstone at high homologous temperature - Effect of surface forces, Geophysical Research Letters, 28, 1299-1302.

El-Kadi, A. I., and S. A. Williams (2000), Generating two-dimensional fields of autocorrelated, normally distributed parameters by the matrix decomposition technique, Ground Water, 38, 530-532.

Engelder, T. (1993), Stress regimes in the lithosphere, Princeton University Press, Princeton, N.J., 457 pp.

Eshelby, J. D. (1957), The determination of the elastic field of an ellipsoidal inclusion, and related problems, Proceedings of the Royal Society of London Series a-Mathematical and Physical Sciences, 241, 376-396.

Feda, J. (1984), K_0 coefficient of sand in triaxial apparatus, Journal of Geotechnical Engineering, ASCE, 110, 519-524.

Fredlund, D. G., and H. Rahardjo (1995), Soil mechanics for unsaturated soils, Wiley, New York, 517 pp.

Garagash, D. I. (2006), Propagation of a plane-strain hydraulic fracture with a fluid lag: Early-time solution, International Journal of Solids and Structures, 43, 5811-5835.

Garcia-Bengochea, I., et al. (1979), Pore distribution and permeability of silty clays, Journal of the Geotechnical Engineering Division, 105, 839-856.

Gay, A., et al. (2004), Polygonal faults-furrows system related to early stages of compaction; upper Miocene to recent sediments of the Lower Congo Basin, Basin Research, 16, 101-116.

Gleason, K. J., et al. (1986), Geometrical aspects of sorted patterned-ground in recurrently frozen soil, Science, 232, 216-220.

Goulty, N. R. (2001), Polygonal fault networks in fine-grained sediments; an alternative to the syneresis mechanism, First Break, 19, 69-73.

Goulty, N. R. (2002), Mechanics of layer-bound polygonal faulting in fine-grained sediments, Journal of the Geological Society of London, 159, 239-246.

Goulty, N. R. (2008), Geomechanics of polygonal fault systems: a review, Petroleum Geoscience, 14, 389-397.

Goulty, N. R., and R. E. Swarbrick (2005), Development of polygonal fault systems: a test of hypotheses, Journal of the Geological Society, 162, 587-590.

Hallett, P. D., and T. A. Newson (2005), Describing soil crack formation using elastic-plastic fracture mechanics, European Journal of Soil Science, 56, 31-38.

Harris, R. C. (2004), Giant desiccation cracks in Arizona, Arizona Geological Survey, 93 pp.

He, W., et al. (2003), Creep compaction of quartz aggregates: effects of pore-fluid flow-a combined experimental and theoretical study, American Journal of Science, 303, 73-93.

Henriet, J. P., et al. (1991), Early fracturing of Palaeogene clays, southernmost North Sea; relevance to mechanisms of primary hydrocarbon migration, Special Publication of the European Association of Petroleum Geoscientists, 1, 217-227.

Herrera, M. C., et al. (2007), Colombian volcanic ash soils, Characterization and Engineering Properties of Natural Soils, Taylor & Francis, Singapore, 2385-2409.

Higgs, W. G., and K. R. McClay (1993), Analogue sandbox modelling of Miocene extensional faulting in the Outer Moray Firth, Geological Society Special Publications, 71, 141-162.

Holmes, D. M., et al. (2006), Cracking during lateral drying of alumina suspensions, Journal of the American Ceramic Society, 89, 1908-1913.

Holtz, R. D., and M. B. Jamiolkowski (1985), Discussion of "Time dependence of lateral earth pressure", Journal of Geotechnical Engineering, ASCE, 111, 1239-1242.

Houlsby, G. T., and C. P. Wroth (1980), Strain and displacement discontinuities in soil, Journal of the Engineering Mechanics Division, ASCE, 106, 753-771.

Jaeger, J. C., and N. G. W. Cook (1976), Fundamentals of rock mechanics, 2nd ed., Chapman and Hall, Wiley, 585 pp.

Jain, A. K., and R. Juanes (2008), Pore-scale mechanistic study of the preferential mode of hydrate formation in sediments: Coupling of multiphase fluid flow and sediment mechanics, paper presented at Proceedings of the 6th International

Conference on Gas Hydrates (ICGH 2008), Vancouver, British Columbia, CANADA.

Jain, A. K., and R. Juanes (2009), Preferential mode of gas invasion in sediments: Grain-scale mechanistic model of coupled multiphase fluid flow and sediment mechanics, Journal of Geophysical Research, in press.

Jaky, J. (1944), The coefficient of earth pressure at rest, Journal for Society of Hungarian Architects and Engineers, 78(22), 355-358 (in Hungarian).

Jamiolkowski, M. L., C.C.; Germaine, J. T.; Lancellotta, R. (1985), New developments in field and laboratory testing of soils, paper presented at Proc. 11th International Conference On Soil Mechanics and Foundation Engineering, San Francisco, 1, 57-154.

Jaworski, G. W., et al. (1981), Laboratory study of hydraulic fracturing, Journal of the Geotechnical Engineering Division, ASCE, 107, 713-732.

Juang, C. H., and R. D. Holtz (1986), Fabric pore size distribution, and permeability of sandy soils, Journal of Geotechnical Engineering, ASCE, 112, 855-868.

Kavazanjian, E., Jr., and J. K. Mitchell (1984), Time dependence of lateral earth pressure, Journal of Geotechnical Engineering, ASCE, 110, 530-533.

Kenney, T. C. (1959), Discussion of "Geotechnical properties of glacial lake clays," by T. H. Wu, Journal of the Soil Mechanics and Foundations Division, ASCE, 85, 67-79.

Khodaverdian, M., and P. McElfresh (2000), Hydraulic fracturing stimulation in poorly consolidated sand: Mechanisms and consequences, Society of Petroleum Engineers (SPE), Dallas, TX, United states, 715-727.

Kim, H. K., and J. C. Santamarina (2008), Spatial variability: Drained and undrained deviatoric load response, Geotechnique, 58, 805-814.

Koliji, A., et al. (2006), Suction induced effects on the fabric of a structured soil, Transport in Porous Media, 64, 261-278.

Kolymbas, D., and E. Bauer (1993), Soft oedometer. A new testing device and its application for the calibration of hypoplastic constitutive laws, Geotechnical Testing Journal, 16, 263-270.

Komak Panah, A., and E. Yanagisawa (1989), Laboratory studies on hydraulic fracturing criteria in soil, Soils and Foundations, 29, 14-22.

Konrad, J. M., and R. Ayad (1997), An idealized framework for the analysis of cohesive soils undergoing desiccation, Canadian Geotechnical Journal, 34, 477-488.

Kulhawy, F. H., and P. W. Mayne (1990), Manual on estimating soil properties for foundation design, Electric Power Research Institute, Palo Alto, CA, 306 pp.

Lachenbruch, A. H. (1962), Mechanics of thermal contraction cracks and ice-wedge polygons in permafrost, Geological Society of America, New York, NY, United States, 69 pp.

Lade, P. V. (2002), Instability, shear banding, and failure in granular materials, International Journal of Solids and Structures, 39, 3337-3357.

Le Guen, Y., et al. (2007), Enhanced deformation of limestone and sandstone in the presence of high P_{CO2} fluids, Journal of Geophysical Research, 112, 1-21.

Lonergan, L., et al. (1998), The geometry of polygonal fault systems in Tertiary mudrocks of the North Sea, Journal of Structural Geology, 20, 529-548.

Lu, N., et al. (2007), Tensile strength characteristics of unsaturated sands, Journal of Geotechnical and Geoenvironmental Engineering, 133, 144-154.

Lupini, J. F., et al. (1981), The drained residual strength of cohesive soils, Geotechnique, 31, 181-213.

Lura, P., et al. (2007), Influence of shrinkage-reducing admixtures on development of plastic shrinkage cracks, ACI Materials Journal, 104, 187-194.

Malthe-Sorenssen, A., et al. (2006), Fracture patterns generated by diffusion controlled volume changing reactions, Physical Review Letters, 96, 245501-245501.

Massarsch, K. R. (1978), New aspects of soil fracturing in clay, Journal of the Geotechnical Engineering Division, ASCE, 104, 1109-1123.

Mayne, P. W., and F. H. Kulhawy (1982), K_0-OCR relationships in soil, Journal of the Geotechnical Engineering Division, ASCE, 108, 851-872.

Mesri, G., and A. F. Cepedadiaz (1986), Residual shear-strength of clays and shales, Geotechnique, 36, 269-274.

Mesri, G., and T. M. Hayat (1993), Coefficient of earth pressure at rest, Canadian Geotechnical Journal, 30, 647-666.

Michalowski, R. L. (2005), Coefficient of earth pressure at rest, Journal of Geotechnical and Geoenvironmental Engineering, ASCE, 131, 1429-1433.

Mori, A., and M. Tamura (1987), Hydrofracturing pressure of cohesive soils, Soils and Foundations, 27, 12–24.

Morris, P. H., et al. (1992), Cracking in drying soils, Canadian Geotechnical Journal, 29, 263-277.

Muir Wood, D. (1990), Soil behaviour and critical state soil mechanics, Cambridge University Press, Cambridge, England.

Muraoka, H., and H. Kamata (1983), Displacement distribution along minor fault traces, Journal of Structural Geology, 5, 483-495.

Naser Abu-Hejleh, A., and D. Znidarcic (1995), Desiccation theory for soft cohesive soils, Journal of Geotechnical Engineering, ASCE, 121, 493-502.

Nelson, M. (2007), 3D geometry and kinematics of non-colinear fault intersections, Cardiff University.

Nicol, A., et al. (2003), The geometry, growth and linkage of faults within a polygonal fault system from South Australia, Geological Society Special Publications, London, 216, 245-261.

Okochi, Y., and F. Tatsuoka (1984), Some factors affecting K_0 values of sand measured in triaxial cell, Soils and Foundations, 24, 52-68.

Olson, R. E. (1974), Shearing strength of kaolinite, illite, and montmorillonite, Journal of the Geotechnical Engineering Division, ASCE, 100, 1215-1229.

Ovarlez, G., and E. Clement (2003), Slow dynamics and aging of a confined granular flow, Physical Review E (Statistical, Nonlinear, and Soft Matter Physics), 68, 31302-31301.

Palomino, A. M., and J. C. Santamarina (2005), Fabric map for kaolinite: Effects of pH and ionic concentration on behavior, Clays and Clay Minerals, 53, 211-223.

Peng, X., and R. Horn (2007), Anisotropic shrinkage and swelling of some organic and inorganic soils, European Journal of Soil Science, 58, 98-107.

Perrin, G., and J. B. Leblond (1993), Rudnicki and Rice analysis of strain localization revisited, Journal of Applied Mechanics-Transactions of the ASME, 60, 842-846.

Poliakov, A. N. B., et al. (1994), Fractal plastic shear bands, Fractals, 2, 567-581.

Pollard, D. D., and P. Segall (1987), Theoretical displacements and stresses near fractures in rock: with applications to faults, joints, veins, dikes, and solution surfaces, in Fracture Mechanics of Rocks, edited by B. K. Atkinson, Academic Press, London, 277-349.

Prodanovic, M., and S. L. Bryant (2006), A level set method for determining critical curvatures for drainage and imbibition, Journal of Colloid and Interface Science, 304, 442-458.

Prŭska, M. J. (1973), Effect of initial stress on the stress-strain relation, paper presented at Proceedings of the 8th International Conference on Soil Mechanics and Foundation Engineering, Moscow, 4, 26-28.

Ramsey, J. G., and R. J. Lisle (2000), The Techniques of Modern Structural Geology Vol. 3: Applications of Continuum Mechanics in Structural Geology, Academic Press, London.

Renard, F., et al. (2001), Enchanced pressure solution creep rates induced by clay particles: Experimental evidence in salt aggregates, Geophysical Research Letters, 28, 1295-1298.

Renard, F., et al. (2005), Numerical modeling of the effect of carbon dioxide sequestration on the rate of pressure solution creep in limestone: Preliminary results, Oil and Gas Science and Technology, 60, 381-399.

Rodriquez, R., et al. (2007), Experimental and numerical analysis of desiccation of a mining waste, Canadian Geotechnical Journal, 44, 644-658.

Roscoe, K. H., and J. B. Burland (1968), On the generalized stress-strain behaviour of 'wet' clay, in Engineering Plasticity, edited by J. Heyman and F. A. Leckie, Cambridge University Press, Cambridge, 535-609.

Rothenburg, L., and R. J. Bathurst (1989), Analytical study of induced anisotropy in idealized granular materials, Geotechnique, 39, 601-614.

Rudnicki, J. W., and J. R. Rice (1975), Conditions for the localization of deformation in pressure-sensitive dilatant materials, Journal of the Mechanics and Physics of Solids, 23, 371-394.

Sanford, R. J. (2003), Principles of fracture mechanics, Prentice Hall, Upper Saddle River, NJ.

Santamarina, J. C., and G. C. Cho (2001), Determination of critical state parameters in sandy soils - Simple procedure, Geotechnical Testing Journal, 24, 185-192.

Santamarina, J. C., et al. (2001), Soils and waves: particulate materials behavior, characterization and process monitoring, J. Wiley & Sons, Chichester, England, New York, 488 pp.

Scherer, G. W. (1990), Theory of drying, Journal of the American Ceramic Society, 73, 3-14.

Schmertmann, J. H. (1983), A simple question about consolidation, Journal of Geotechnical Engineering, ASCE, 109, 119-122.

Schofield, A. N. (1980), Cambridge geotechnical centrifuge operations, Geotechnique, 30, 227-268.

Schultz, R. A., et al. (2006), Displacement-length scaling relations for faults on the terrestrial planets, Journal of Structural Geology, 28, 2182-2193.

Shin, H., and J. C. Santamarina (2009), Mineral dissolution on K_0 effects, Journal of Geotechnical and Geoenvironmental Engineering, ASCE, in press.

Shin, H., et al. (2008), Contraction-driven shear failure in compacting uncemented sediments, Geology, 36, 931-934.

Skempton , A. W. (1961), Horizontal stresses in an overconsolidated Eocene clay, Proc. 5th Intl. Conf. Soil Mech. Found. Eng., 1, 351-357.

Skempton, A. W. (1985), Residual strength of clays in landslides, folded strata and the laboratory, Geotechnique, 35, 3-18.

Slatter, E. E., et al. (2005), Measuring lateral pressures during suction controlled one dimensional consolidation, paper presented at Proceedings of an International Symposium on Advanced Experimental Unsaturated Soil Mechanics, Taylor & Francis, London, Trento, Italy, 117-124.

Soga, K., et al. (2006), Macro and micro behaviour of soil fracturing, International Symposium on Geomechanics and Geotechnics of Particulate Media - Geomechanics and Geotechnics of Particulate Media, Taylor and Francis, Balkema, Ube, Yamaguchi, Japan, 421-427.

Soliva, R., et al. (2006), Spacing and linkage of confined normal faults: Importance of mechanical thickness, Journal of Geophysical Research-Solid Earth, 111, B01402.

Stuevold, L. M., et al. (2003), Polygonal faults in the Ormen Lange Field, More Basin, offshore Mid Norway, Geological Society Special Publications, London, 216, 263-281.

Taber, S. (1930), The mechanics of frost heaving, Journal of Geology, 38, 303-317.

Tanaka, H., et al. (2003), Pore size distribution of clayey soils measured by mercury intrusion porosimetry and its relation to hydraulic conductivity, Soils and Foundations, 43, 63-73.

Terzaghi, K., and R. B. Peck (1967), Soil mechanics in engineering practice, 2nd ed., Wiley, New York, 729 pp.

Terzaghi, K., et al. (1996), Soil mechanics in engineering practices, 3rd ed., Wiley, New York.

Thusyanthan, N. I., et al. (2007), Crack initiation in clay observed in beam bending, Geotechnique, 57, 581-594.

Ting, C. M. R., et al. (1994), Development of K_0 in soft soils, Geotechnique, 44, 101-109.

Toshikazu, H., et al. (2002), Features of crack propagation by hydraulic fracturing in cohesive soil. Experimental study on seepage failure of small earth dams, Transactions of the Japanese Society of Irrigation, Drainage and Reclamation Engineering, 219, 383-392.

Towner, G. D. (1988), The influence of sand- and silt-size particles on the cracking during drying of small clay-dominated aggregates, Journal of Soil Science, 39, 347-356.

Truong, Q. H., et al. (2009), Stiffness characteristics of vanishing mixtures, Korea University, Manuscript under review.

URAPIV (2008), http://urapiv.wordpress.com/.

Uri, L., et al. (2006), Oscillatory ductile compaction dynamics in a cylinder, Physical Review E (Statistical, Nonlinear, and Soft Matter Physics), 74, 31301-31301.

van Damme, H., and M. Ben Ohoud (1990), From flow to fracture and fragmentation in colloidal media, 2, Local order and fragmentation geometry, Plenum, New York, 105-116

Vermeer, P. A. (1990), The orientation of shear bands in biaxial tests, Geotechnique, 40, 223-236.

Walsh, J. J., and J. Watterson (1988), Analysis of the relationship between displacements and dimensions of faults, Journal of Structural Geology, 10, 239-247.

Wang, Y. H., and D. Xu (2007), Dual porosity and secondary consolidation, Journal of Geotechnical and Geoenvironmental Engineering, 133, 793-801.

Watterson, J., et al. (2000), Geometry and origin of a polygonal fault system, Journal of the Geological Society, 157, 151-162.

Weaver, C. E. (1989), Clays, muds, and shales, Elsevier, Amsterdam, New York, 819 pp.

Weinberger, R. (1999), Initiation and growth of cracks during desiccation of stratified muddy sediments, Journal of Structural Geology, 21, 379-386.

Willemse, E. J. M., et al. (1996), Three-dimensional analyses of slip distributions on normal fault arrays with consequences for fault scaling, Journal of Structural Geology, 18, 295-309.

Wilson, G. W., et al. (1997), Effect of soil suction on evaporative fluxes from soil surfaces, Canadian Geotechnical Journal, 34, 145-155.

Wolf, H., et al. (2003), Experimental investigation of shear band patterns in granular material, Journal of Structural Geology, 25, 1229-1240.

Wolf, H., et al. (2005), Centrifuge model tests on sand specimen under extensional load, International Journal for Numerical and Analytical Methods in Geomechanics, 29, 25-47.

Wright, C. A., and L. Weijers (2001), Hydraulic fracture reorientation: Does it occur? Does it matter?, Leading Edge, 20, 1185-1189.

Wu, R. (2006), Some fundamental mechanisms of hydraulic fracturing, Georgia Institute of Technology, Atlanta.

Yakobson, B. I. (1991), Morphology and rate of fracture in chemical decomposition of solids, Physical Review Letters, 67, 1590-1593.

Yanagisawa, E., and A. K. Panah (1994), Two dimensional study of hydraulic fracturing criteria in cohesive soils, Soils and Foundations, 34, 1-9.

Zabat, M., et al. (1997), Surface topography and mechanical properties of smectite films, Progress in Colloid and Polymer Science, Springer, Berlin, Heidelberg, 96-102.

Zarzycki, J., et al. (1982), Synthesis of glasses from gels: The problem of monolithic gels, Journal of Materials Science, 17, 3371-3379.

Zhang, G., et al. (2007), Characterization and engineering properties of the Old Alluvium in Puerto Rico, paper presented at Characterization and Engineering Properties of Natural Soils, Taylor & Francis, Singapore, 2557-2588.

Zhu, F., et al. (1995), Factors affecting at-rest lateral stress in artificially cemented sands, Canadian Geotechnical Journal, 32, 195-203.

VITA

Hosung Shin

Hosung Shin was born on June 24, 1972 in Goheung, Korea. He received his Bachelor degree in Civil and Environmental engineering from Korea University (Seoul, Korea) in February 1995, and his Master degree in Civil Engineering from Korea Advanced Institute of Science and Technology (KAIST - Daejon, Korea) in February 1997. During seven years, he worked at Saman Engineering and LG Engineering and Construction. In August 2004, he started research towards this doctoral dissertation at the Georgia Institute of Technology, and will receive his Ph.D. degree in Civil Engineering (Geosystems Group) in August 2009.